NBSIR 74-380

PLANAR NEAR-FIELD MEASUREMENTS ON HIGH PERFORMANCE ARRAY ANTENNAS

Allen C. Newell
Myron L. Crawford

Electromagnetics Division
Institute for Basic Standards
National Bureau of Standards
Boulder, Colorado 80302

July 1974

Prepared for
Air Force Avionics Laboratory
Wright Patterson Air Force Base, Ohio 45433

NBSIR 74-380

PLANAR NEAR-FIELD MEASUREMENTS ON HIGH PERFORMANCE ARRAY ANTENNAS

Allen C. Newell
Myron L. Crawford

Electromagnetics Division
Institute for Basic Standards
National Bureau of Standards
Boulder, Colorado 80302

July 1974

Prepared for
Air Force Avionics Laboratory
Wright Patterson Air Force Base, Ohio 45433

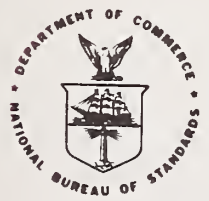

U.S. DEPARTMENT OF COMMERCE, Frederick B. Dent, Secretary

NATIONAL BUREAU OF STANDARDS, Richard W. Roberts, Director

CONTENTS

LIST OF FIGURES

LIST OF FIGURES (continued)

LIST OF FIGURES (continued)

LIST OF FIGURES (continued)

PLANAR NEAR-FIELD MEASUREMENTS ON HIGH PERFORMANCE ARRAY ANTENNAS

The results of measurements which apply the planar near-field measurement technique to phased array antennas are described. Fast and efficient tests are used to determine the required scan area and data point spacing. The use of these tests can reduce the amount of data required for some antennas without significantly increasing the errors in computed results.

Measurements were made at different distances from the antennas, with the probe transmitting and receiving, and for both sum and monopulse difference patterns. Comparisons between the far-field patterns computed from the near-field data and those measured on far-field ranges are presented.

Key words: Antennas; near-field measurements; phased arrays.

1.0 Introduction

This program is concerned with determining the far-field characteristics of phased array antennas from measured near-field data. The required theory and basic measurement techniques have been developed in the past at the NBS Electromagnetics Division [1-4] and at other laboratories [5] and indicate the usefulness of this approach. The purpose of this particular program is to demonstrate that this measurement approach can provide accurate results when applied to radar type arrays which are mounted on an aircraft and contained within a radome.

The details of this program are described in the Statement of Work, and may be divided into three parts:

I -- Concept Application Study, which describes the plane-wave scattering matrix theory as it applies to the present program. This is done in such a way that the antenna engineers, who are potential users of this material, will appreciate the value of the approach and be able to use the theoretical formulations and measurement procedures.

II -- A Measurement Program, which consisted of near-field measurements on two test antennas. The test antennas were chosen with characteristics representative of high performance radars. These included narrow beamwidths, side lobes below 30 dB, monopulse difference minima of at least 30 dB, beam steering to ± 45°, and operation frequencies in the x-band range. Neither test antenna had all these features, but all were realized in at least one of the antennas. Some of the goals of the measurement program are summarized below.

a. Data Minimization. Since a large amount of near-field data is generally required, large computer storage is needed for data processing. If the amount of measured data could be reduced without a significant sacrifice in the accuracy of computed results, a large savings could be realized in both measurement and computation time. Tests were therefore made to determine the optimum spacing of data points and the size of the scan area for a given test antenna and probe combination.

b. Measurements on Radome Enclosed Antennas. In the past, all of our measurements have been done within 10-50 wavelengths of the test antenna. If a long radome encloses the antenna, the measurement plane must be moved farther from the antenna. Tests were performed to determine what effect this would have on the scan parameters (spacing and area) and the accuracy of computed results.

c. Transmitting From Probe. In previous measurements, the test antenna was transmitting and the probe receiving. For test antennas which are non-reciprocal or which do not operate in the transmit modes, the probe would have to be used as the transmitter. The theory indicated that this should not present any difficulties, and measurements were performed to determine if there were any unforeseen experimental problems.

d. Locating Faults in the Array and/or Radome. Tests were performed to see how effective the near-field technique would be in detecting and locating failures in the array, and if possible, also in the radome.

e. Demonstration of Agreement with Far-Field Measurements. Since this measurement approach is new to most antenna engineers, and involves the use of fairly sophisticated theory and computations, it does not enjoy the confidence placed in conventional far-field measurements. Questions are frequently asked if the results from near-field measurements agree with "actual" (far-field) measurements. While such comparisons are helpful, and have been performed in the past, it must be realized that errors and approximations exist in both measurements. In some cases, the far-field measurements are less accurate than the near-field measurement, and they cannot serve as a suitable standard to judge the accuracy of this new method.

Comparing the results of both measurements will demonstrate that there are no gross errors in either approach, and will help to build confidence in the near-field approach. A more complete and valid approach to proving accuracy, however, is to study how the approximations to the theory, and measurement errors in the near-field data affect the accuracy of the computed far-field parameters. This approach is being pursued as a part of a thorough error analysis of the near-field techniques.

III -- The third part of the program involves a System Design Study to specify the hardware and software necessary to implement the planar near-field measurement technique.

2.0 Concept Application Study -- Review of the Plane Wave, Scattering-Matrix Theory of Antenna-Antenna Interactions

Frequent use is made in this report of the quantities used in a plane wave scattering matrix theory of antennas (more completely covered in references [1-4]). A brief discussion is given here to acquaint the reader with the basic quantities and their meaning and to give the results of the theory that are required in a treatment of near-field measurements. The intent of the following discussion is to describe the concepts used in this new approach to antenna theory in terms of quantities which should be familiar to the microwave and antenna engineer.

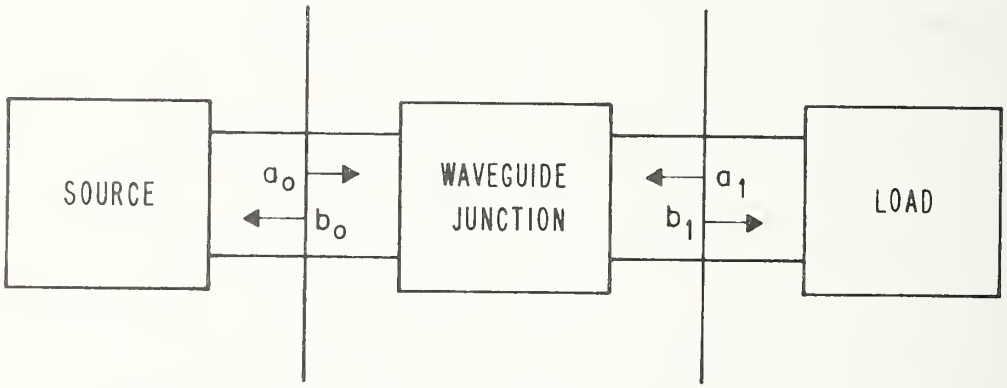

Figure 1. Waveguide Junction 2-Port Schematic.

The theoretical formulation and notation employed here are, in many respects, similar to those found in the familiar scattering matrix description of waveguide junctions. Therefore, we begin by referring to a waveguide two-port, shown schematically in figure 1 as it is described by the S (scattering) parameters. The incident and emergent wave amplitudes a_0, a_1, b_0, b_1, on two terminal surfaces, 0 and 1, at the ends of the two-port

are related by the equations [6]

$$b_0 = S_{00}a_0 + S_{01}a_1 \tag{1a}$$

$$b_1 = S_{10}a_0 + S_{11}a_1, \tag{1b}$$

where S_{00} and S_{11} are the reflection coefficients of the two-port and S_{01} and S_{10} are the transmission coefficients. These S parameters are complex scalar quantities which specify the response of the two-port transducer at a given frequency and for one waveguide mode. Once these quantities have been obtained from measurements, they can be used to determine how this device will interact with others in a composite system.

Although an antenna is more complicated than a simple waveguide two-port, it can still be described by the same sort of formal representation. The antenna is viewed as a multi-port transducer (one input port and an output port for each polarization and direction in space), which transforms wave amplitudes in a closed transmission line system to an angular spectrum of plane waves in the space system and vice versa. The plane-wave S parameters provide a powerful description of an antenna from this transducer point of view. As with the two-port, once these S parameters have been determined, they may be used to evaluate the antenna performance in a larger, more complicated system. Familiar quantities such as power gain and axial ratio are easily derived from the S parameters, but the S-parameters are not limited to use in the far-field plane wave situations which are usually assumed. One of their main advantages is that they give a means of formulating near-field antenna interaction problems in a way which gives new insight into the problems and which allows practical solutions.

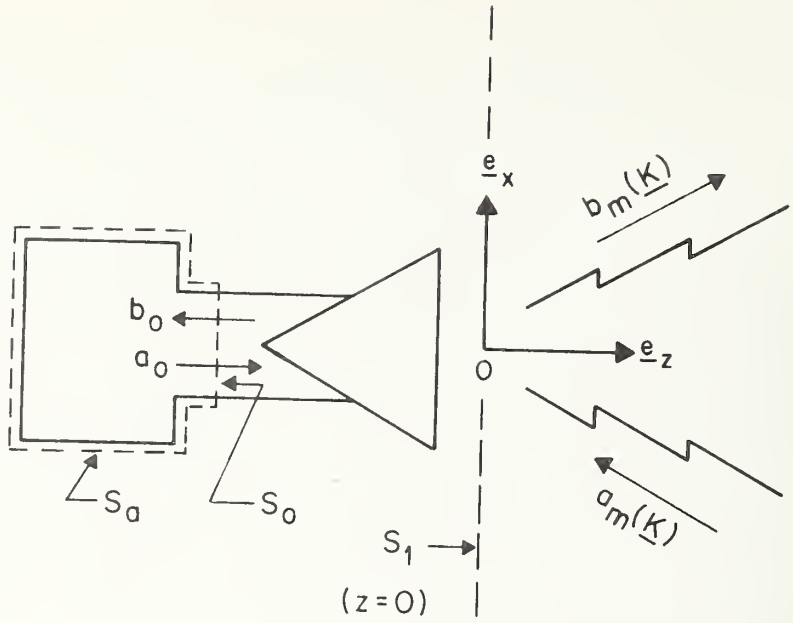

Figure 2. Antenna in Measurement Coordinate System.

To further define these parameters, consider the antenna shown in figure 2 oriented in the coordinate system Oxyz with unit vectors $\underline{e}_x$, $\underline{e}_y$, $\underline{e}_z$ in the space to the right of the antenna, and let $\underline{k}$ be the propagation vector for plane waves in this space. Since $\underline{k}\cdot\underline{k}$ is fixed by the relation, $\underline{k}\cdot\underline{k} = k^2 = \omega^2\mu\varepsilon$, we can consider k_z and $\underline{k}$ to be functions of $\underline{K}$, the transverse part of $\underline{k}$. That is, $\underline{K} = k_x\underline{e}_x + k_y\underline{e}_y$ and $k_z = \pm\gamma$, where

$$\gamma = \sqrt{k^2 - K^2}. \qquad (2)$$

$\underline{K}$ will be the independent variable in most of what follows, and defines directions in the space to the right of the antenna. For example $\underline{K} = 0$ defines the reference boresight direction; $\underline{K} = k_y\,\underline{e}_y + 0\,\underline{e}_x$ defines the E-plane for an antenna with linear polarization in the y-direction; and $\underline{K} = 0\,\underline{e}_y + k_x\,\underline{e}_x$ defines the H-plane for the same antenna.

Two additional transverse unit vectors which are used in the formulation are defined as

$$\underline{\kappa}_1 = \underline{K}/|K|, \quad \underline{\kappa}_2 = \underline{e}_z \times \underline{\kappa}_1. \tag{3}$$

These vectors are respectively in and perpendicular to the plane of $\underline{k}$ and $\underline{e}_z$ and are used to specify the independent polarizations of the electric field associated with any given $\underline{k}$. This choice of polarization is the one used in electromagnetic theory in deriving the Fresnel equations and also corresponds to TE and TM modes of waveguide theory.

In figure 2, a_0 and b_0 are incident and emergent wave amplitudes at the surface S_0 just as in the waveguide junction formulation. $a_m(\underline{K})$ and $b_m(\underline{K})$ are spectral density functions for incoming and outgoing plane waves and are analogous to a_1 and b_1 in figure 1 in that each represents the complex amplitude of a plane wave traveling in the $\underline{K}$ direction. This decomposition of the transverse electric field into a continuous angular spectrum of plane waves is analogous to the familiar practice of analyzing a complicated time function in terms of its frequency components. (Indeed there are many concepts from time and frequency domain analysis which can be carried over to the antenna problem and which give new insight to the processes involved.) These ideas are formalized by the following equations which define the S parameter functions that characterize the antenna

$$b_0 = S_{00} a_0 + \int \sum_m S_{01}(m,\underline{K})\ a_m(\underline{K})\ d\underline{K} \tag{4a}$$

$$b_m(\underline{K}) = S_{10}(m,\underline{K})\ a_0 + \int \sum_n S_{11}(m,\underline{K};n,\underline{L})\ a_n(\underline{L})\ d\underline{L}, \tag{4b}$$

where the summation is over the two values of the polarization index, m or n, and integration is over all values of $\underline{K}$, $d\underline{K} \equiv dk_x\, dk_y$.

The significance of each parameter can best be seen by considering two special cases. First assume that the antenna is transmitting into free space, and therefore there are no waves incident from the right, $a_m(\underline{K}) = 0$. We then have

$$b_0 = S_{00} a_0, \tag{5a}$$

$$b_m(\underline{K}) = S_{10}(m,\underline{K})\ a_0. \tag{5b}$$

S_{00} is thus a simple input reflection coefficient term, and $S_{10}(m,\underline{K})$ defines the transmitting characteristic since it describes how the input wave amplitude a_0 is transformed by the antenna into an angular pattern of plane waves $b_m(\underline{K})$.

Next assume that the antenna is being used as a receiver and is terminated in a reflectionless load. In this case $a_0 = 0$ and

$$b_0 = \int \sum_m S_{01}(m,\underline{K})\ a_m(\underline{K})\ d\underline{K}, \tag{6a}$$

$$b_m(\underline{K}) = \int \sum_m S_{11}(m,\underline{K};n,\underline{L})\ a_n(\underline{L})\ d\underline{L}. \tag{6b}$$

$S_{01}(m,\underline{K})$ is called the receiving characteristic since it describes how the antenna responds to an incident spectrum of plane waves $a_m(\underline{K})$. $S_{11}(m,\underline{K};n,\underline{L})$ is called the scattering characteristic as it describes how waves incident from the right are scattered back into the same space.

If the antenna is reciprocal, then $S_{10}(m,\underline{K})$ and $S_{01}(m,\underline{K})$ are related by the reciprocity relation [1]

$$-\eta_0\ S_{01}(m,\underline{K}) = \eta_m(\underline{K})\ S_{10}(m,-\underline{K}),\ (m = 1,2) \tag{7}$$

where $\eta_1 = \frac{k}{\gamma}\sqrt{\frac{\varepsilon}{\mu}}$ and $\eta_2 = \frac{\gamma}{k}\sqrt{\frac{\varepsilon}{\mu}}$, and are referred to as wave admittances, and η_0 is the wave admittance of the transmission line.

It should be noted that the formulation is expressed in terms of transverse components, where transverse as used here means transverse to z. We will most generally be working with x- and y-components or κ_1 and κ_2-components (which are in the x-y plane) rather than the spherical components which are employed in far-field measurements. The spherical components may of course be obtained by the appropriate coordinate transformation, but they will not generally appear in the formulation. To obtain spherical components of the transmitting characteristic for instance, the z-component is first obtained from the transversality relation

$$\underline{s}_{10}(\underline{K}) \cdot \underline{k} = 0, \tag{8}$$

which may be written

$$s_{10z}(\underline{K}) = \frac{-k_x s_{10x}(\underline{K}) - k_y s_{10y}(\underline{K})}{\gamma}. \tag{9}$$

In these and following equations, the small "s" will denote the complete vector, and the capital "S" will denote its transverse components. This may be expressed by the equation,

$$\underline{s}_{10}(\underline{K}) = \underline{S}_{10}(\underline{K}) + s_{10z}\underline{e}_z(\underline{K}) \tag{10}$$

The spherical components for the usual spherical coordinate system shown in figure 3 are then obtained from the relations

$$\underline{e}_\theta = \cos\theta\ \underline{\kappa}_1 - \sin\theta\ \underline{e}_z, \tag{11a0}$$

$$\underline{e}_\phi = \underline{\kappa}_2. \tag{11b}$$

Additional insight into the character of $\underline{S}_{10}(\underline{K})$ and $\underline{S}_{01}(\underline{K})$ may be obtained by comparing them to familiar quantities such as the far electric field and a measured antenna pattern. If the magnitude of one component of either $\underline{S}_{10}(\underline{K})$ or $\underline{S}_{01}(\underline{K})$ is plotted as a function k_x and k_y, the plot closely resembles

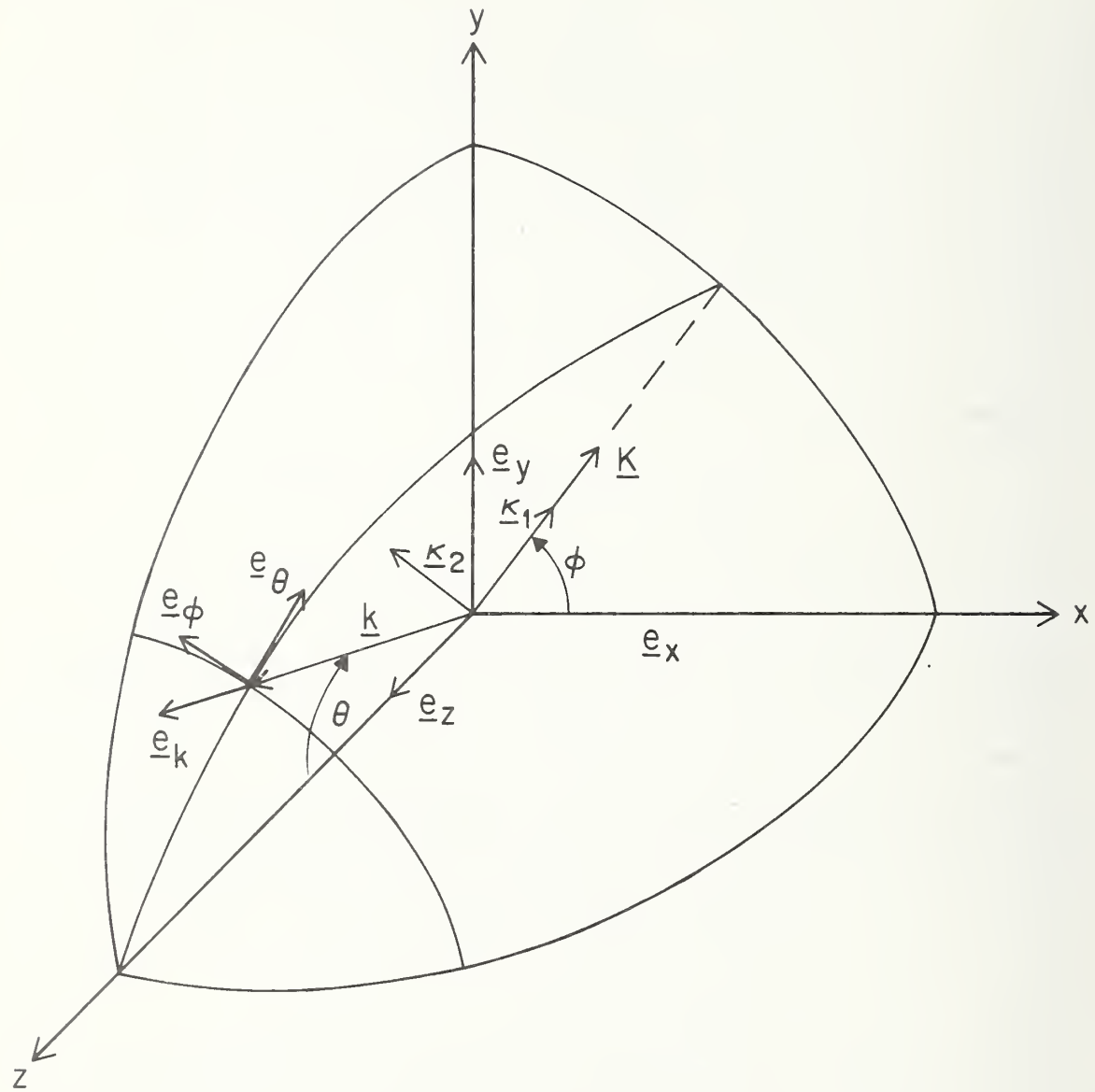

Figure 3. Relative Orientations of Orthogonal Unit Vector triads; $\underline{e}_x$, $\underline{e}_y$, $\underline{e}_z$; $\underline{\kappa}_1$, $\underline{\kappa}_2$, $\underline{e}_z$; $\underline{e}_\theta$, $\underline{e}_\phi$, $\underline{e}_k$.

a 3-dimensional antenna pattern. There is a simple relationship between $S_{10}(\underline{K})$ and the far-electric field which is obtained from the asymptotic value of the integral relation between $\underline{S}_{10}(\underline{K})$ and the electric field at arbitrary distance [1]. In the direction specified by the unit vector $\frac{\underline{k}}{|\underline{k}|}$, and at a large distance ρ from the antenna, the electric field is given by

$$\underline{E}(\underline{\rho}) = \frac{-i\gamma \underline{s}_{10}(\underline{K}) a_0 e^{ik\rho}}{\rho}, \tag{12}$$

where $\underline{\rho} = \rho \frac{\underline{k}}{|\underline{k}|}$. If this equation is inverted to give $\underline{s}_{10}(\underline{K})$ in terms of $\underline{E}$ the relation is more apparent,

$$\underline{s}_{10}(\underline{K}) = \frac{i}{\gamma a_0} \left[\underline{E}(\underline{\rho}) \rho \, e^{-ik\rho}\right]. \tag{13}$$

Since in the far-field the magnitude of $\underline{E}$ varies as $1/\rho$ and its phase change is given by $e^{ik\rho}$, the quantity in the brackets is a far-field distance-invariant quantity referred to as the radiation vector which expresses the vector pattern of the antenna as a function of direction. The transmitting characteristic $\underline{s}_{10}(\underline{K})$ also contains this information, but it is modified by the factor $1/\gamma$ which varies with direction, where $\gamma = k \cos\theta$, and θ is the angle between $\underline{k}$ and $\underline{e}_z$.

Far-field quantities may therefore be obtained quite easily in terms of $\underline{s}_{10}(\underline{K})$ but in addition, it can be used to formulate near-field antenna measurement situations more compactly than $\underline{E}$ or the radiation vector. For instance the power gain and effective area functions are given by

$$G(\underline{K}) = \frac{4\pi Y_0 k^2 [|S_{10}(1,\underline{K})|^2 + |S_{10}(2,\underline{K})\gamma/k|^2]}{\eta_0(1-|S_{00}|^2)} \tag{14}$$

$$\sigma(\underline{K}) = \frac{4\pi^2 \eta_0 [|S_{01}(1,\underline{K})\gamma/k|^2 + |S_{01}(2,\underline{K})|^2]}{1 - |S_{00}|^2}, \qquad (15)$$

where Y_0 is the value of $\sqrt{\varepsilon/\mu}$ for the transmission medium.

The goal of near-field measurements is then to determine $\underline{S}_{10}(\underline{K})$ or $\underline{S}_{01}(\underline{K})$ for the values of $\underline{K}$ which are of interest. One of the key equations in the near field measurement approach is referred to as the transmission integral. It relates the transmission and receiving characteristics of the test and probe antennas to the observed data. This equation will now be discussed for the case where the test antenna is used as the transmitter.

Suppose that the transmission characteristic of the test antenna is given by $\underline{S}_{10}(\underline{K})$ when it is placed in a specific orientation in the reference coordinate system. It should be noted that the S-parameters do depend in part on the orientation of the antenna. A convenient arrangement is to define a set of antenna coordinates fixed to the antenna and orient the antenna in the reference measurement system of figure 2 such that the two coordinate systems are coincident. In this way the measured parameters will be defined with respect to the antenna coordinate system. The x- and y-axes of the antenna are defined by reference marks on the antenna structure. The z-axis is chosen in some clearly defined direction, such as perpendicular to the aperture.

Now suppose that the probe antenna has a receiving characteristic $\underline{R}_{01}(\underline{K})$ when it is placed in the prescribed orientation in the reference system. Let the probe be placed in the receiving orientation by a 180° rotation about the y-axis and a translation along the z-axis to z = d. In its new orientation, the probe receiving characteristic will be denoted by

$\underline{R}'_{01}(\underline{K})$. The rectangular components in the two orientations are related by the equations

$$R'_{01x}(k_x,k_y) = -R_{01x}(-k_x,k_y) \tag{16a}$$

$$R'_{01y}(k_x,k_y) = R_{01y}(-k_x,k_y). \tag{16b}$$

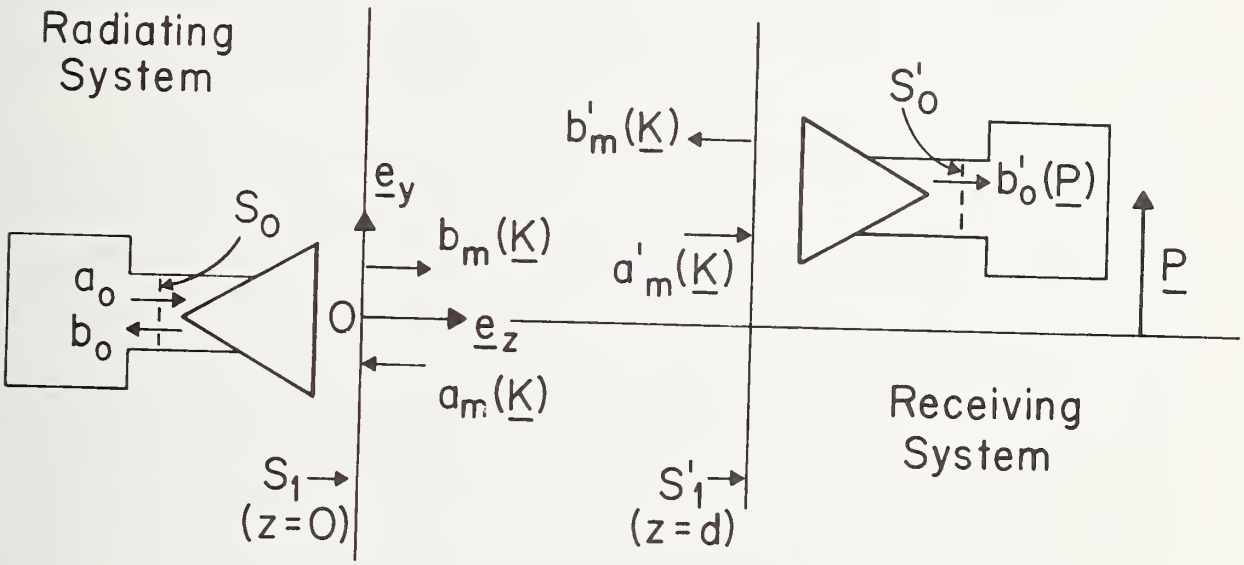

Figure 4. Relative Orientations of the Test Antenna and Probe.

Let the receiving probe be moved in the plane z = d by a transverse displacement $\underline{P} = x\,\underline{e}_x + y\,\underline{e}_y$. The two antennas are shown schematically in figure 4. If we now assume that the multiple reflections between the antennas are small enough to neglect, the transmission equation is given by

$$b'_0(\underline{P}) = \frac{a_0}{(1-\Gamma_\ell R_{00})} \int \left[\underline{R}'_{01}(\underline{K})\cdot\underline{S}_{10}(\underline{K})e^{i\gamma d}\right] e^{i\underline{K}\cdot\underline{P}}\, d\underline{K}. \tag{17}$$

It should be pointed out at this point that $b_0'(\underline{P})$ is the actual observed quantity, and that the product in the brackets, and more specifically $\underline{S}_{10}(K)$, is the desired result. Since eq. (17) is a Fourier integral transformation, we may write

$$D'(\underline{K}) = \underline{R}_{01}'(\underline{K}) \cdot \underline{S}_{10}(\underline{K}), \tag{18}$$

where $D'(\underline{K})$ denotes the determinate function of K given by

$$D'(\underline{K}) = \frac{e^{-i\gamma d}(1-\Gamma_\ell R_{00})}{4\pi^2 a_0} \int b_0'(\underline{P}) e^{-i\underline{K}\cdot\underline{P}} \, d\underline{P}. \tag{19}$$

Equation (18) gives one equation for the two transverse components of $\underline{S}_{10}(\underline{K})$ in terms of the function determined from the measurements, $D'(\underline{K})$, and the probe receiving characteristic, $R_{01}'(\underline{K})$. A second equation is required and is obtained by repeating the measurement with a second "independent" probe. This second probe may be obtained in effect by simply rotating the original probe about its axis by 90° unless the probe is circularly polarized. The second equation is then

$$D''(\underline{K}) = \underline{R}_{01}''(\underline{K}) \cdot \underline{S}_{10}(\underline{K}), \tag{20}$$

where

$$D''(\underline{K}) = \frac{e^{-i\gamma d}(1-\Gamma_\ell R_{00})}{4\pi^2 a_0} \int b_0''(\underline{P}) \, e^{-i\underline{K}\cdot\underline{P}} \, d\underline{P} \tag{21}$$

and $b_0''(\underline{P})$ and $R_{01}''(\underline{K})$ are respectively the received signal and probe receiving characteristic for the second orientation.

An alternative form of eqs. (18) and (20) employs the complete vectors rather than the transverse parts and may be of more use in many applications than the original form.

It can be shown [7] that

$$D'(\underline{K}) = \underline{R}'_{01}(\underline{K})\cdot\underline{S}_{10}(\underline{K}) = \underline{r}'_{01}(\underline{K})\cdot\underline{s}_{10}(\underline{K}) = r'_{01\theta}(\underline{K})s_{10\theta}(\underline{K}) + r'_{01\phi}(\underline{K})s_{10\phi}(\underline{K}), \quad (22)$$

where again the small r and s denote the complete vectors. If eq. (13) is now used to substitute $\underline{E}$ for $\underline{s}_{10}$, the coupling product can be expressed in terms of the spherical components of the far-electric field.

$$D'(\underline{K}) = \frac{i\rho e^{-ik\rho}}{\gamma a_0}\left[\underline{r}'_{01}(\underline{K})\cdot\underline{E}_s(\underline{\rho})\right] . \quad (23)$$

It can also be shown that the reciprocity relationship between the complete spectral vectors is given by

$$\underline{s}_{01}(\underline{K}) = \frac{Y_0\gamma}{\eta_0 k}\,\underline{s}_{10}(-\underline{K}). \quad (24)$$

If the probe is reciprocal, then eqs. (24) and (13) may be used to express $\underline{s}'_{01}(\underline{K})$ in terms of the far-electric field which the probe would produce at a distance ρ' with input amplitude a'_0. The coupling product may then be expressed completely in terms of familiar electric field quantities,

$$D'(\underline{K}) = -\frac{Y_0\rho\rho' e^{-ik(\rho+\rho')}}{\eta_0 k\gamma a_0 a'_0}\left[\underline{E}'_r(\rho')\cdot\underline{E}_s(\rho)\right], \quad (25)$$

where $\underline{E}'_r$ and $\underline{E}_s$ denote the electric fields of the probe and test antennas respectively. Equation (22) is more useful than eq. (18) when the probe correction is given in spherical components and one desires the spherical components of either $\underline{s}_{10}$ or $\underline{E}$ as the field results. When this form is used, it is not necessary to transform from the rectangular to the spherical components, and the number of calculations is therefore reduced.

The steps in the measurement and computation may be summarized as follows.

1. Define the coordinate axes of the reference measurement system, the test antenna, and the probe.
2. Measure or calculate from theory the probe receiving characteristic for all values of $\underline{K}$ for which the test antenna characteristics are to be determined.
3. Place the test antenna and probe in the measurement system in the prescribed orientation and verify that multiple reflections are small enough to neglect.
4. Measure $b_0'(\underline{P})$ and $b_0''(\underline{P})$ over a sufficient area and at adequate spacing in x and y. (Defining the scan parameters is one of the main tasks of this program.)
5. Evaluate the integrals in eqs. (19) and (21) and solve eqs. (18) and (20) for the two transverse components of $\underline{S}_{10}(\underline{K})$.
6. Compute power gain, spherical components, polarization ratios or other desired quantities, or use $\underline{S}_{10}(\underline{K})$ to obtain the field in any other transverse plane to evaluate antenna performance.

Each of these topics will be discussed in more detail in the following sections, with special reference to the application of this project.

3.0 Measurement Program

3.1 Test Antennas, Probe, and Initial Alignment

Two test antennas were used during the first series of tests. The first is shown in figure 5 and is called a constrained lens array. It is a fixed-beam array composed of 1788 elements which are space fed from an eight-horn feed.

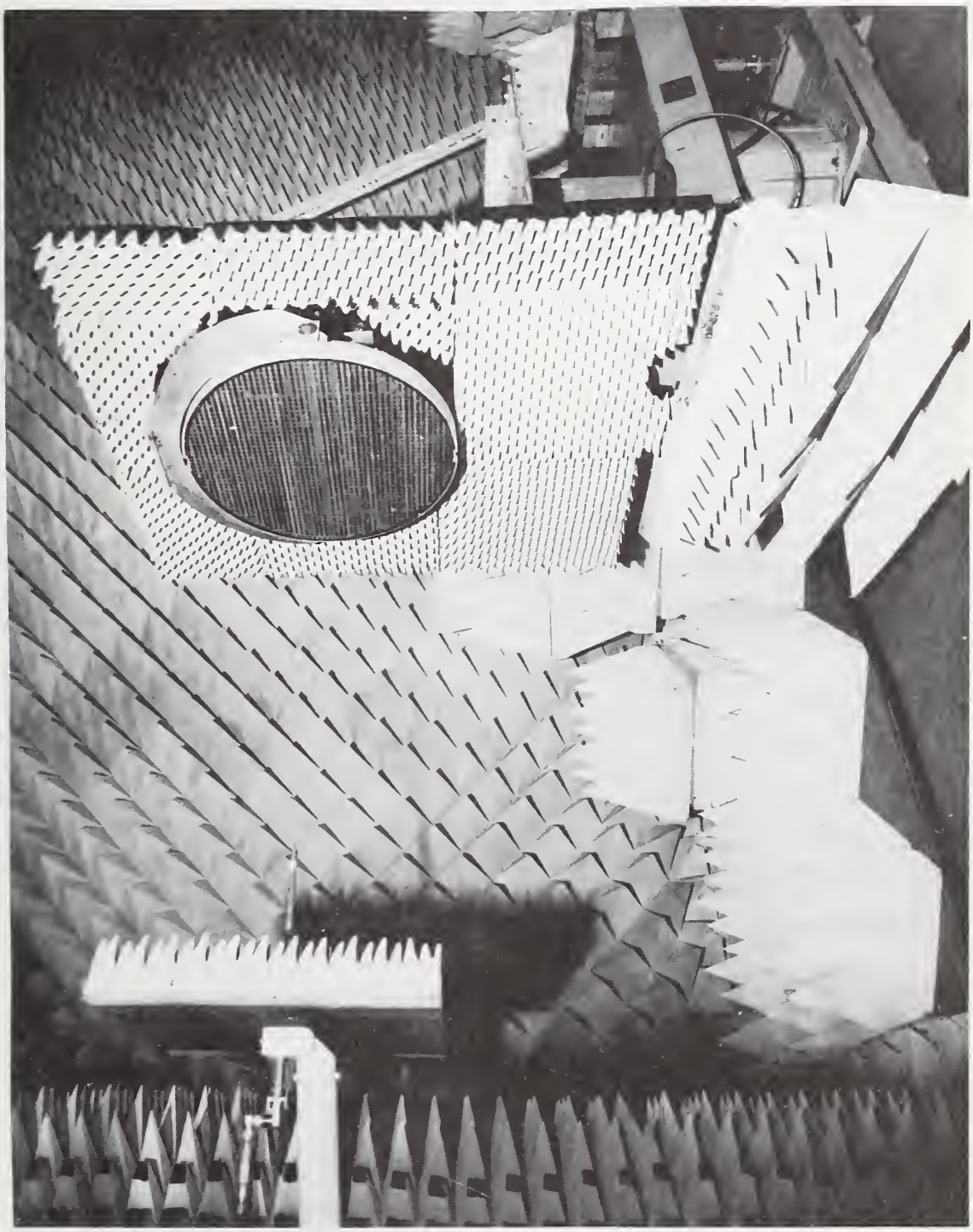

Figure 5. Constrained Lens Antenna and Probe.

The principal features of this antenna are that it has sidelobes of about-30 dB over a fairly large frequency range, and operates in a sum and two difference modes. Since there are no ferrite devices in the array, it is a reciprocal antenna.

The second test antenna is shown in figure 6, and is referred to as the Volphase (Volumetric Phase Scanning) array. It is a corporate fed phased array composed of 1600 elements. The array is steerable to ± 45° in both azimuth and elevation and also operates in both sum and monopulse difference modes.

The probe which was used for most of these measurements is also shown in both of the figures. It was an open-ended section of WR90 waveguide. The waveguide provides a simple probe which possesses a number of advantages when patterns are to be determined out to fairly wide angles. Its pattern is smoothly varying without nulls, and the magnitude of the relative probe correction is fairly uniform over a large angular region. Its axial ratio is approximately 40 dB; it provides a small scattering cross section; and its gain can be measured to high accuracy.

The probe receiving characteristic is obtained by measuring its relative far-field patterns for both polarizations and its gain in the boresight direction. If the probe is placed on a rotator which is in the far-field of a source antenna, and rotated through the angles θ and ϕ, then from the asymptotic (large d) form of eq. (17) expressed in terms of spherical components,

$$\frac{b_0'(\theta,\phi)}{b_0'(0,0)} = \frac{\underline{r}_{01}'(-\theta,-\phi)\cdot\underline{E}_s(\underline{\rho})}{\underline{r}_{01}'(0,0)\cdot\underline{E}_s(\underline{\rho})} . \qquad (26)$$

If the polarization characteristics of the source antenna are known, then the measured patterns (both amplitude and phase for two polarizations of the source) give the relative probe

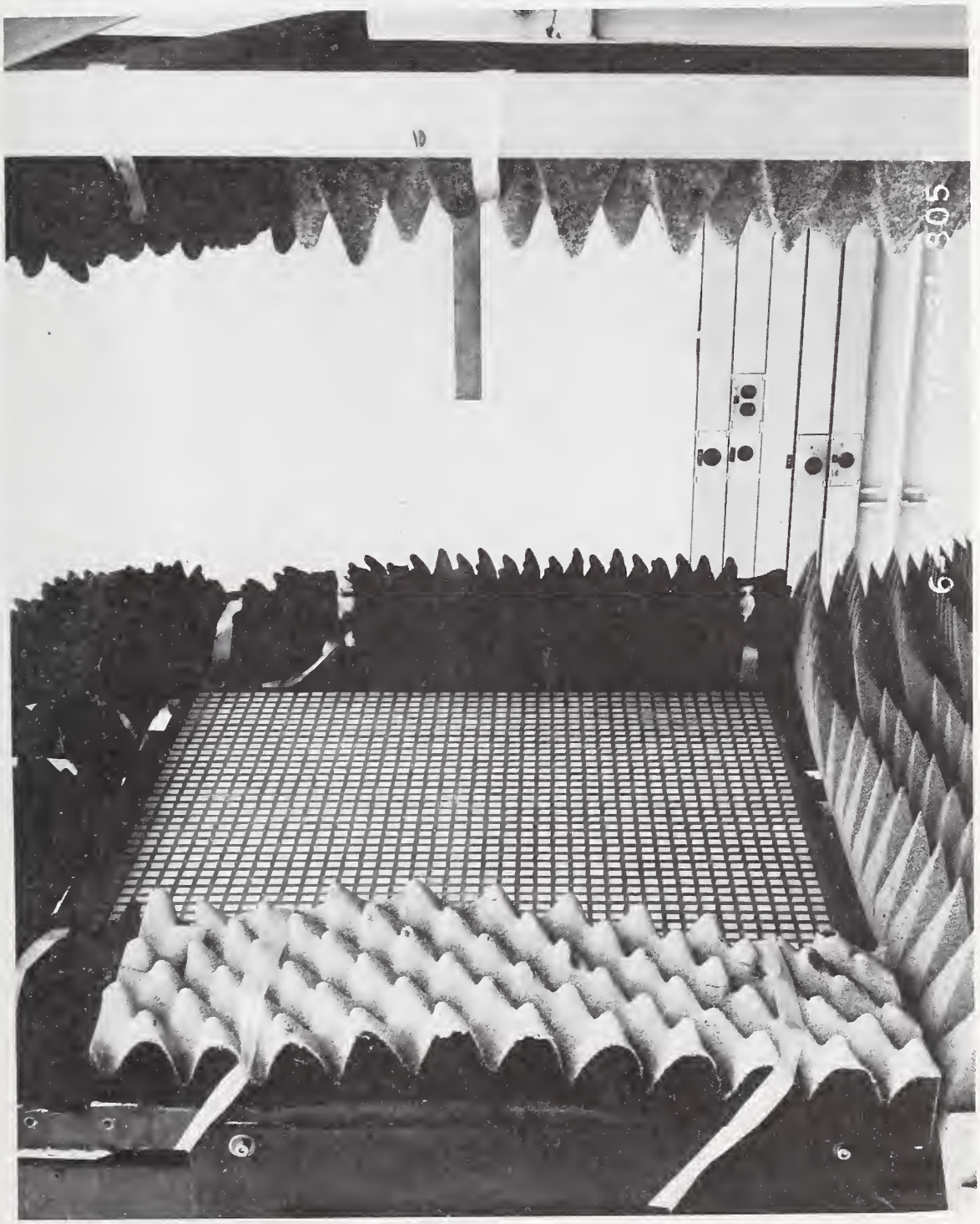

Figure 6. Volphase Antenna and Probe.

correction data for the two spherical components of $\underline{r}'_{01}(\underline{K})$. These relative values are sufficient if only relative patterns of the test anenna are required. If absolute power gain is required, then the power gain of the probe must also be measured. In all of this and past work, the necessary data have been obtained to give the absolute as well as relative patterns.

The reference coordinate system for measurements made on each test antenna is defined with the x-axis horizontal, the y-axis vertical, and the z-axis in the center of, and normal to the plane of the scanner.

The scanner used to make measurements with the constrained lens antenna is a large mechanical structure which moves the probe over the required area and is shown in figure 7. A variety of tests were carried out initially to align the scanner so that its measurement plane was vertical, and the probe motions orthogonal. Reference lines were scribed on the antennas and probe to define their x- and y-axes, and then precision transits and autocollimators were used to place the test antenna's axes coincident with the reference coordinate system.

The measurement system is shown schematically in figure 8. This system provides the programming control to the positioner to move the probe in a raster-type scan. During the scan, the phase and amplitude of the probe output signal are automatically recorded at preset intervals in x and y.

Measurements with the Volphase antenna were made at a different site than those on the constrained lens, and the large scanner was not available. They demonstrate quite dramatically that good results are possible using the near-field scanning technique without ideal measurement conditions. The measurement setup in figure 9 shows the smaller scanner

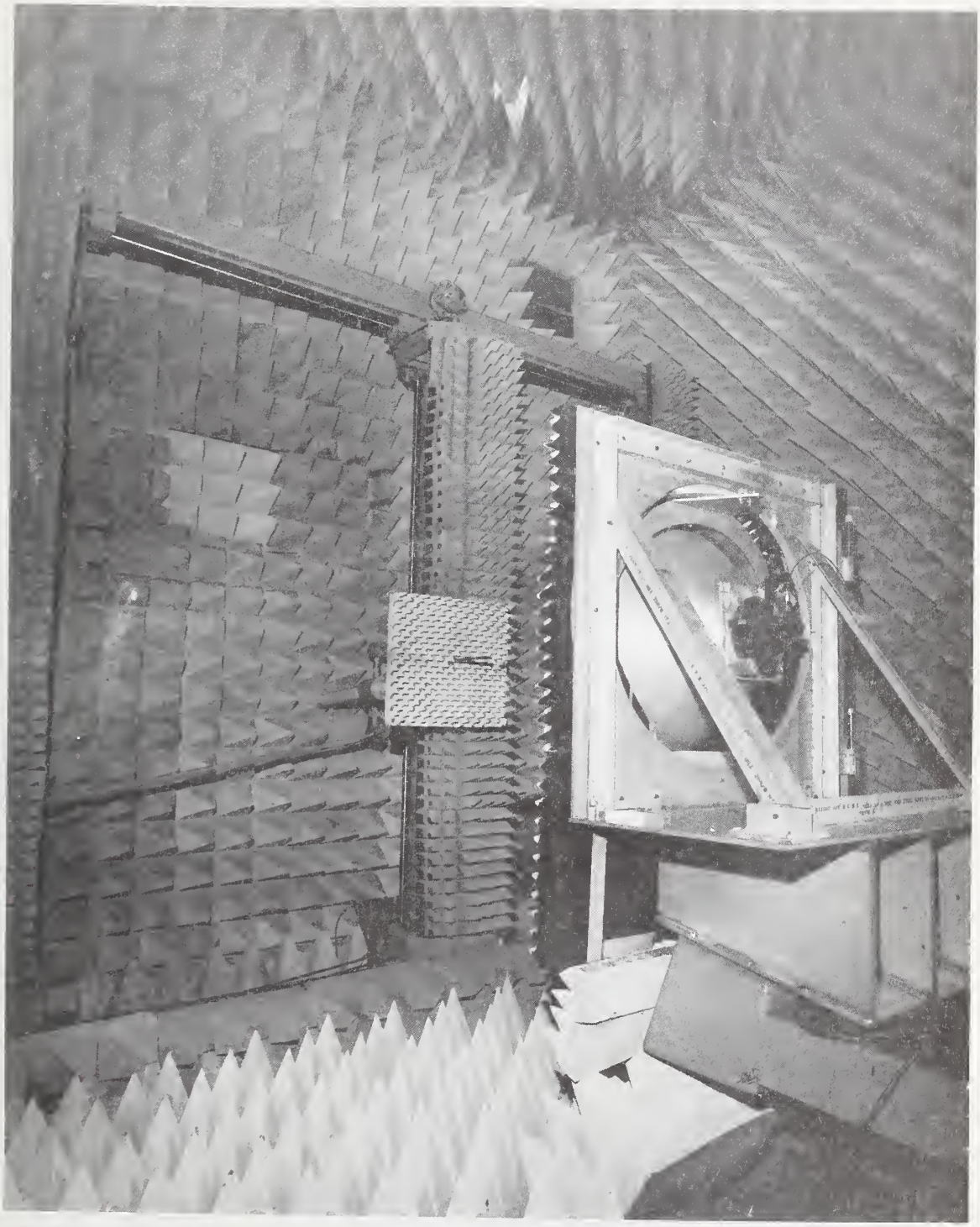

Figure 7. Scanner for Moving Probe in x-y Plane.

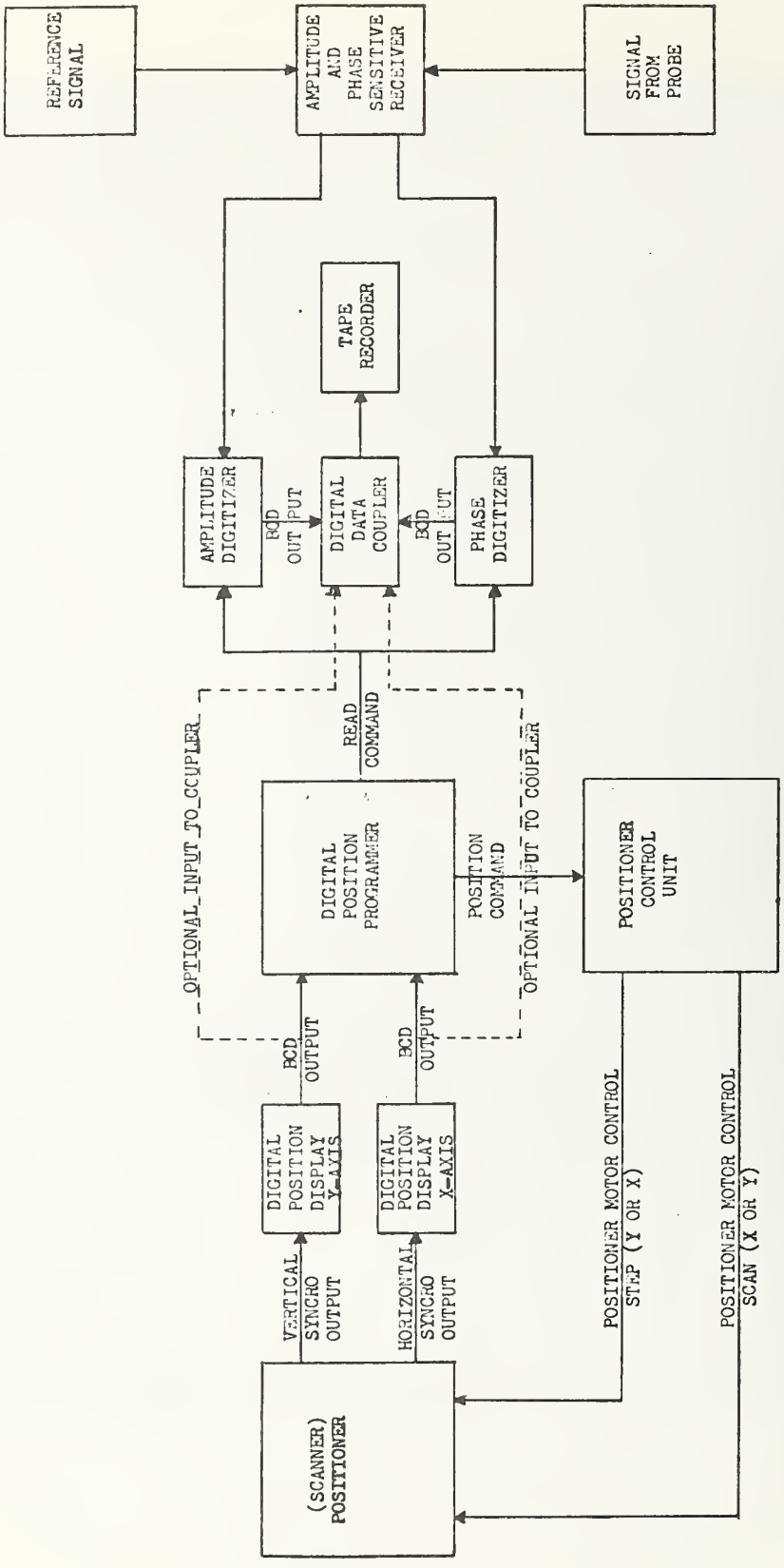

Figure 8. Block Diagram of Automatic Position and Measurement System.

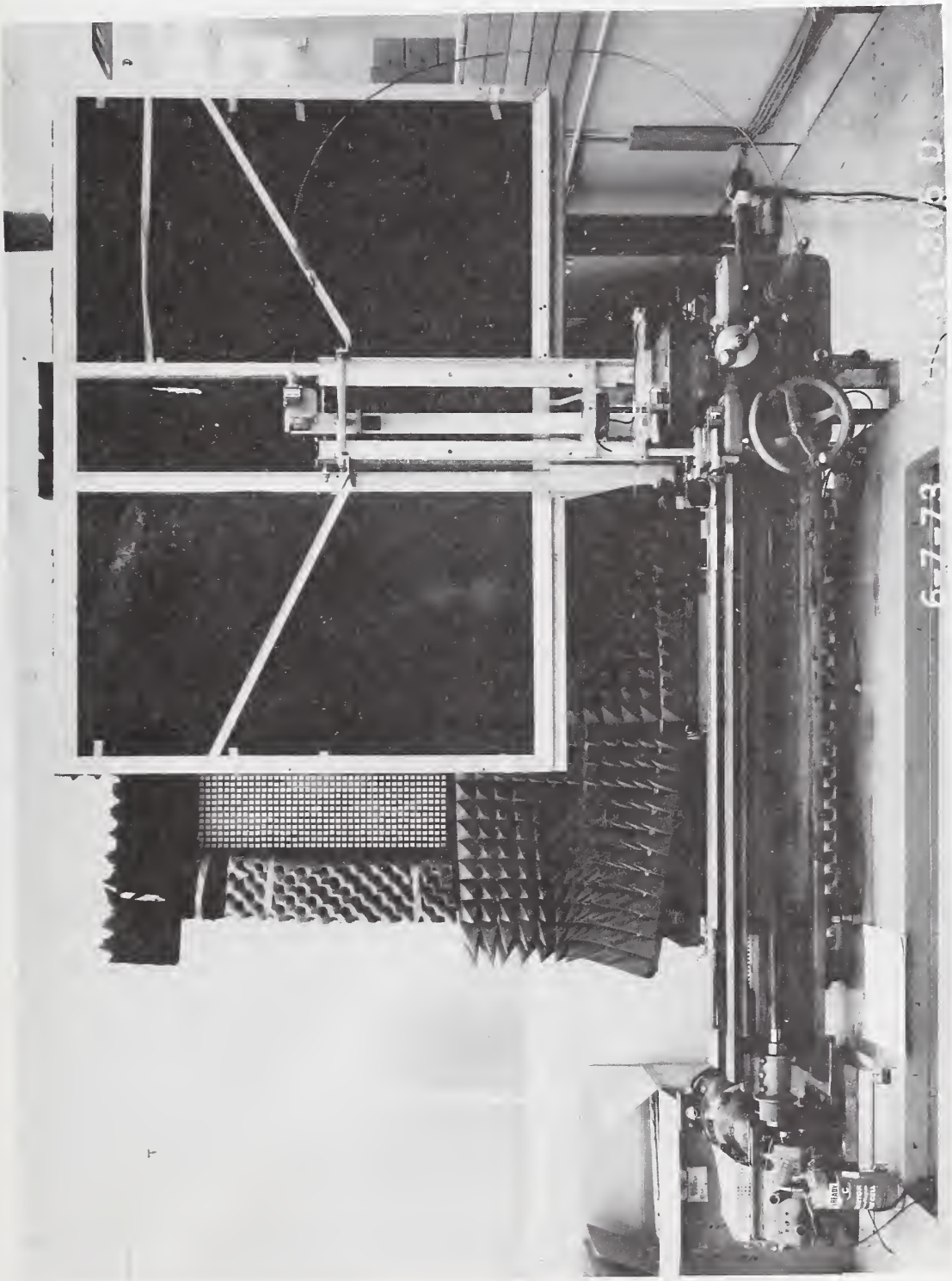

Figure 9. Scanner Used for Volphase Antenna.

used and the limited amount of absorbing material necessary. Figure 10 shows the room in which the measurements were made. In this environment, larger multiple reflections would be expected, and yet as the tests described in section 3.2.4 verify, their effect was quite small.

Near-field measurements were made on these two test antennas under a wide variety of conditions in order to meet the objectives outlined in section 1. These included, for instance, different beam steering direction, different scan lengths and point spacings, the presence or absence of a radome, simulated antenna faults, and use of the test antenna as a transmitter and as a receiver. Only part of the voluminous amount of data obtained from these measurements has been completely analyzed at this time, and this report will deal primarily with that data which has been analyzed and the conclusions which were derived from the completed tests. Tables 1-4 summarize the various measurements which were performed under the headings of centerline data and two-dimensional data. The centerline data were obtained by moving the probe along the lines x=0 and/or y=0 and recording the probe output amplitude and phase. These data were used in preliminary type tests to be discussed in the next section. The complete two-dimensional data were used to obtain complete and detailed far-field parameters, and the results of these tests will be discussed in a later section.

3.2 Determining Scan Parameters and the Effects of Multiple Reflections

The parameters to be determined were the scan lengths L_x and L_y, and the spacings between data points δ_x and δ_y. To determine these, and to estimate the effects of multiple reflections, a series of tests were performed using centerline data.

Figure 10. Near-Field Measurement Setup for Electronically Steerable Phased Array Antenna.

Table 1. Summary of Constrained Lens Array Centerline Data (X&Y)

Measurement Port	Mode	Array Az. (deg)	Steering El. (deg)	Measurement Distance (cm)	Radome	Scan Length (cm)	Type of Measurement
Sum	Xmit	0,20,38	0,20	25.4	No	213.4	Scan Parameter Determination
"	"	0,20	0	" + $\frac{n\lambda}{4}$	"	177.8	Multipath Evaluation
"	Rec	0	0	"	"	127.0	Single and Multiple Faulty Elements
"	"	"	"	" + $\frac{n\lambda}{4}$	"	"	Multipath Evaluation
"	Xmit	0,20,38	0,10	117.6	"	213.4	Scan Parameter Determination
"	"	"	0	"	"	250.2	Beam Shift, Array Offset 71 cm in X
"	"	0,20	0,10	254.6	"	213.4	Beam Shift
"	"	"	0	"	"	250.2	Beam Shift, Array Offset 71 cm in X
"	"	0	0	"	"	127.0	Single and Multiple Faulty Elements
"	"	"	"	"	"	152.4	" " " " "
"	Rec	"	"	" + $\frac{n\lambda}{4}$	"	127.0	Multipath Evaluation
"	Xmit	"	"	"	Yes	228.6	
"	"	"	"	"	"	"	Faulty Radome
"	"	0,20	"	"	"	"	Beam Shift, Array Offset 71 cm in X
"	Rec	0	"	" + $\frac{n\lambda}{4}$	"	"	Multipath Evaluation
El. Diff.	Xmit	0	0	25.4	No	177.8	
"	"	"	"	" + $\frac{n\lambda}{4}$	"	"	Multipath Evaluation
"	Rec	"	"	254.6 $\frac{n\lambda}{4}$	Yes	228.6	" "

Table 2. Summary of Constrained Lens Array Two Dimensional Data

Measurement Port	Mode	Measurement Distance (cm)	Radome	Scan Lengths L_x(cm)	Scan Lengths L_y(cm)	Faulty Elements	Faulty Radome	Type of Measurement
Sum	Xmit	25	No	152.4	152.4	No	No	
"	Rec	"	"	127.0	127.0	Yes	"	
Sum	Xmit	117	No	127.0	127.0	No	No	Freq. - 8.4 GHz
Sum	Xmit	254	No	152.4	152.4	No	No	
"	"	"	"	228.6	228.6	"	"	
"	"	"	"	152.4	152.4	Yes	"	
Sum	Xmit	254	Yes	228.6	228.6	No	No	
"	"	"	"	"	"	Yes	"	
"	"	"	"	"	"	No	Yes	
Sum	Xmit	254	No	228.6	228.6	No	No	Array offset 71 cm in X and 20° in azimuth.
Sum	Xmit	254	No	203.2	203.2	No	No	Cross Polarization
"	"	"	Yes	127.0	127.0	"	"	" "
Sum	Rec	254	Yes	228.6	228.6	No	No	
El. Diff.	Xmit	25	No	101.6	177.8	No	No	
"	Rec	"	"	"	"	"	"	
El. Diff.	Xmit	254	No	127.0	228.6	No	No	
"	"	"	Yes	"	"	"	"	
"	"	"	"	"	"	Yes	"	
El. Diff.	Xmit	254	No	127.0	228.6	No	No	Cross Polarization
"	"	"	Yes	"	127.0	"	"	" "
El. Diff.	Rec	254	Yes	127.0	228.6	No	No	
Az. Diff.	Xmit	254	Yes	228.6	228.6	No	No	Array Offset 71 cm in X
"	"	"	"	"	"	"	"	Rotated 20° in azimuth.
"	"	"	"	127.0	127.0	No	No	Cross Polarization
Az. Diff.	Xmit	254	Yes	228.6	157.5	No	No	
"	"	"	"	"	"	"	"	

Table 3. Summary of Volphase Array Centerline Data

Measurement Port	Azimuth Beam Position (deg)	Measurement Distance (cm)	Radome	Type of Measurement
Sum	0,30,45	38.1	No	Scan Parameter Tests
"	0,10,30	38.1 - $\frac{n\lambda}{4}$	"	Multipath Eval.
"	0,30	38.1	"	Cross Polarization
"	0,5	304.8	"	Scan Parameter Tests
"	"	304.8 - $\frac{n\lambda}{4}$	"	Multipath Eval.
"	"	304.8	"	Cross Polarization
"	"	"	Yes	Beam Shift
"	"	304.8 - $\frac{n\lambda}{4}$	"	Multipath Eval.
"	"	304.8	"	Cross Polarization
"	0	38.1	No	Faulty Elements
"	"	304.8	"	" "
"	"	"	Yes	" "
Az. Diff.	0,30	38.1	No	Beam Shift
"	0,5	304.8	"	" "
"	"	304.8 - $\frac{n\lambda}{4}$	"	Multipath Eval.
"	"	304.8	Yes	Beam Shift
"	"	304.8 - $\frac{n\lambda}{4}$	"	Multipath Eval.
"	"	304.8	"	Cross Polarization

Table 4. Summary of Volphase Array Two Dimensional Data

Measurement Port	Azimuth Beam Position (deg)	Measurement Distance	Radome
Sum	0	38.1 cm	No
"	5	"	"
"	30	"	"
"	45	"	"
"	0	304.8 cm	"
"	5	"	"
"	0	"	Yes
"	5	"	"
Az. Diff	0	38.1 cm	No
"	5	"	"
"	30	"	"
"	0	304.8 cm	"
"	5	"	"
"	0	"	Yes
"	5	"	"

A typical set of data for the constrained lens antenna along the centerline y=0, z=25 cm, is shown in figure 11. The first step in the processing is to compute the Fourier transform of these data in order to implement eq. (19) to obtain an approximate far-field pattern as shown in figure 12. This is an approximate pattern because only centerline data have been used and probe correction is ignored. For this to give correct results, the measured response must be expressible as a product function, i.e., $b_0'(x,y) = b_0'(0,y)\ b_0'(x,0)$. To the degree that this is valid, figure 12 is a plot of the relative magnitude of $D'(k_x,0)$ plotted as a function of the azimuthal angle A, which is related to k_x along the principal planes by

$$k_x = \frac{2\pi}{\lambda} \sin A.$$

Although this is not the actual far-field pattern, it is very useful for making these preliminary tests. One of the main advantages of these tests is that actual data for the particular antenna-probe pair serve as the basis upon which the scan parameters are determined.

3.2.1 Scan Area Determination

In principle, eqs. and (21) must be integrated over an infinite plane. This of course is not possible, and so we must determine what errors are introduced by using a finite areas, and the size of the area required for good accuracy. The use of a finite area is one of two approximations to the theory which must be evaluated. Since the scan area was very limited for measurements made with the Volphase antenna, these tests were performed primarily with the constrained lens antenna and its measurement system.

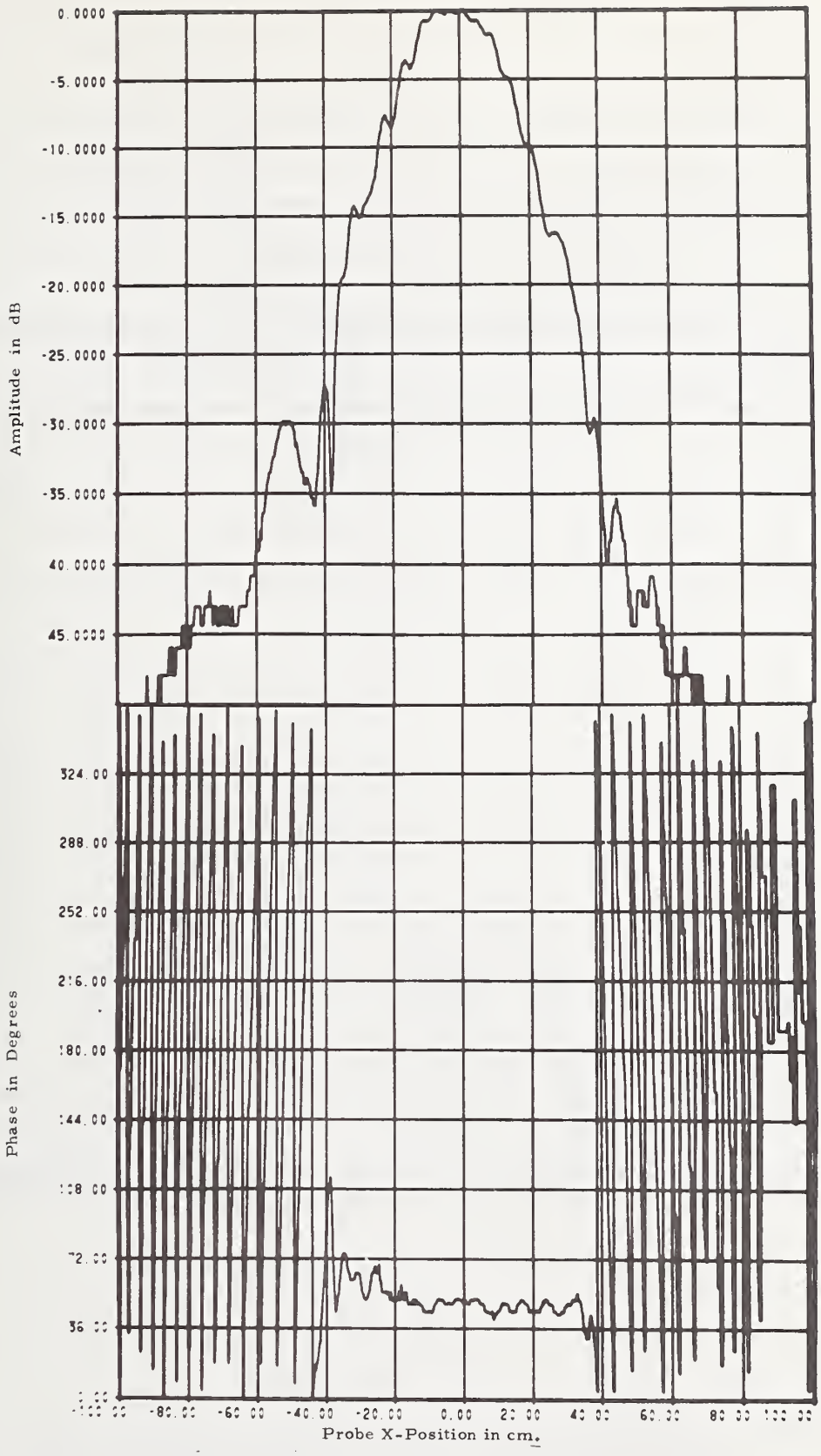

Figure 11. Near-Field Centerline Data, Constrained Lens Antenna, z = 25 cm, Az = EL = 0^{o}.

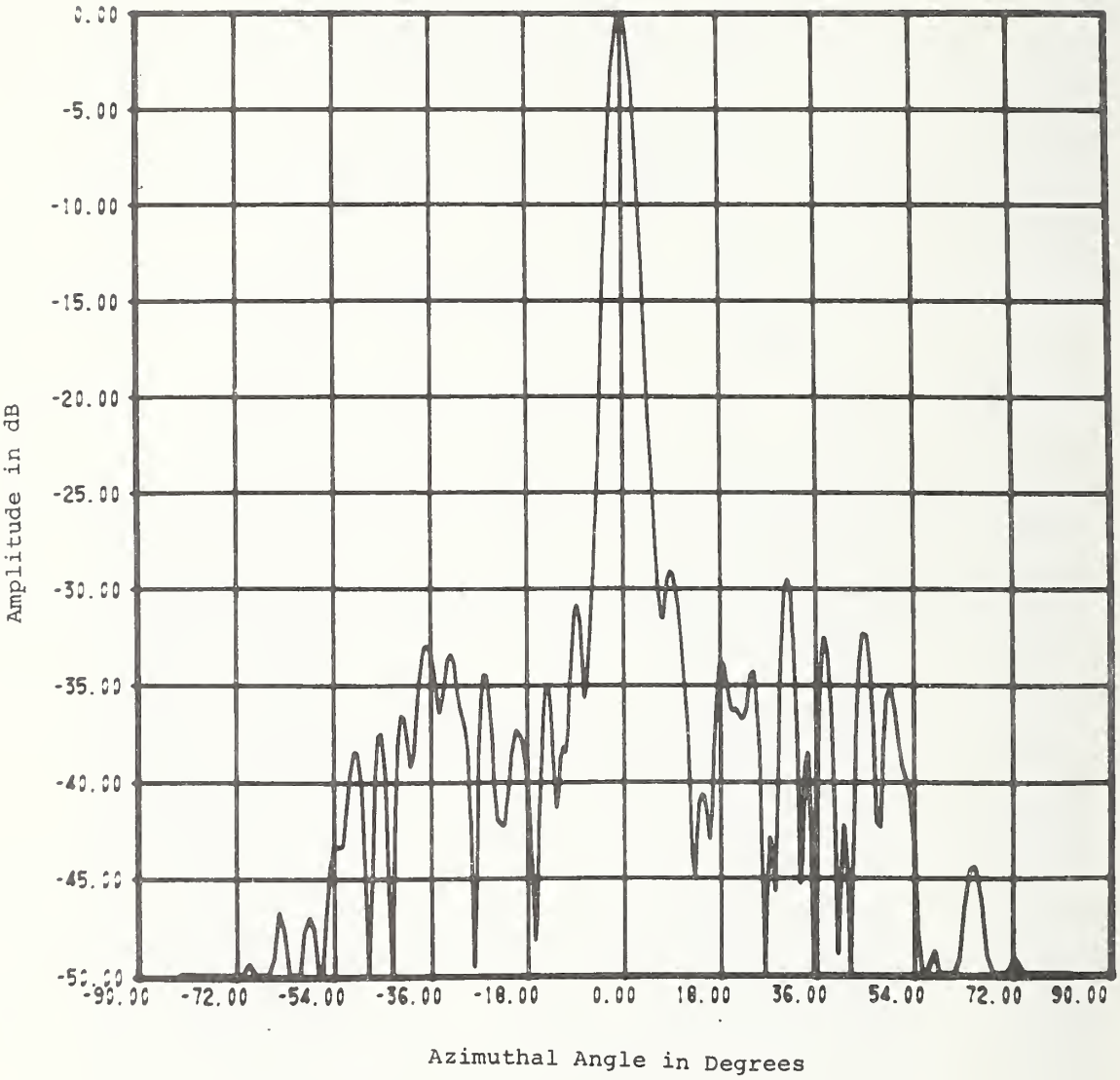

Figure 12. Approximate Far-Field Pattern Computed from Centerline Data Taken on Constrained Lens Antenna. z = 25 cm, Az = EL = 0°.

To determine the required scan length, data were taken over the maximum extent of the scanner. The transform is computed for the complete data set, and for subsets obtained by deleting points from each edge. The change in the transform was measured by computing the RMS and maximum differences in percent of the on-axis value, and the change in the on-axis gain. These quantities are shown plotted as a function of distance deleted from each edge and the ratio of scan length to antenna diameter a, in figures 13 and 14. It is evident from these curves that a scan length which is only slightly larger than the width of the antenna is sufficient for good accuracy at the indicated z-separation distance of 25 cm.

Figure 15 is a plot of the far-field pattern obtained from the complete centerline data and a plot of the difference between this pattern and the pattern obtained after deleting 50 cm from both edges of the near-field data shown in figure 11. This shows that the changes due to reducing the scan length occur primarily in the nulls, at wide angles, and where the pattern is below about 40 dB. This is generally true when the deleted data are in the region of rapidly increasing phase similar to the region bounded by $|x| > 40$ cm in figure 11. It is evident that the data in this region are primarily due to the field diffracted around the edges of the antenna and contribute mainly to the wide-angle regions of the far-field. The near-field for a well collimated antenna is conveniently divided into two regions. The area of relatively constant phase may be referred to as the collimated region, and the remaining region as the diffracted region. It is the collimated region which determines the primary structure of the far-field pattern and which must be retained in the measurement. This is further illustrated by figure 16 which shows the y=0 centerline data for z = 254 cm. The collimated region has

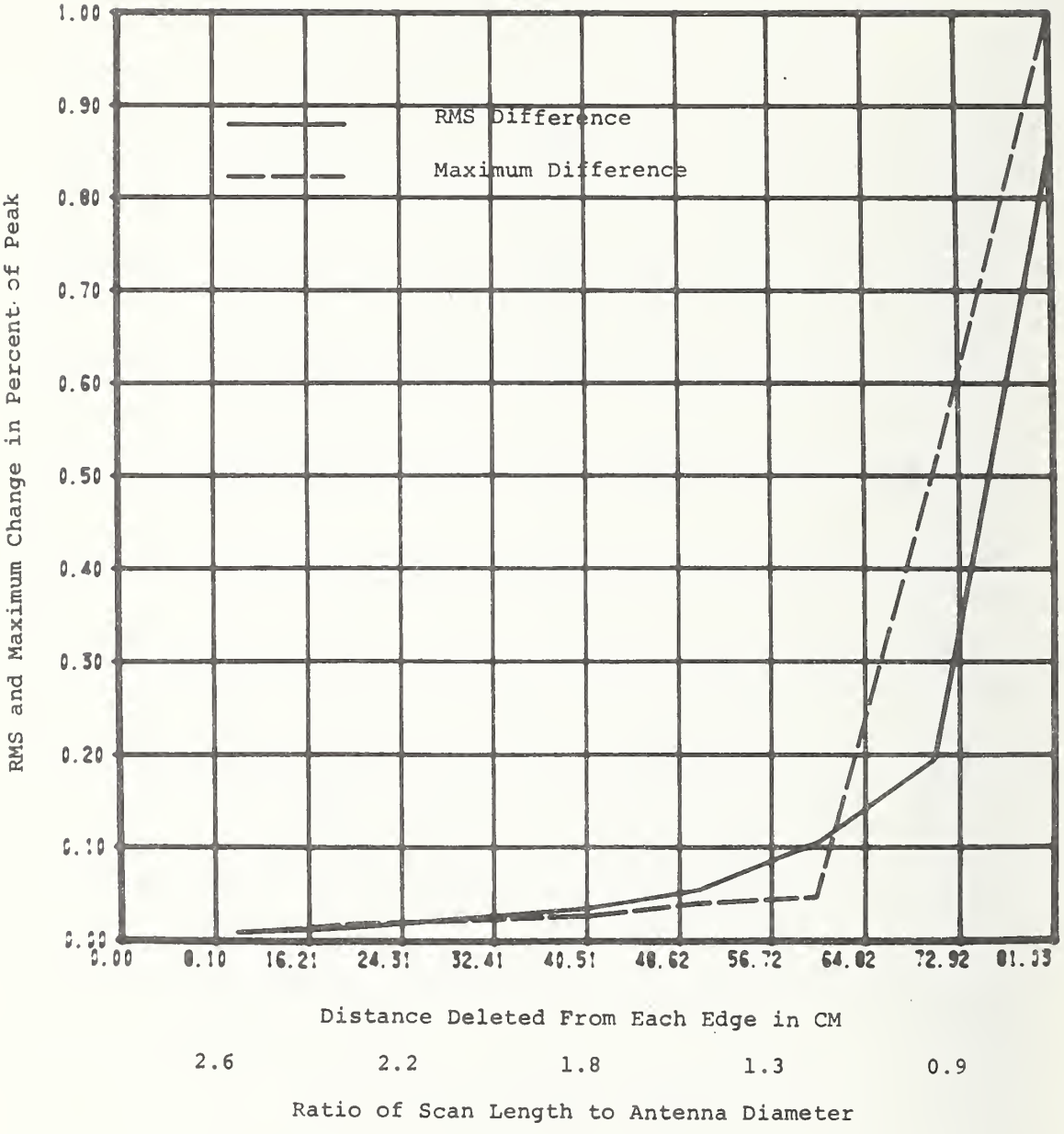

Figure 13. Change in Computed Far-Field Due to Decreasing Scan Length.

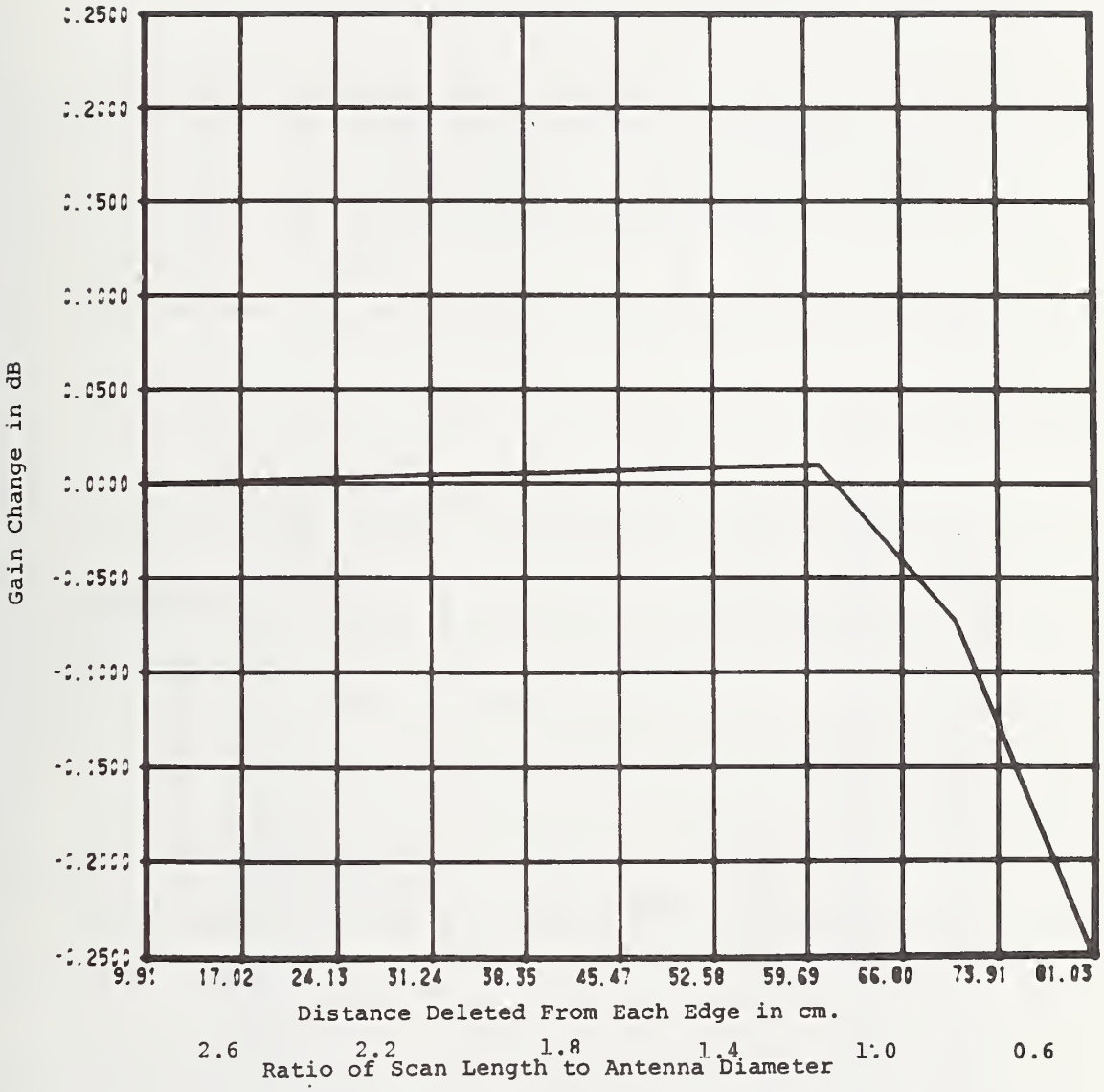

Figure 14. Change in Computed Gain Due to Decreasing Scan Length.

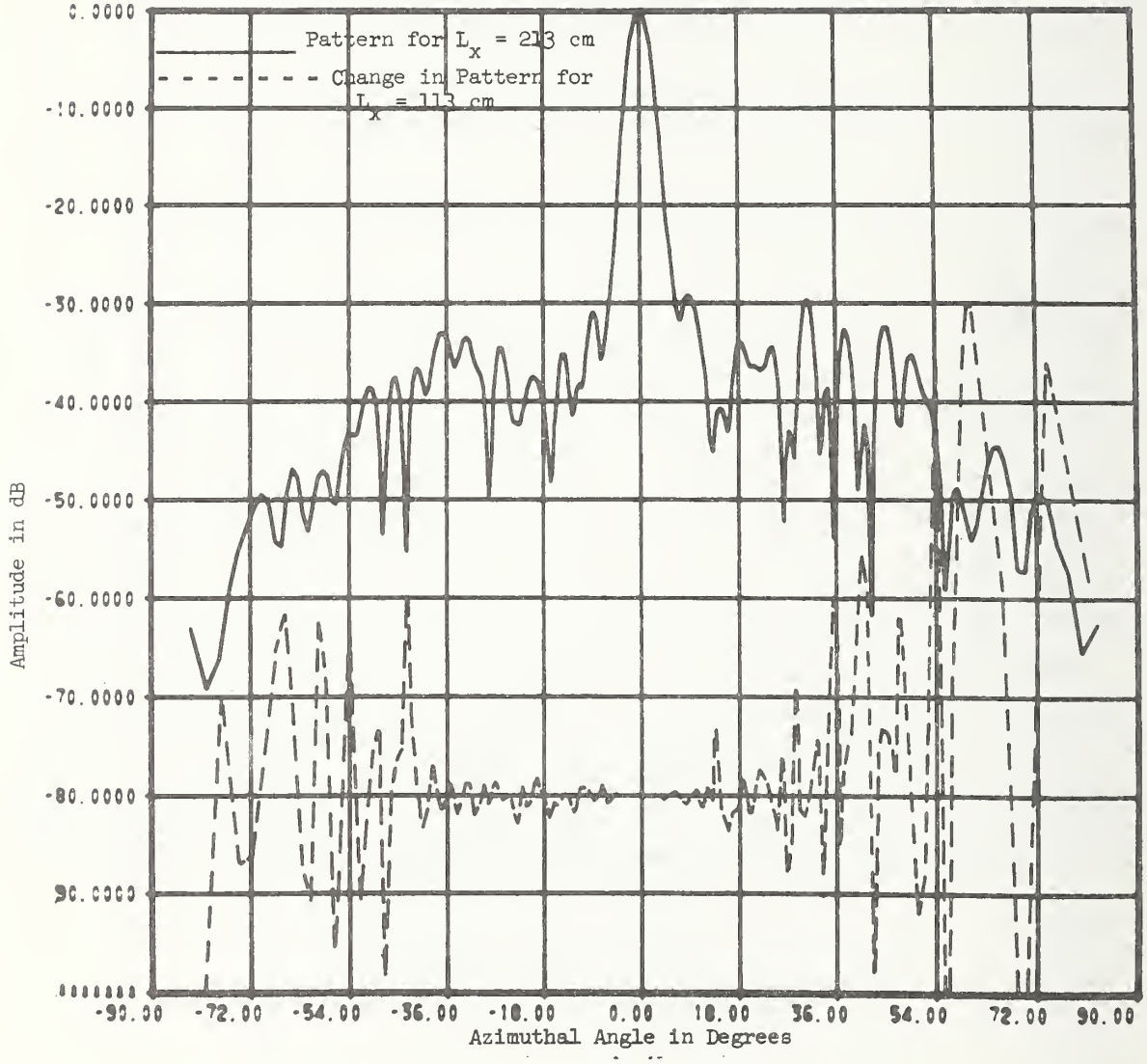

Figure 15. Change in Far-Field Pattern Due to Decreasing Scan Length, L_x = 213 cm and L_x = 113 cm.

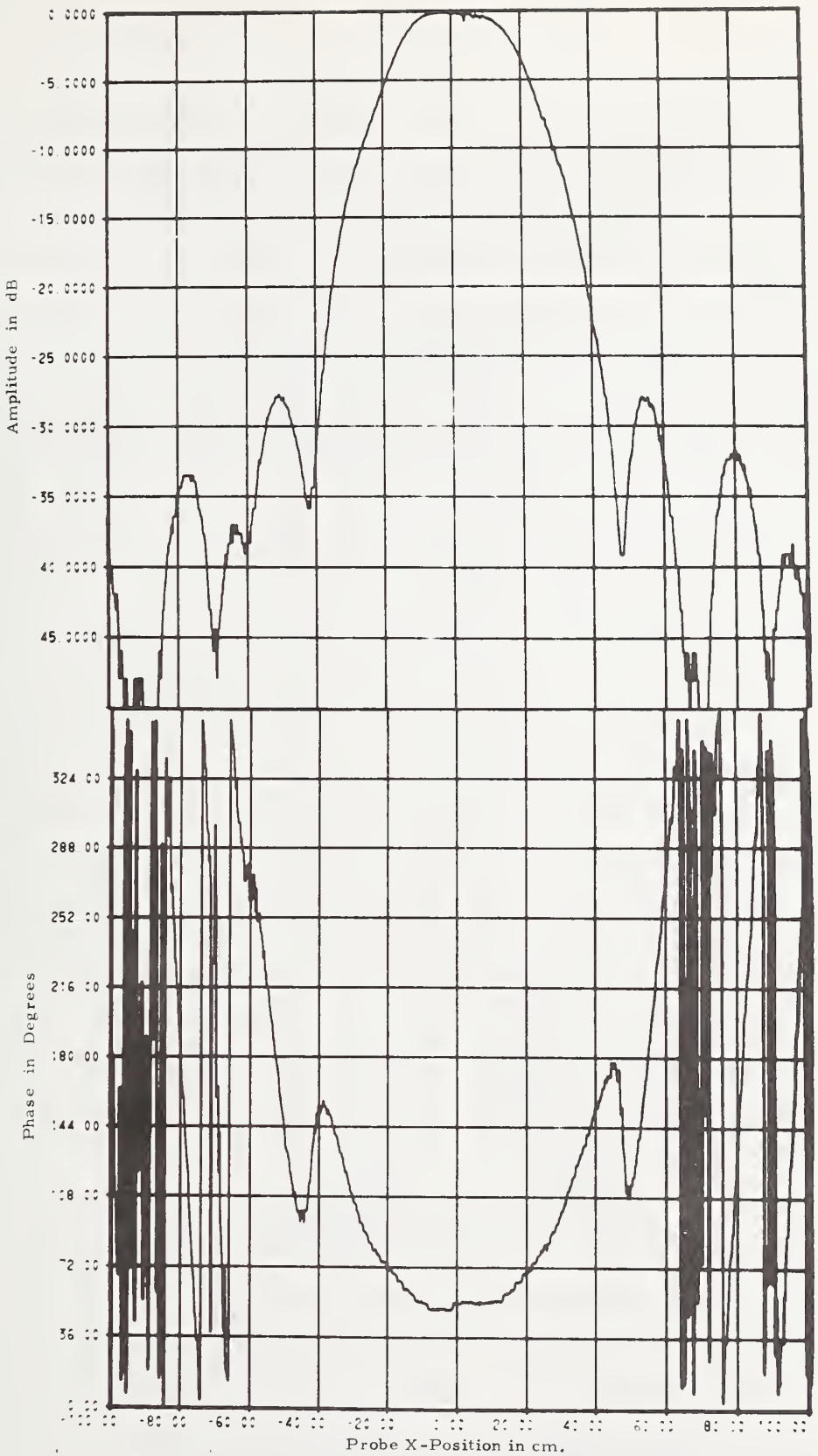

Figure 16. Near-Field Centerline Data, Constrained Lens Antenna, z = 254 cm, Az = EL = 0°.

increased somewhat to about $|x| \lesssim 60$ cm, and the scan length tests indicate that measurements over this interval will give good results for the principal part of the far field. There is, however, some loss of information at this distance if measurements are made over only the collimated region.

If we compare the far-field computed from the z = 254 cm data shown in figure 17 with that obtained from z = 25 cm data shown in figure 12, a significant change is apparent. Since only centerline data have been used, detailed agreement would not be expected, but the reduction of the sidelobes for angles greater than about 18 degrees is significant. Both patterns have been computed for scan lengths of 213 cm, and the decreased sidelobes in figure 17 are due to a spacial filtering resulting from increasing the z-distance while maintaining the same scan length. To a first approximation, this means that the portions of the transmitted spectrum which do not cross the measurement area are essentially filtered out of the measured data. From the tests which have been made, it appears that the far-field cutoff angle which results from this filtering can be estimated as equal to the angle between a normal to the measurement plane and a line from the edge of the antenna to the edge of the measurement plane as illustrated in figure 18. In terms of the scan length L_x, the distance between the two antennas d, and the antenna diameter a, the cutoff angle θ_c is given approximately by

$$\theta_c \simeq \tan^{-1}\left(\frac{L_x - a}{2d}\right). \qquad (27)$$

From tests on two-dimensional data, it appears that the cutoff angle is actually larger than this, but eq. (27) is useful in estimating the required size of the measurement area.

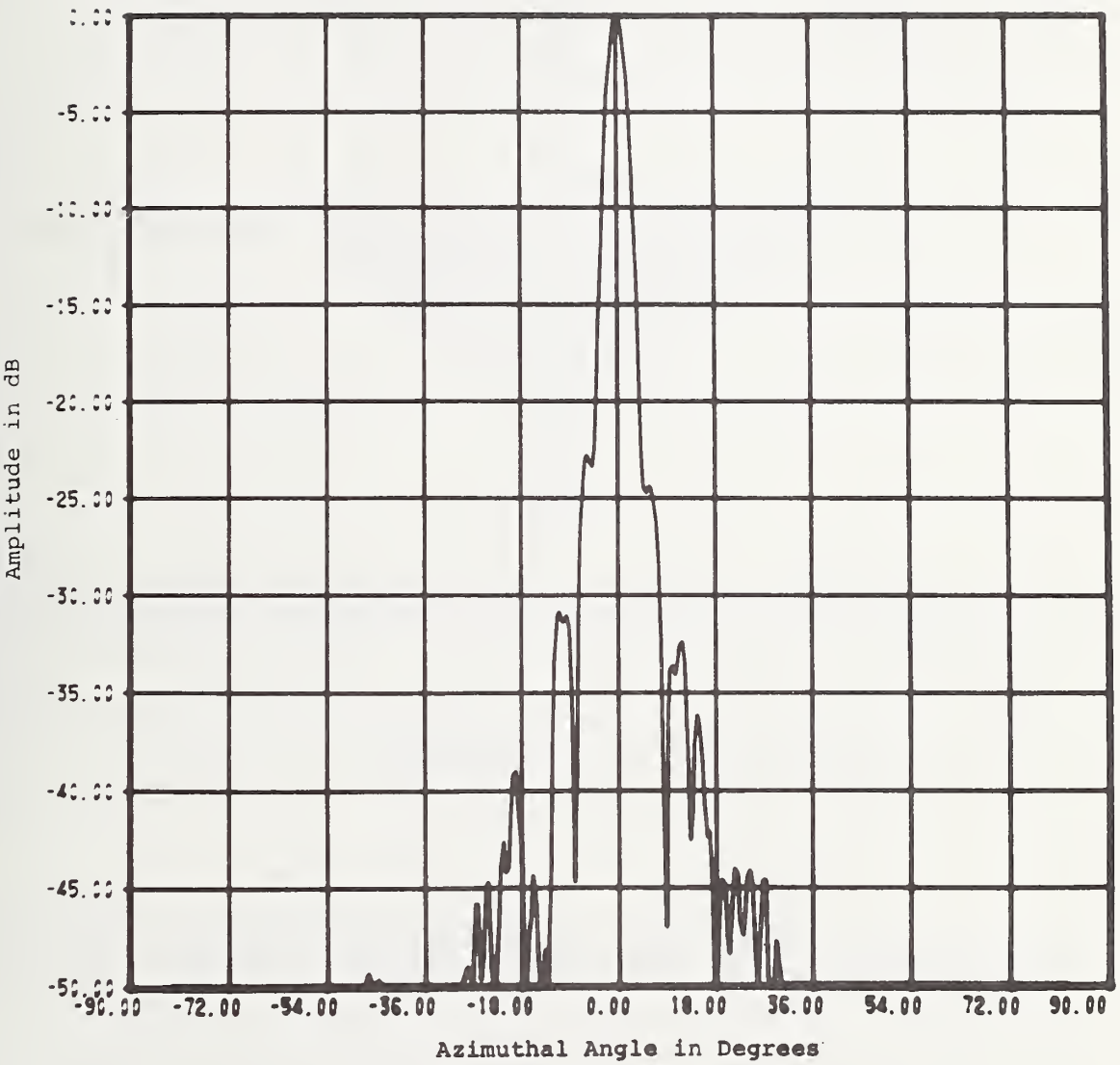

Figure 17. Approximate Far-Field Pattern Computed from Center-line Data Taken on Constrained Lens Antenna, z = 254 cm, Az = EL = 0°.

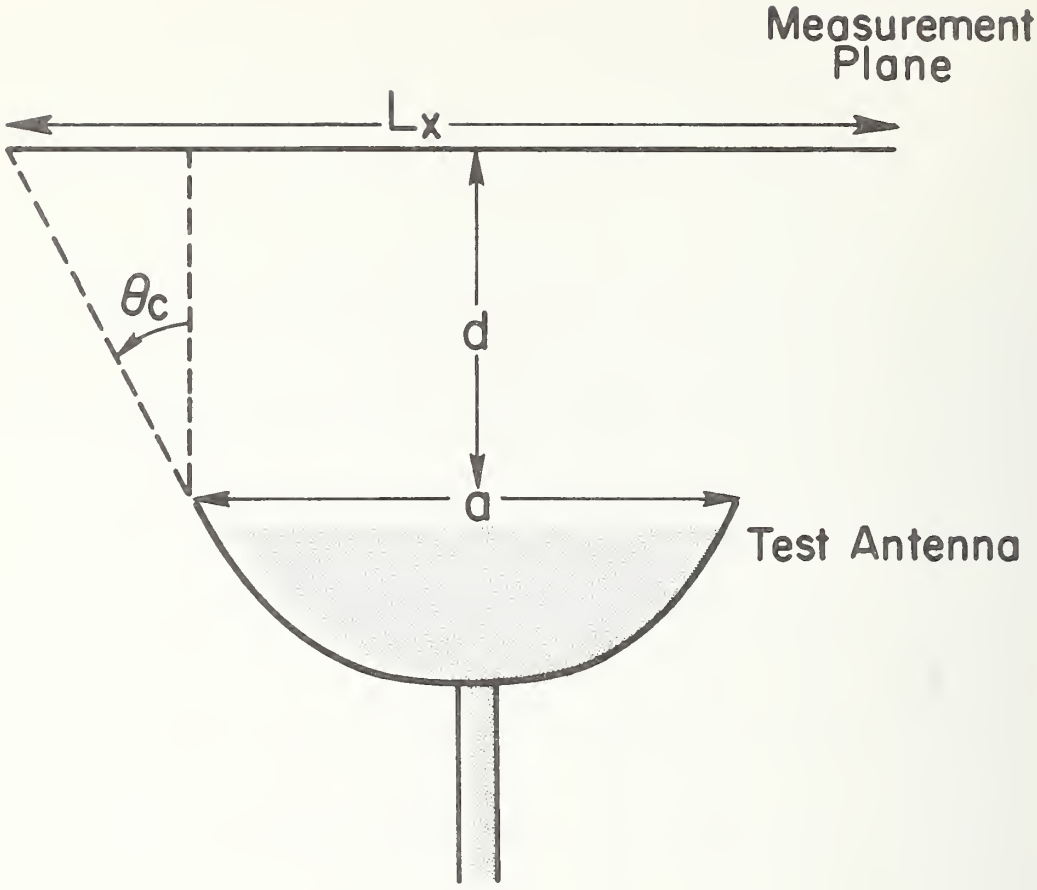

Maximum Angle for Accurate Far Field = θ_c

$$\theta_c \simeq \mathrm{Tan}^{-1}\left(\frac{L_x - a}{2d}\right)$$

TRUNCATION OF MEASUREMENT AREA

Figure 18. Schematic Relationship between Scan Length and Maximum Angle to which Far-Field Pattern can be Accurately Determined.

There are times when this filtering effect, due to increasing the separation distance, will cause errors in an important angular region. The area must therefore be increased, or the separation distance decreased. There are times however when it has a beneficial effect. When high accuracy is required over a limited angular region, the spatial filtering reduces the complexity of the near-field and fewer data points are required. More will be said about this in the following section.

3.2.2 Data Point Spacing Determination

The choice of an adequate spacing of data points is obtained by use of a two-dimensional form of the sampling theorem. This theorem states that if $b_0'(\underline{P})$ is the Fourier transform of a band limited function of $\underline{K}$ with band limits

$$k_1 = \frac{\pi}{\delta_x} \text{ and } k_2 = \frac{\pi}{\delta_y}, \tag{28}$$

then the required spacings are δ_x and δ_y. Furthermore, the integrals in eqs. (19) and (21) may be replaced by a summation, without approximation. The problem is then to determine the band limit of the transform of $b_0'(\underline{P})$. The transform whose band limit we seek is the quantity within the brackets of eq. (17) given by

$$D'(\underline{K})e^{i\gamma d} = \underline{R}_{01}'(\underline{K}) \cdot \underline{S}_{10}(\underline{K})e^{i\gamma d}. \tag{29}$$

In the strictest sense, band limiting would require eq. (29) to be zero for $|\underline{K}|$ greater than some value K_b. Although it may not be zero, an arbitrarily small value of eq. (29) may be attained by choosing the band limit in the evanescent mode region where $|\underline{K}| > k$. In this region, γ is purely imaginary,

and the attenuation due to the $e^{i\gamma d}$ factor insures cutoff for $|\underline{K}|$ only slightly greater than k. This was pointed out originally by Kerns [2], and later discussed in more detail by Joy and Paris [5].

The high degree of cutoff is illustrated by the data for one of the test antennas. Figure 19 is a plot of the relative magnitude of $D'(k_x,0)$ plotted as a function of k_x/k. This was computed from the near-field data shown in figure 11 where $d \simeq 8\lambda$ and $\delta_x = 0.10\lambda$. The region where k_x/k is greater than unity represents evanescent modes which are all at least 50 dB below the main beam. If we choose a band limit of $k_1 = 1.05\ k$ which corresponds to a data point spacing of 0.476λ, an additional attenuation of 140 dB results from the factor $e^{i\gamma d}$. It is clear that the band limit need be only slightly greater than k, and therefore that the minimum required spacing for this antenna at this distance is only slightly less than $\lambda/2$.

The factor of $e^{i\gamma d}$ is not the only term which can produce a band limit however. Band limiting can also occur in the region where γ is real. If either $\underline{R}'_{01}(\underline{K})$ or $\underline{S}_{10}(\underline{K})$ or their product is small enough for all $\underline{K}$ greater than some value, this will produce a practical cutoff. The question as to how small they must be, or equivalently how large δ_x and δ_y may be, is answered in terms of the effect produced on the important part of the far-field for a given cutoff level or data point spacing. To answer this question, the centerline data are again used in a test similar to the one described in the last section. The original data were taken at a closely spaced interval, $\delta_x \simeq \lambda/10$. The spectrum $D'(k_x,0)$ is computed from this closely spaced data and stored in the computer. The spectrum is then computed using only every other data point and the results compared with the stored values. This is repeated for increased intervals and the change in the spectrum

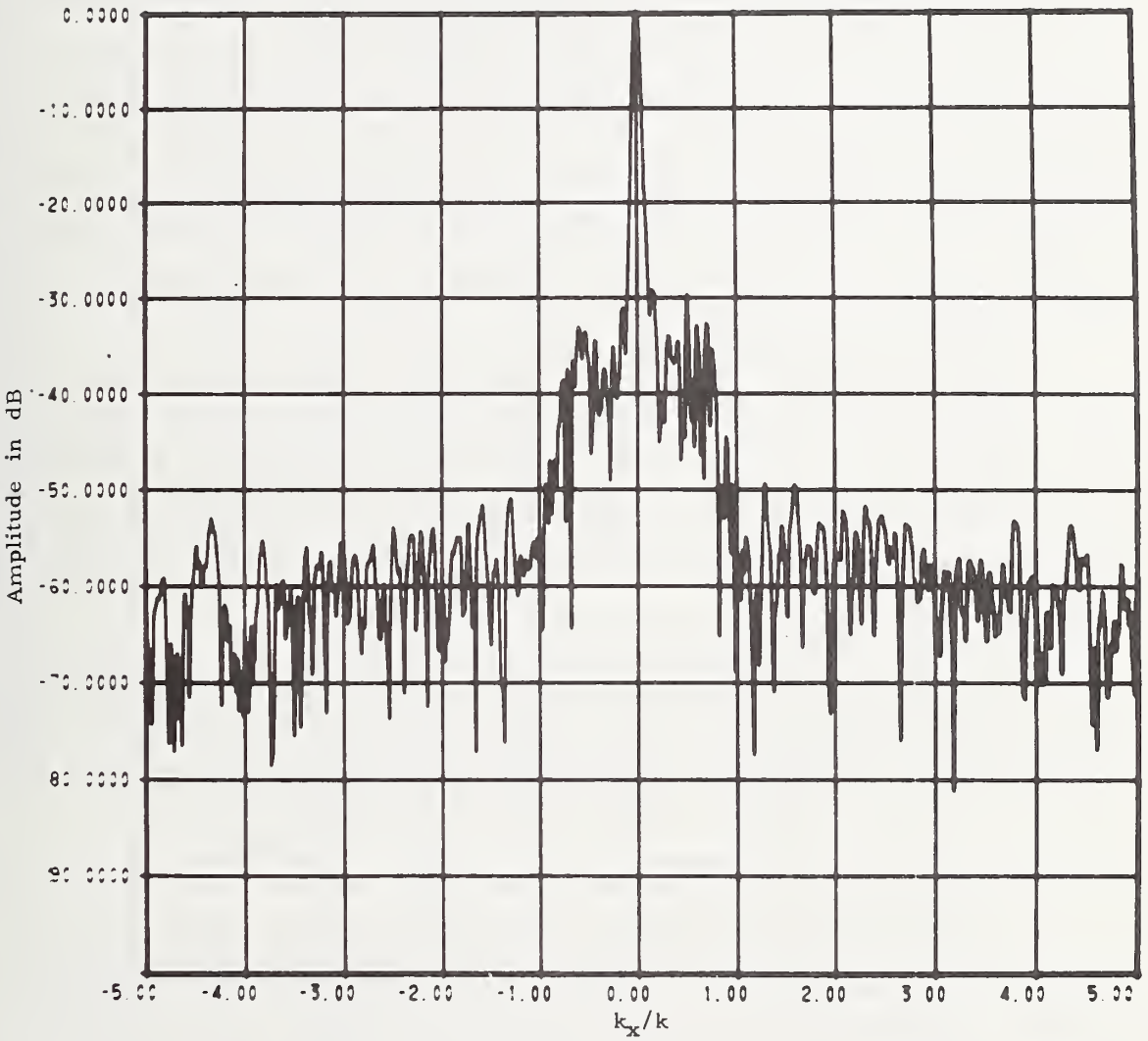

Figure 19. Amplitude Spectrum for Both Propagating and Evanescent Modes on Constrained Lens Antenna.

is measured by computing the RMS and peak difference in the pattern over all real angles and the change in the on-axis gain. These quantities are shown plotted in figure 20 for the centerline data in figure 11. A comparison of patterns for cases where the RMS and peak differences are less than 1% shows that the major changes are at nulls. The positions of nulls and sidelobes are not changed, and the maximum change in sidelobe magnitude is less than 2 dB as shown in figure 21. If this is an acceptable level of accuracy, then for this antenna pair, a spacing of about 0.8 λ can be used. This results in a reduction of over 60% in the number of points required when compared to $\lambda/2$ spacing. This is very significant when applied to antennas with aperture dimensions of 100 λ or more.

From tests on a number of antennas whose near-field is well collimated it is apparent that spacings greater than $\lambda/2$ can frequently be used. For narrow beam antennas, a spacing of slightly less than $\lambda/2$ can therefore be considered as a lower limit rather than $\lambda/2$ being an upper bound as previously had been reported [5].

It must be remembered that when a band limit of K_b is used, and measurements are made at the corresponding spacing, no pattern information is available for $|\underline{K}| > K_b$. The maximum angle to which patterns are calculable is given by

$$\theta_{max} = \sin^{-1} \frac{\lambda}{2\delta} . \qquad (30)$$

If information is desired over a limited angular region, then certain things can be done to produce spatial filterings in the measured data, reduce the band limits, and therefore increase δ_x and δ_y. We have already seen how increasing the separation distance accomplishes this, and a similar effect can be achieved by using a probe with a more directive receiving pattern.

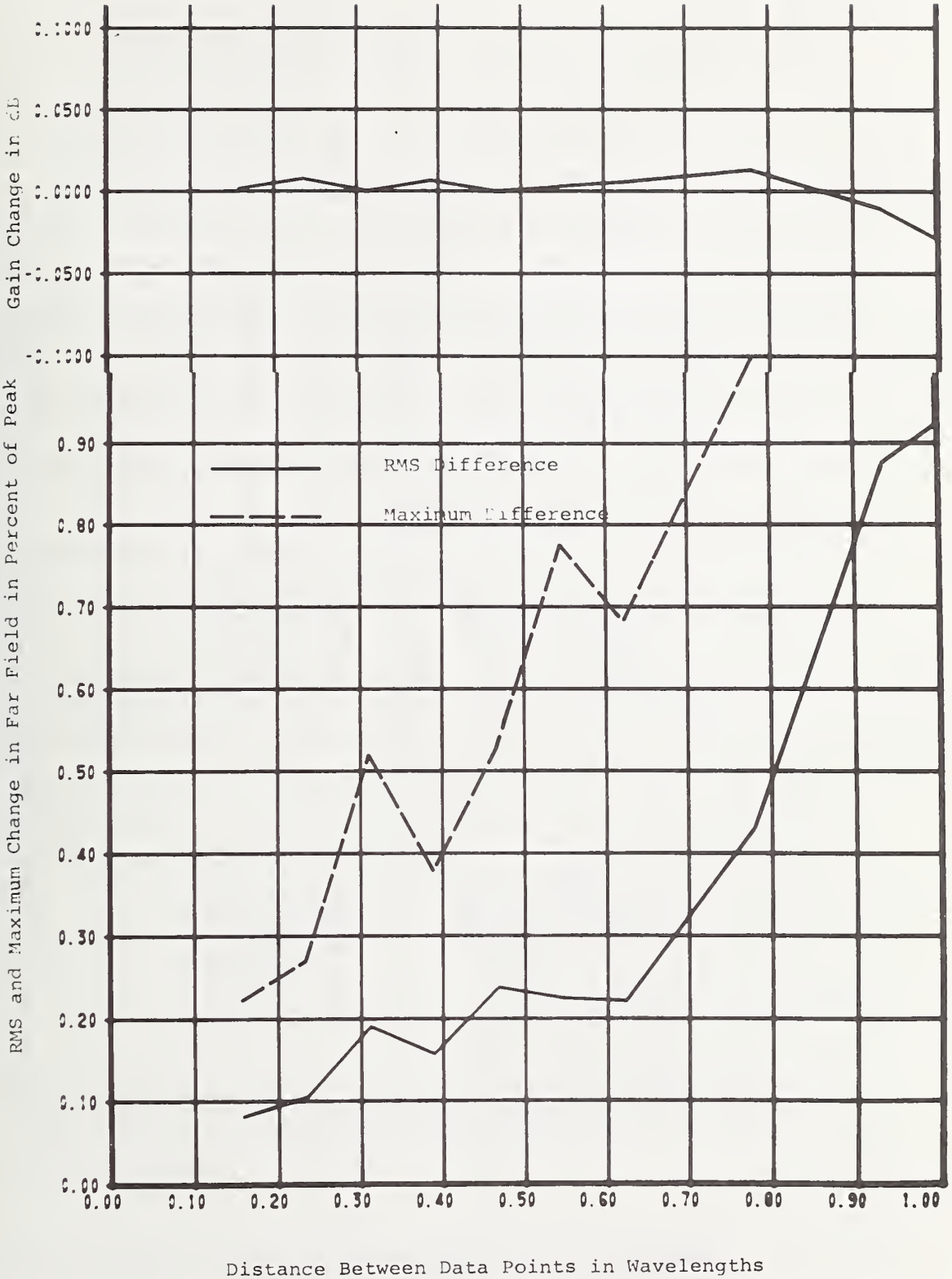

Figure 20. Change in Far-Field Due to Increase of Data Point Spacing.

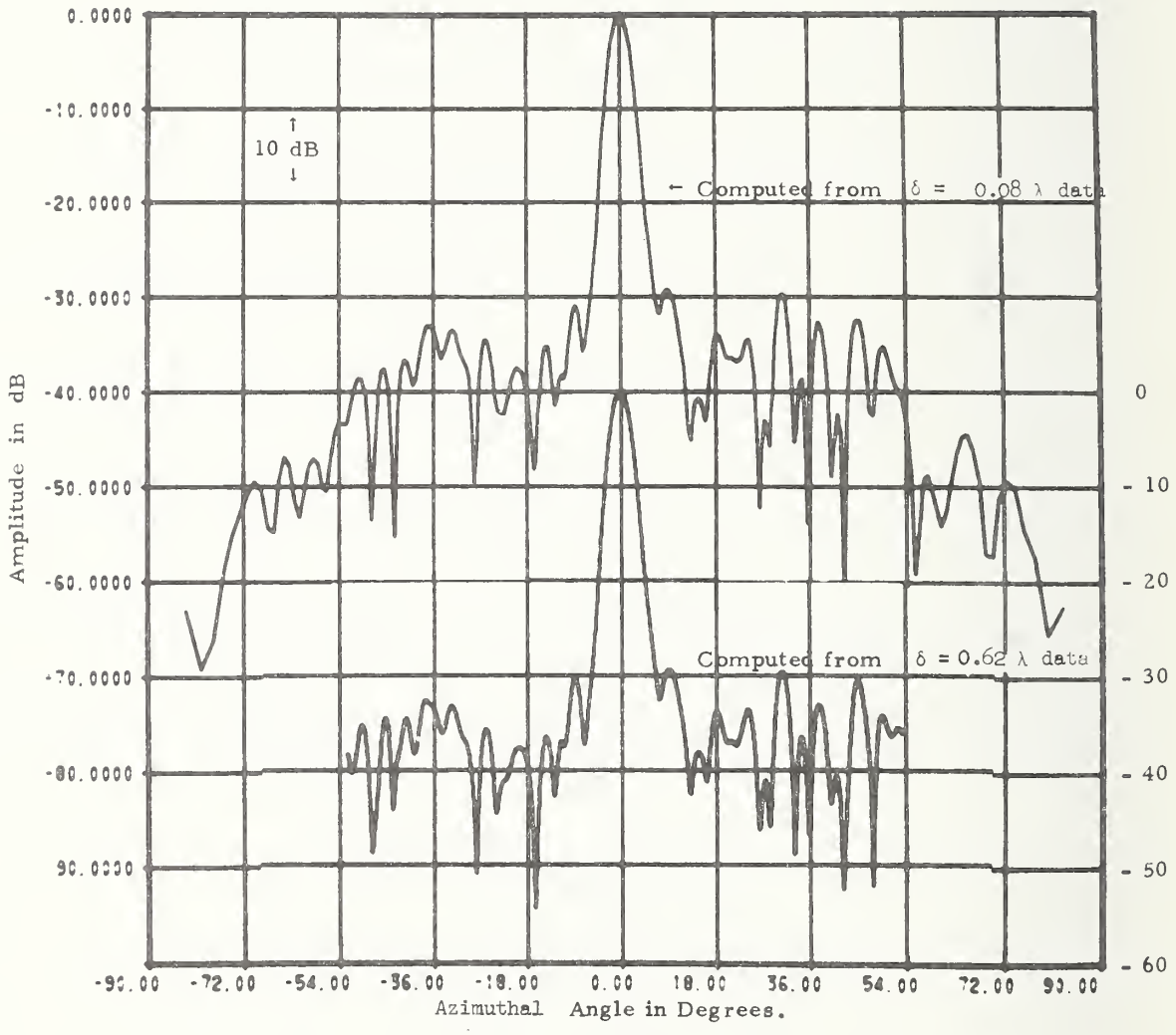

Figure 21. Comparison of Patterns Computed from Near-Field Data with $\delta_x = .08\lambda$ and $\delta_x = 0.62\lambda$, Constrained Lens Antenna.

3.2.3 Scan Area and Data Point Spacing for Main Beam Shifted Away from the Normal to the Measurement Plane

When the planar near-field technique is used on an electronically steerable array, there are times when the main beam is steered to directions other than normal to the measurement plane. Under these conditions, the required scan parameters may change with steering angles, and tests were therefore performed to determine the nature of those changes for scan angles of 45° or less. On the constrained lens antenna, the beam was shifted by mechanically rotating the antenna in its mount, and near-field centerline patterns were measured for azimuth rotations of 0°, 20°, and 38° and elevation rotations of 0°, 10°, and 20°. The data for the 20° azimuth rotation is shown in figure 22 and should be compared to figure 11 which is the comparable data for 0° rotation. The major changes in the data are the translation of the amplitude by the distance, $\Delta x = d \tan \theta$, and the change of the phase in the collimated region from a fairly uniform function to a rapidly increasing function with a slope of $\frac{d\phi}{dx} = \frac{360}{\lambda} \sin 20°$. The scan area which is required for a given angular region about the main beam is approximately the same as for normal incidence, but it has been shifted in space. The maximum scan area for all beam positions can therefore be determined from a knowledge of the maximum scan angles, the angular region about the main beam, and the relationship given in eq. (27). For example, if the beam is to be steered to ± 45°, and patterns computed ± 10° about the main beam, then the scan length must be $L_x = 2d \tan 55° + a$. The distance d between test antenna and the probe must be kept small to maintain a reasonable scan area under these circumstances.

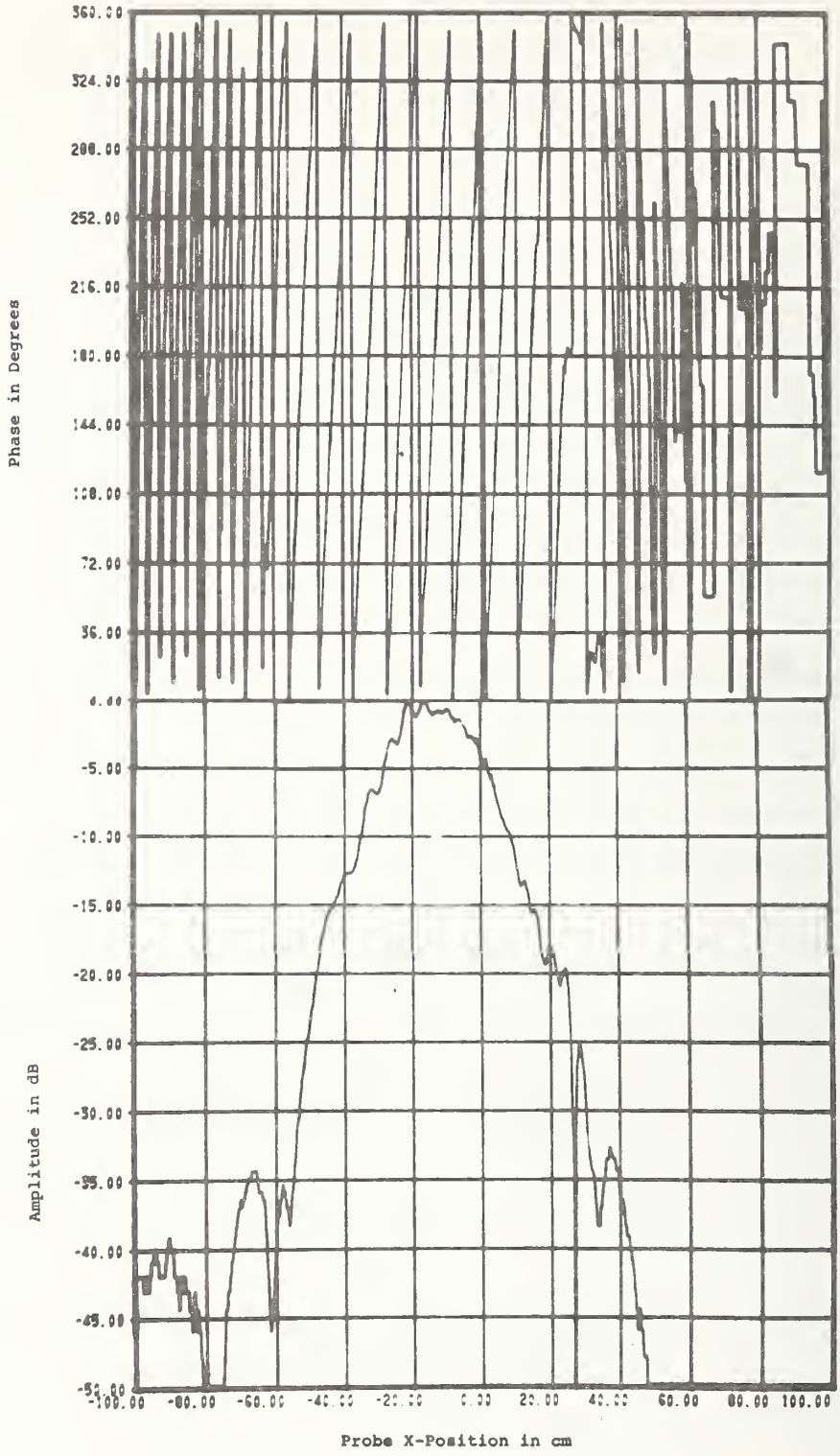

Figure 22. Near-Field Centerline Data, Constrained Lens Antenna, z = 25 cm, Az = 20°, EL = 0°.

The data point spacing is affected by a shift of the beam in two ways. First the main beam and sidelobes are shifted to wider angles, and band limiting in the real angle region will therefore occur at larger angles, which results in a smaller data point spacing. The magnitude of the sidelobes may also increase as the beam is steered, and this will also result in a wider band limit and still smaller data point spacing. Second, there may be an increase in the evanescent modes at the wide steering angles, which would extend the practical cutoff into the imaginary angle region and therefore require a data point spacing of less than $\lambda/2$. This latter effect was not observed for the Volphase antenna for steering angles of 45° or less. The tests on centerline data for various steering angles did show a slight decrease in required spacing for off axis angles, but as figure 23 shows, they were all close to $\lambda/2$.

3.2.4 Effect of Multiple Reflections

It was previously mentioned that multiple reflections between the antennas are assumed to be small enough to neglect. Since this is an approximation, it must be determined how low the reflections actually are, and what their effect is on the computed parameters.

To accomplish this, centerline data were employed in a slightly different way. A series of scans which differed in the z-separation by intervals of $\lambda/4$ were taken along a centerline, and the far-fields were computed for each scan and compared with each other. The multipath signals will have different phase relations at each z-position, and some of the changes in the computed far-fields will be due to the multiple reflections. If the near-field is not a product pattern, some

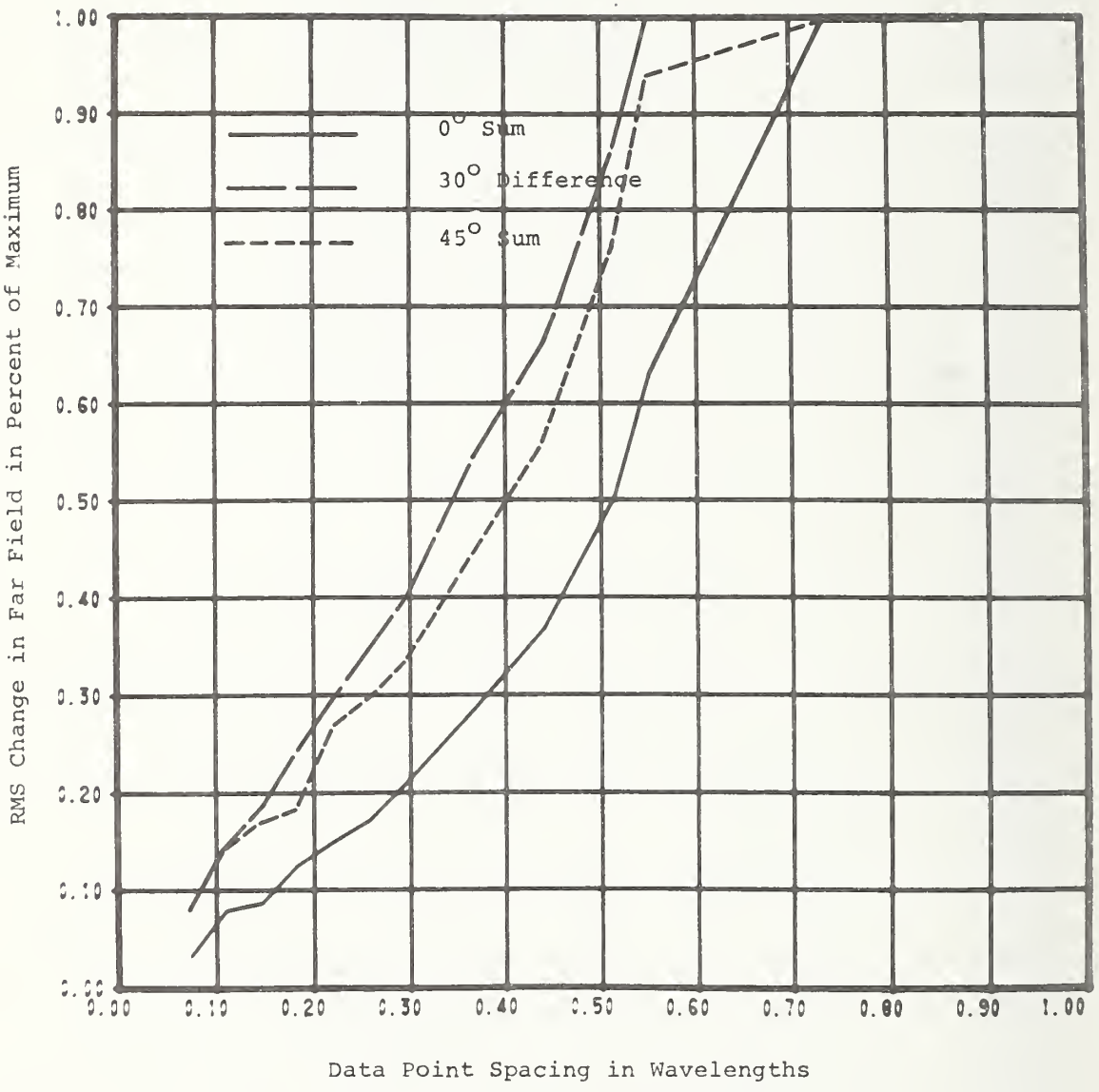

Figure 23. Change in Computed Far-Field Due to Increased Data Point Spacing. Volphase Antenna, z = 38 cm. Az = 0°, 30°, 45°, EL = 0°.

change will occur in the patterns computed from centerline data at different z-distances even if there is no multipath interference. This will probably make the apparent effect of multipath larger than it actually is, and the tests therefore set a probable upper bound to the error.

A typical set of data is illustrated in figure 24. Two scans at z distances which differ by $\lambda/4$ are plotted. These particular data are for the Volphase antenna operating in the sum mode with the beam steered to zero degrees in both azimuth and elevation. Measurements at one distance are shown as continuous curves, and at the second distance as individual points. The far-fields computed from these two sets of data are shown in figure 25, with similar plotting of the two results. It is apparent that the multiple reflections will not cause any serious error in the far-field parameters for this antenna and probe pair.

The magnitude of the multipath can also be estimated by measuring the amplitude of the near-field as a function of separation distance at various points near the center of the collimated region. Periodic variations with a period of $\lambda/2$ are due to multiple reflections, and the magnitude of the interference signal can be determined from the peak-to-peak amplitude of the variations by the expressions,

$$A_m = 20 \log \left(\frac{\rho-1}{\rho+1}\right), \quad \rho = \log^{-1}(M/20), \tag{31}$$

where M is the measured variation in dB, and A_m is the ratio of the true field to the multipath interference signal. Typical measurements of M between 0.1 to 0.2 dB indicate interference levels of approximately 40 dB below the true signal. If the relative phase between the true and interference field did not change over the area of the collimated region, the multipath would increase or decrease all measured amplitudes

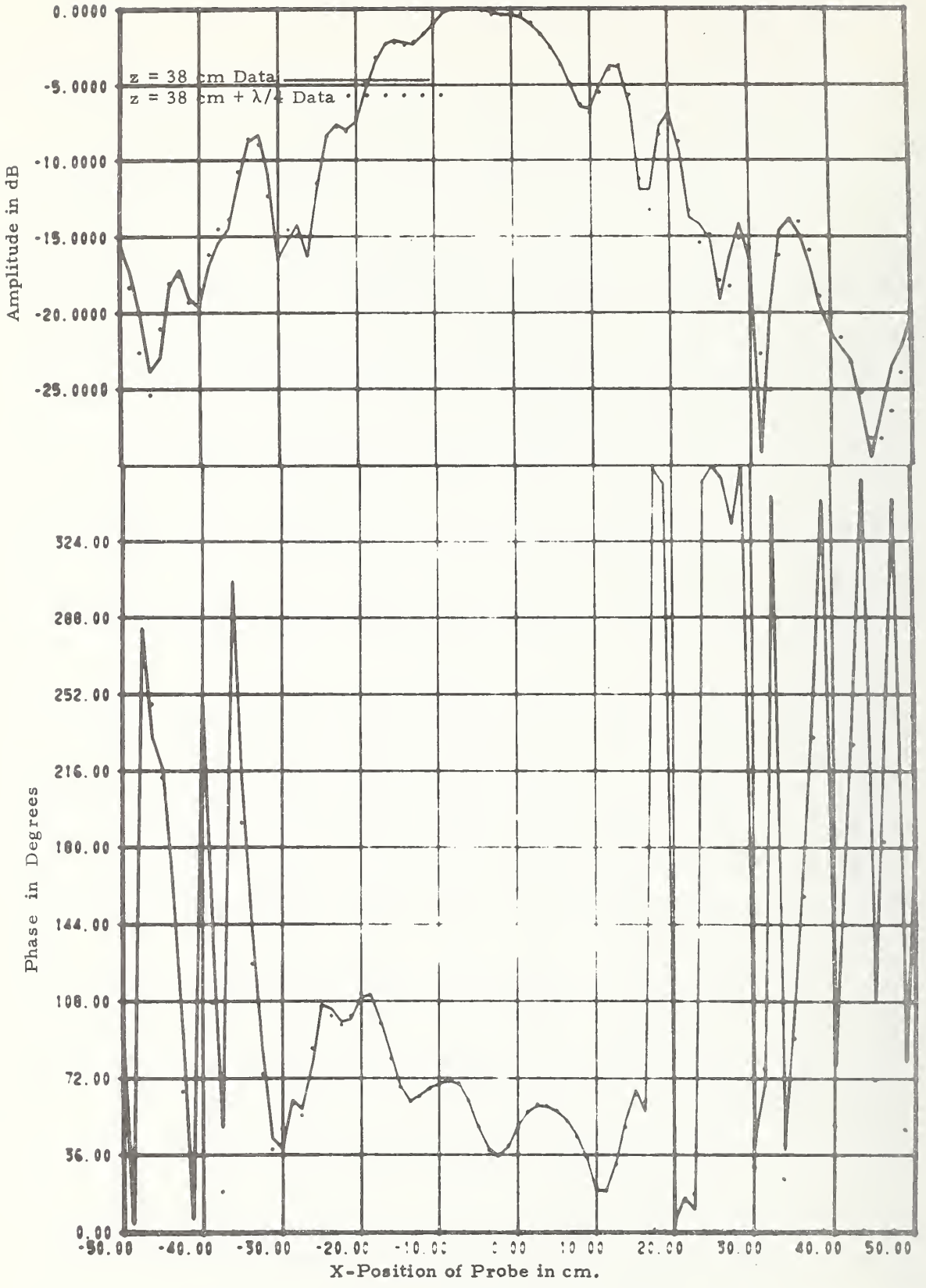

Figure 24. Multipath Centerline Data for Volphase Antenna, z = 38 cm.

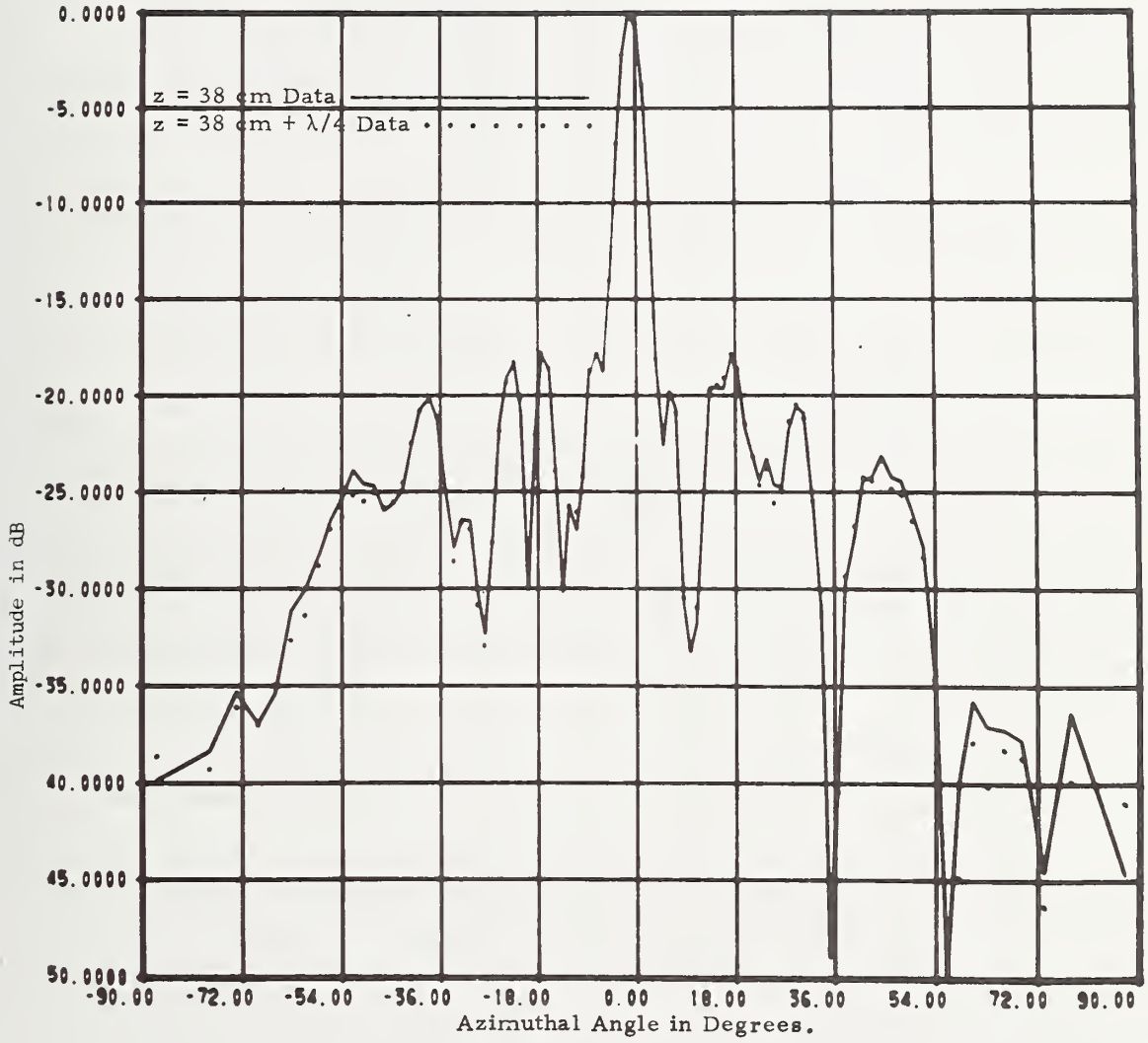

Figure 25. Far-Fields Computed from Data at z-Distance which Differ by λ/4, Volphase Antenna.

by a constant amount. The maximum error in the on-axis gain would therefore be ± M/2 dB, and since all of the pattern would be changed by the same amount, there would be no error in the relative pattern.

The more typical situation is where the multipath goes in and out of phase with the true field across the collimated area, which results in a small periodic variation in the amplitude and phase as a function of x and y. This reduces the error in the on-axis gain, but causes some error in the relative far-field pattern.

In some cases, the multiple reflections may be too large to neglect for a given probe and z-separation. They can be reduced by reducing the size of the probe or increasing the distance between the antennas. Since the mounting structures, the floor and walls, and the scanner do in fact contribute to the scattering characteristics of the total system, the reflections can also be reduced by the appropriate placement of microwave absorbers. For antennas with well collimated beams, and fairly small z-distances, a large amount of absorbing material is not required. It is generally not necessary that the room be completely covered with absorbing material.

3.2.5 Detection of Faulty Array Elements and Radome

One very useful side benefit of the near-field scanning techniques is the possibility of detecting and identifying faults associated with the test antenna. Ideally one would like to differentiate between array faults and radome faults and locate the position of faulty elements and/or radome anomalies. To investigate possible means of using the near-field data to accomplish this fault detection/location, numerous scans were taken with and without real or simulated faults. The general approach was to record a set of data with

the array and/or radome operating properly, introduce a real or simulated fault, and record data at the same positions as the first case. The raw data were compared, or the data after identical processing were compared, to evaluate the sensitivity to various faults. Most of the data involving fault location are still to be processed and only preliminary results are available at this time.

Some of the data which have been processed involves simulated phase shifter faults on the constrained lens antenna. Aluminum oxide disks were cut to fit over a single radiating element. Various thicknesses were used to produce phase shifts of 45°, 90°, and 180°. Figure 26 shows the superimposed plots of the amplitude and phase along the near-field centerline y=0, z=25 cm with and without a 180° dielectric disk at x=0, y=0. The effect of the simulated fault is more clearly seen in figure 27 where the changes in amplitude and phase due to the simulated fault are plotted. Figure 28 is a similar difference plot for the case when the dielectric disk had been moved to the position x=25, y=0. In both cases, the changes in phase and amplitude are a good indication of the general locations of the faulty element. Further data processing is being done on this and similar two-dimensional data to try to improve the indication and location of faulty array elements.

3.2.6 Far-Field Patterns from Centerline Data

In the previous sections, the centerline data have been used to determine scan parameters and estimate errors. The far-field patterns and gains derived from the one dimensional scans have not been examined in detail. Only their changes due to changes in the amount or character of the data have been examined. It is also of interest to determine the accuracy of the far-field parameters which have been determined from centerline data and therefore to discuss the possibility of using centerline scans in other types of tests.

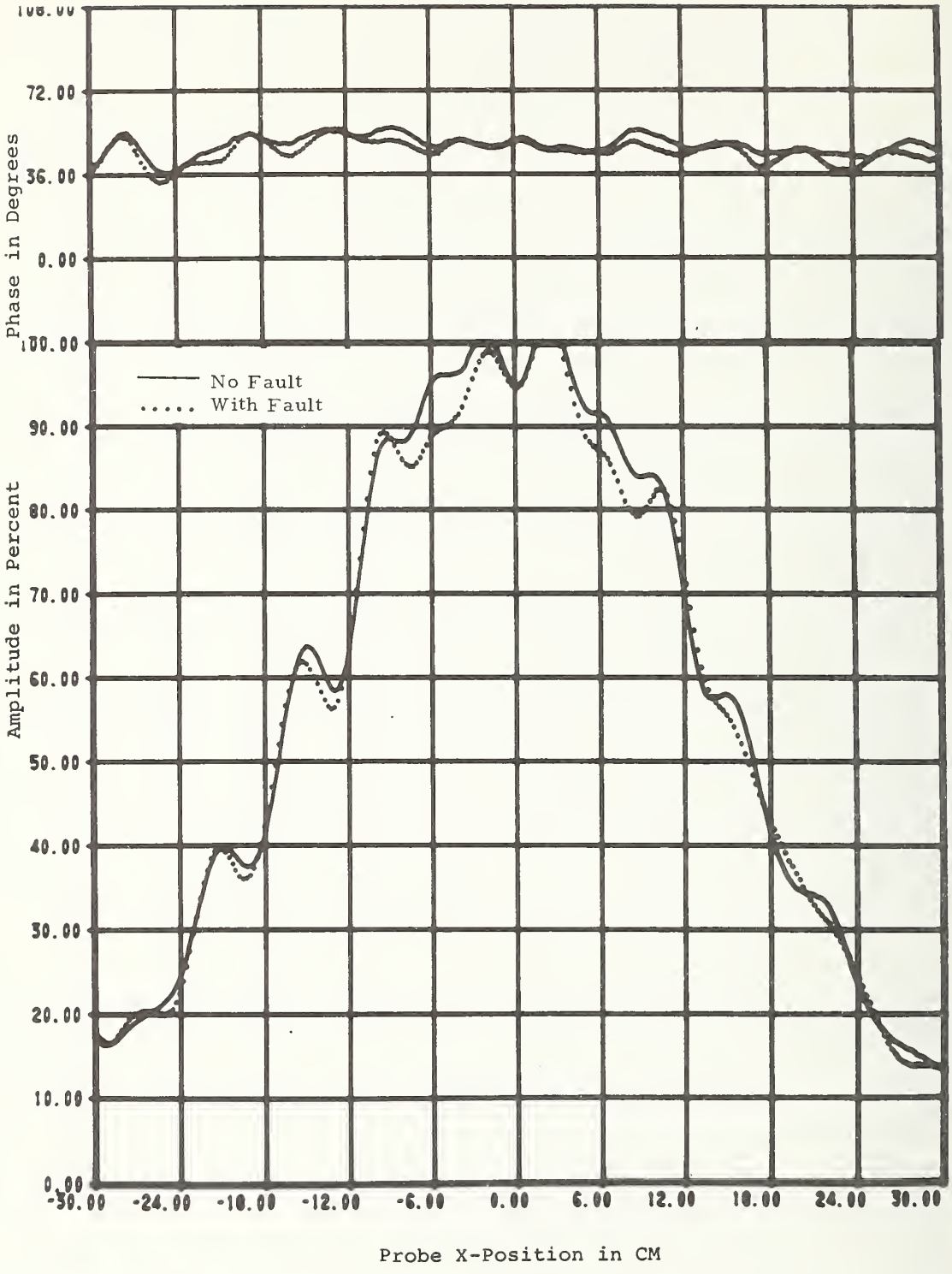

Figure 26. Near-Field Amplitude and Phase Centerline Data on Constrained Lens Antenna With and Without 180° Simulated Phase Shifter Fault at x = 0.

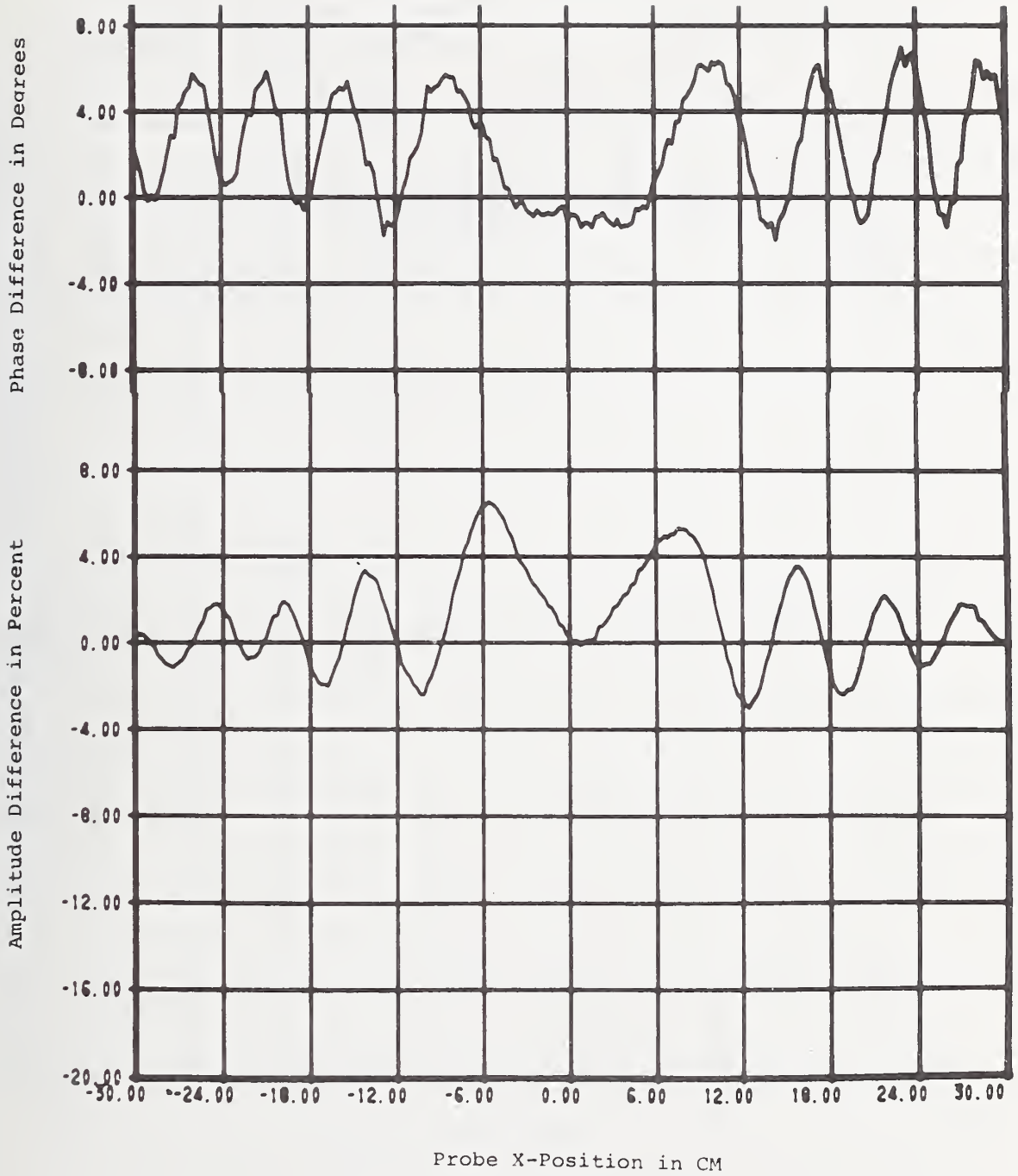

Figure 27. Change in Amplitude and Phase Due to 180° Simulated Fault at x = 0.

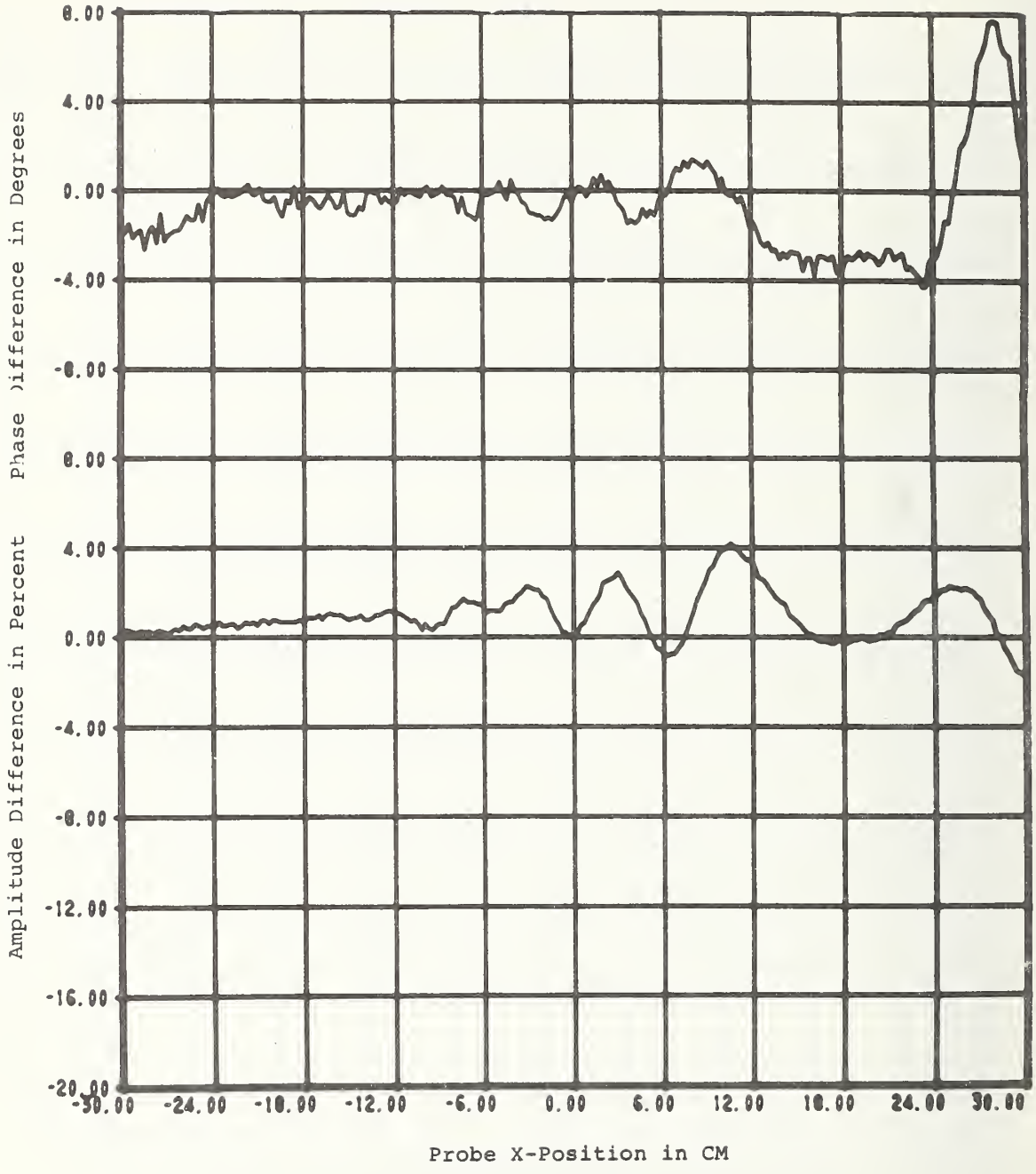

Figure 28. Change in Amplitude and Phase Due to 180° Simulated Fault at x = 18 cm.

The validity of using this approach rests upon the assumption that the measured complete data are expressible as a rectangular product function. That is that

$$b_0'(x,y) = b_0'(0,y)\ b_0'(x,0).$$

If this is true for a given antenna, then the centerline data will give accurate results. If it is not true, then the results will only be an approximation to the actual far-field parameters. The design and construction of the antennas usually will give some indication as to whether or not the rectangular separability will be a good approximation. Because of the circular aperture on the constrained lens, the centerline data would not be expected to give very accurate results. Figures 29 and 30 show the comparison between far-field patterns for the constrained lens antenna which were computed from complete two-dimensional data and only centerline scans. As expected, there is qualitative agreement but a significant difference in the detail of the sidelobes.

For the Volphase antenna with a rectangular aperture and a design which fits the rectangular separability assumption, the centerline data should give much better results. This is verified by reference to figures 31-34, which also compare results from complete and centerline data for this antenna for both sum and azimuth difference modes.

Certainly for an antenna like the Volphase, and even to some degree for the constrained lens type, the results of one-dimensional scans would be helpful during the initial construction and testing of an antenna. The approximate results could be computed quickly and used in the adjustment of feeds, phase shifters, or other elements to optimize antenna performance. The final configuration could then be tested using more complete data.

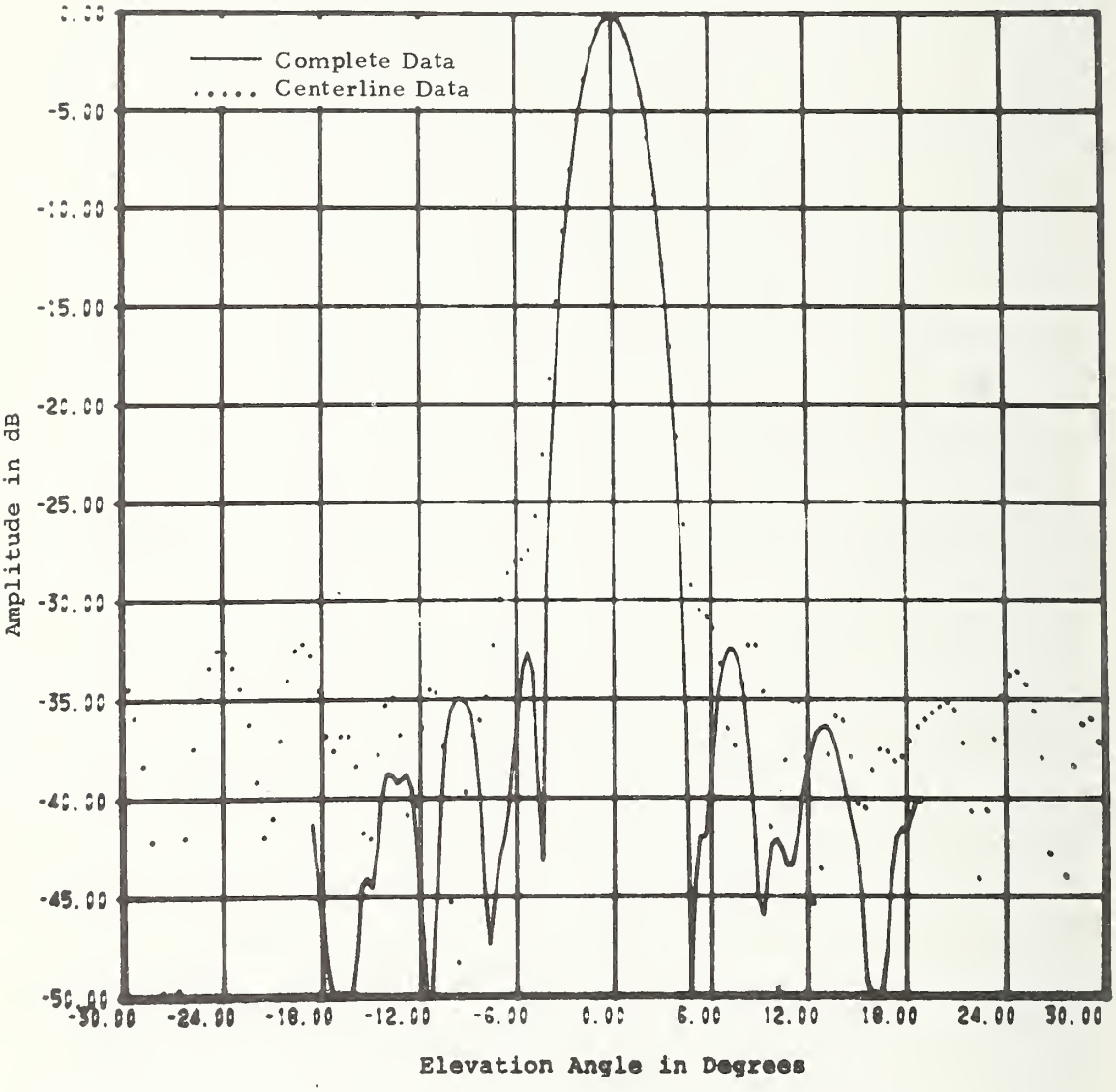

Figure 29. Comparison Between Far-Field Patterns Computed from Complete and Centerline Data. Constrained Lens Antenna, E-Plane Sum Pattern.

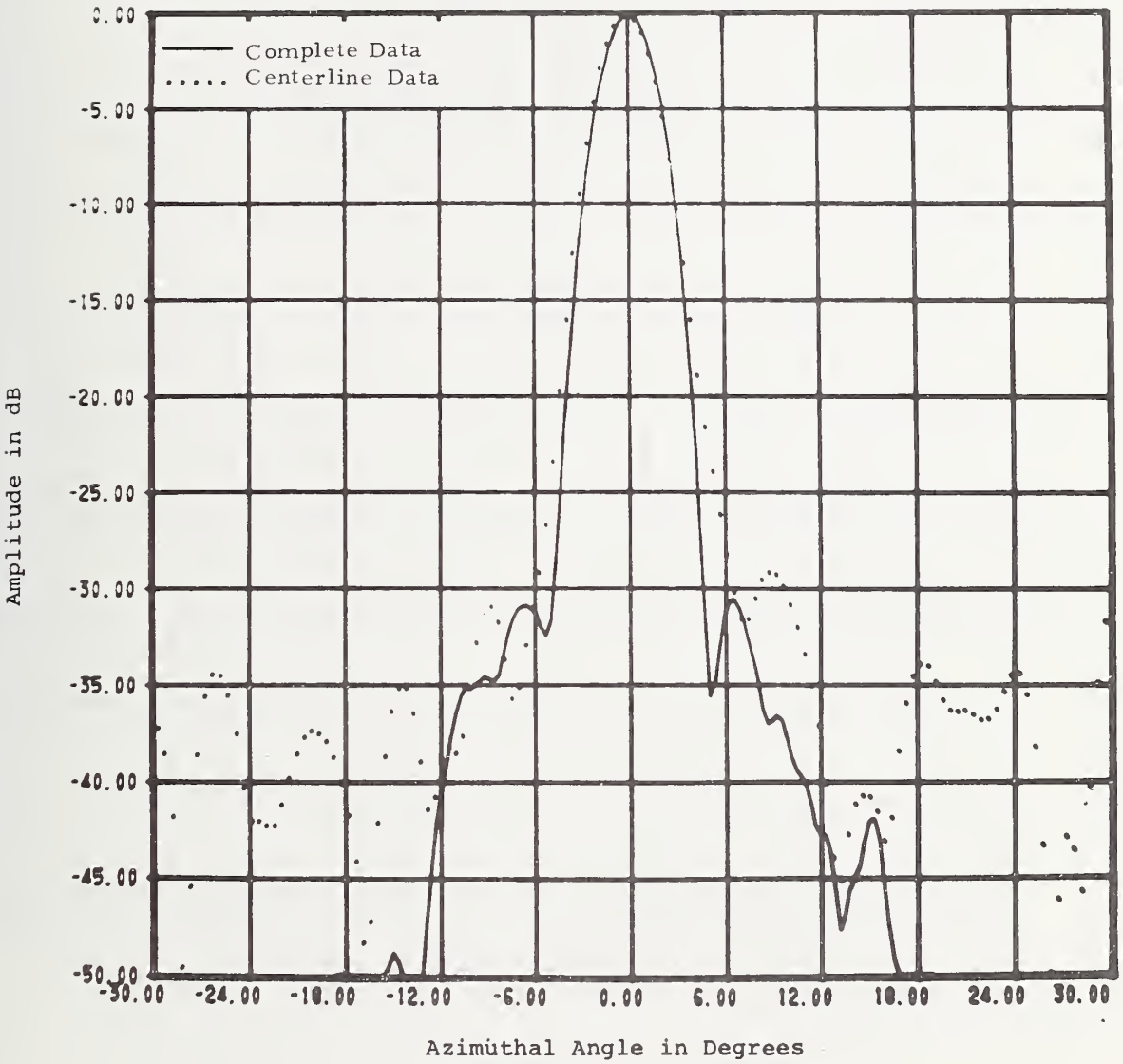

Figure 30. Comparison Between Far-Field Patterns Computed from Complete and Centerline Data. Constrained Lens Antenna, H-Plane Sum Pattern.

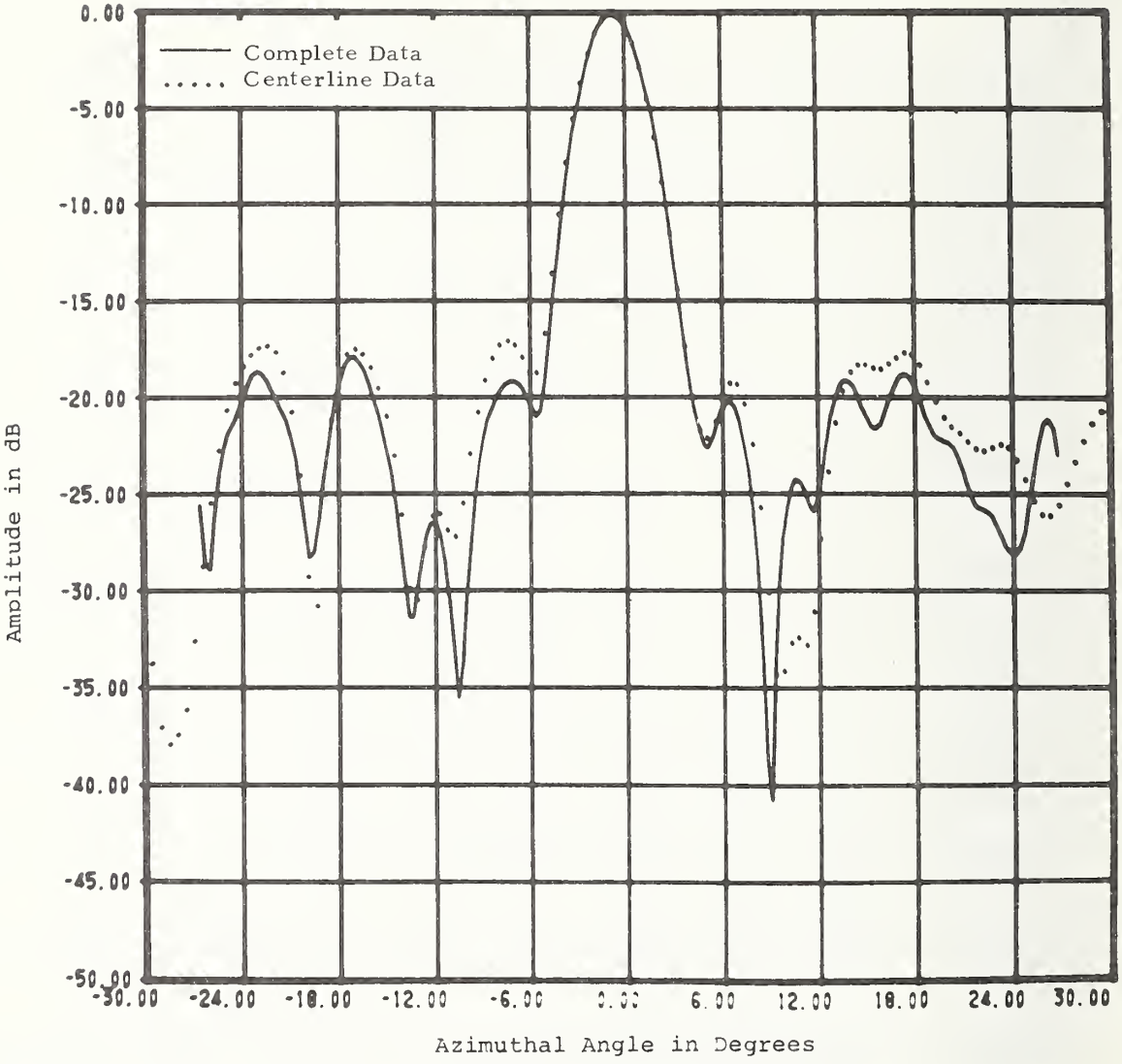

Figure 31. Comparison Between Far-Field Patterns Computed from Complete and Centerline Data. Volphase Antenna, 0° Sum Pattern.

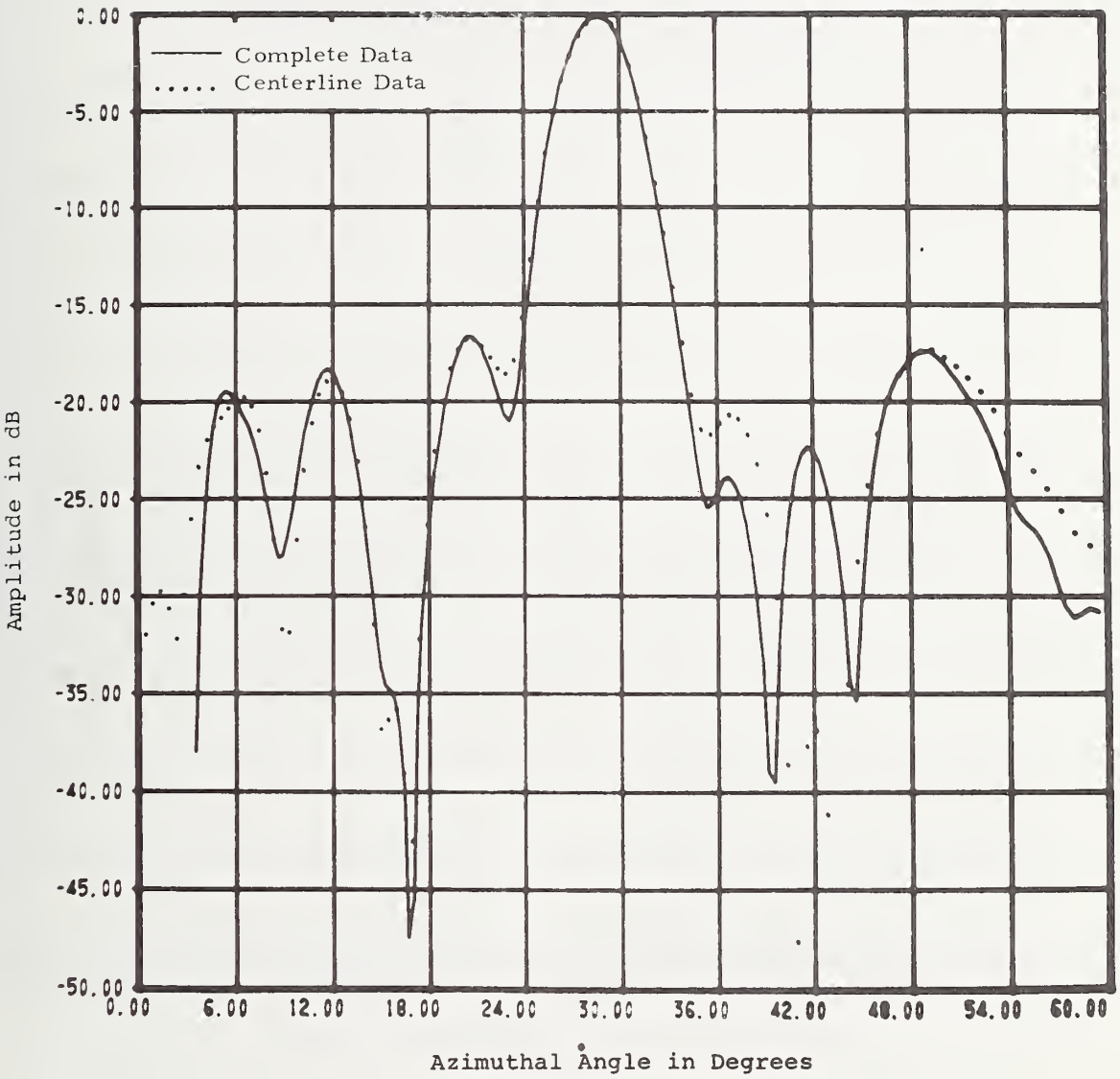

Figure 32. Comparison Between Far-Field Patterns Computed from Complete and Centerline Data. Volphase Antenna, 30° Sum Pattern.

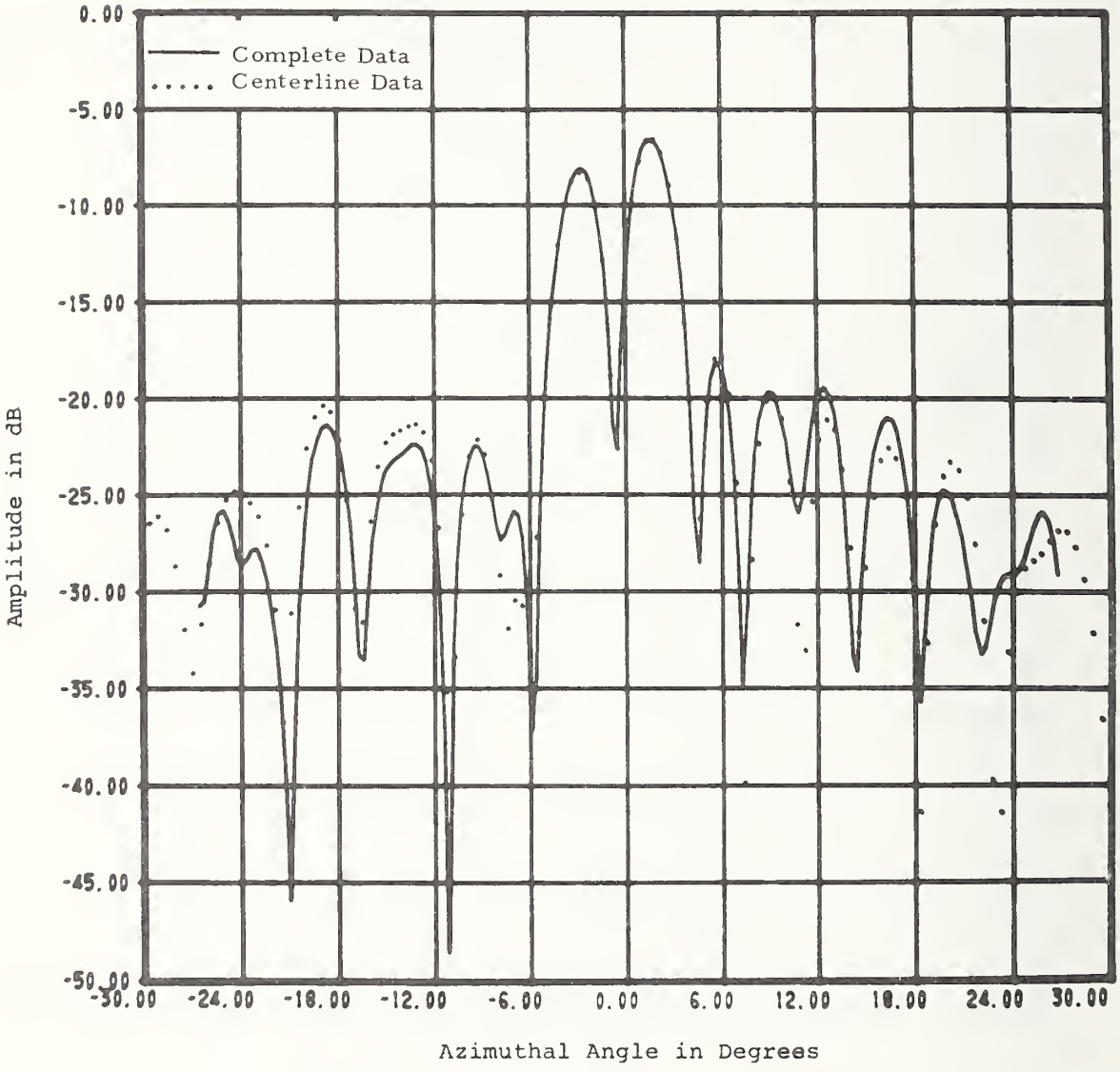

Figure 33. Comparison Between Far-Field Patterns Computed from Complete and Centerline Data. Volphase Antenna, 0° Azimuth Difference Pattern.

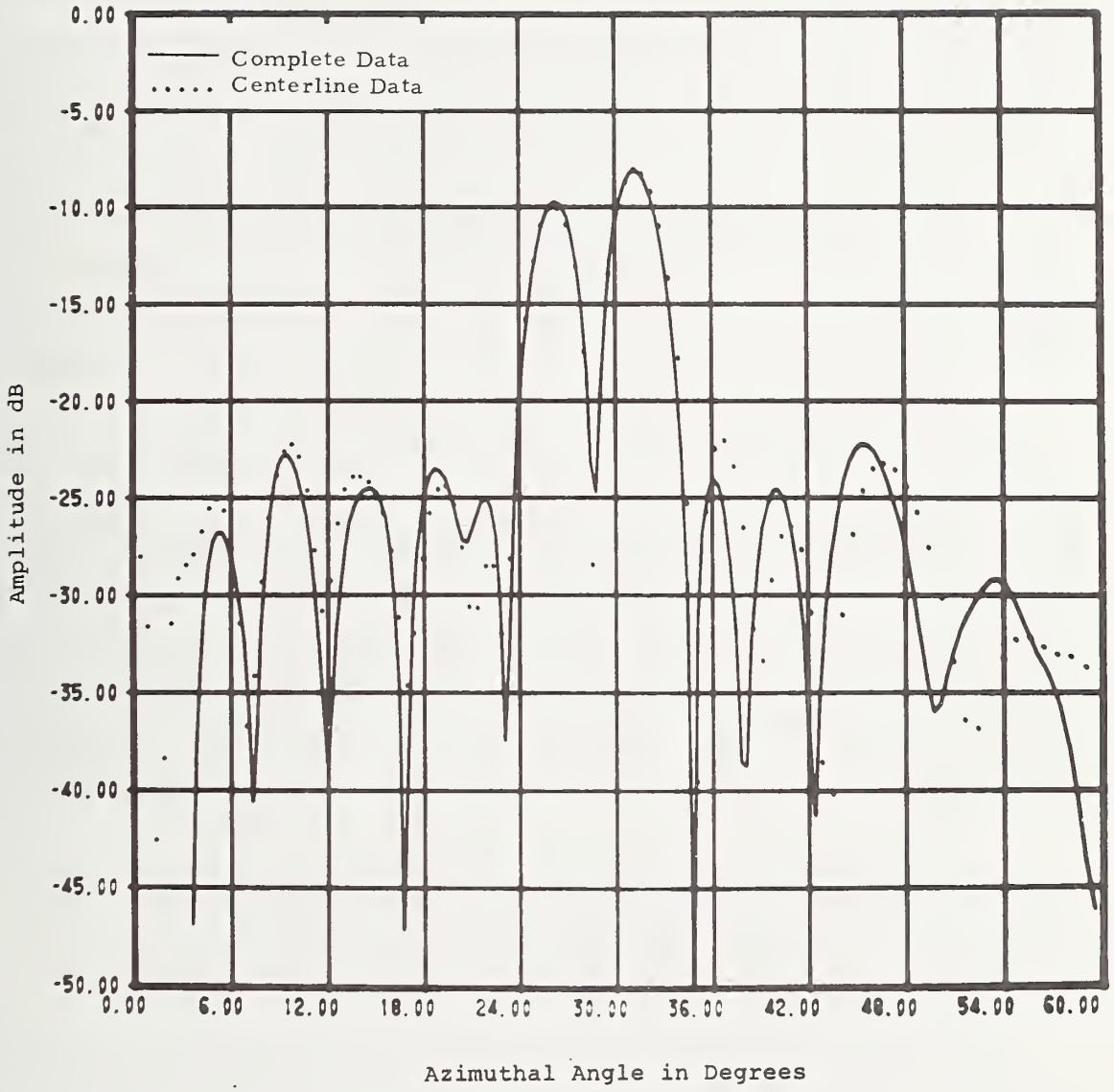

Figure 34. Comparison Between Far-Field Patterns Computed from Complete and Centerline Data. Volphase Antenna, 30° Azimuth Difference Pattern.

3.2.7 Summary of Conclusions from Tests Using Centerline Data

Tests have been described which are very helpful, and in some instances required, to determine the scan parameters and the effects of multiple reflections. Additional tests were also made indicating the feasibility of using this technique to detect antenna element and/or radome faults. Since an assumption of product pattern separability is implicit in these preliminary tests, the results will in general indicate a worst case error due to area truncation, data point spacing increase, and multipath. This is because the effect of the three things being tested will not have the same character along every scan. The variations will tend to have more of a random effect when complete two-dimensional data are used, which reduces the actual error in far-field parameters.

Each given test antenna and test program will have a particular set of desired results. One may require pattern information over a large angular region on a fairly broad beam antenna while another seeks for high accuracy in on-axis gain plus pattern information over a limited angular region. The scan parameters and the type of probe should be chosen to achieve the measurement goals in each situation. The guidelines discussed here and the tests which were described are very helpful in choosing the optimum scan parameters.

It has been shown that for directional antennas, the effects of actual evanescent modes are usually very small, and therefore the minimum required data point spacings are only slightly less than $\lambda/2$.

Spatial filtering can be accomplished by using a directive probe or increasing the distance between the test antenna and probe. This spatial filtering reduces the number of data points required by reducing the scan area and/or increasing the data point spacing. Such filtering will however decrease the angular region over which far-field results are obtainable. The desirability of such filtering will depend on the individual application.

If the antenna design is such that the measured near-field can be approximated by a separable product pattern, the far-field patterns computed from centerline data will be fairly accurate. Centerline data for this type of antenna may be sufficient for many purposes and would be very useful, for instance, during the design and construction of the array. Pattern and gain measurements could be obtained quickly and the effects of modification could be determined.

3.3 Two-Dimensional Measurements and Results

In the present program, complete two-dimensional data have been obtained for the two test antennas under a number of different conditions. The test parameters which have been varied include the use or absence of a radome, z-distance between the probe and test antenna, sum or difference mode, transmitting or receiving from the probe, beam steering direction, and simulation of antenna and radome faults. In total over forty complete near-field scans were recorded (tables 2 and 4), but only part have been completely processed. Those that have been processed will be discussed here to illustrate the measurement technique and demonstrate the results which have been obtained.

3.3.1 Measurements at Different z-Spacings for Sum and Difference Antenna Modes on the Test Antennas

Once the scan parameters are determined, the antennas aligned, and the source and receiver systems checked for stability, a complete scan can be taken. With an automated system, the scan parameters are entered into the position programmer and the measurement from that point on is completely automatic. The probe is moved continuously in the chosen scan

direction (y in our case) and at the preset intervals the position programmer triggers the data system to record the amplitude and phase of the probe output. When the scan length has been covered, the programmer either steps the positioner the prescribed amount in the x-direction or retraces and then steps, and repeats the scan. This process may take from two to eight hours depending on the size of the scan area and the travel speed of the positioner.

Since the relatively long measurement times are required, the receiver system may drift, and some correction for this drift is desirable. The system is very stable during one scan, but the drift between the first and latter scans can be significant. To correct for this, normalization scans are taken at the original measurement points over a small area through the center of the scan area. These normalization scans are taken in the direction perpendicular to the original scans, and used to obtain correction coefficients for all the data in each linear scan. As an additional step in this calculation of the normalization coefficients, the amplitudes and phases of all the data are also normalized with respect to one point in the measurement matrix. The particular point is arbitrary, but it is convenient to choose it close to the center and near the peak amplitude point. If we denote the reference point by $\underline{P}_o$, then the normalized data are given by

$$B_o'(\underline{P}) = \frac{b_o'(\underline{P})}{b_o'(\underline{P}_o)}. \tag{32}$$

To obtain the second complete set of data (which is necessary to solve for the two components of $\underline{S}_{10}(\underline{K})$), the probe is rotated about its z-axis by 90° and the scanning procedure is repeated. For a test antenna and probe which are nearly linearly polarized, the amplitude of this second set of data may be very

small. In some cases it may even be neglected. It must be measured however if spherical components of the far-field are to be determined along non-principal planes or if polarization ratios are desired. The normalization point for these data need not be the same as for the first set. In fact it is usually different, since the cross component is usually smallest in the center where the principal component is largest. If we denote the normalization point for these data by $\underline{P}_1$, then the normalized data are given by

$$B_o''(\underline{P}) = \frac{b_o''(\underline{P})}{b_o''(\underline{P}_1)}. \tag{33}$$

The two sets of data, $B_o'(\underline{P})$ and $B_o''(\underline{P})$, must now be referenced to the input signal, a_o, so that they will have a common phase and amplitude reference. This can be accomplished by first placing the probe at P_o, and orienting it for response to the first measured component. The transmission lines connected to the two antennas are removed and connected directly together. The normalization factor

$$\tau_1 = \frac{b_o'(\underline{P}_o)}{a_o},$$

is then determined from the measured change in the received signal and the appropriate impedance mismatch factors. The second factor,

$$\tau_2 = \frac{b_o''(\underline{P}_1)}{a_o},$$

can be measured in a similar manner, or it can be obtained from τ_1 and a measurement of the ratio $\tau_3 = b_o''(\underline{P}_1)/b_o'(\underline{P}_o)$. If the latter approach is used, only the magnitude of τ_1 is required, but both phase and amplitude of τ_3 are necessary.

For a test antenna which is approximately linearly polarized in the y-direction, and a probe with similar polarization, $B_o'(\underline{P})$ is termed the y- or principal-component data, and $B_o''(\underline{P})$ the x- or cross component-data. These terms are not completely accurate, since the probe will generally respond to both x and y components even if it transmits only a y-component, but they are descriptive and useful.

Figures 35a and 35b are three-dimensional plots of the amplitude and phase of $B_o'(\underline{P})$ resulting from measurements at z = 25 cm on the sum port of the constrained lens antenna. Figures 36a and 36b show the data for the same antenna and probe for a z-spacing of 250 cm. The spatial filtering due to the increased separation distance is very apparent in the smoothness of figure 36a. Figure 36b also illustrates an alternate way of plotting the phase data, where only half of the data are plotted and viewed from a lower observation point. The phase plot in figure 36b shows more detail of the important center section.

The far-field patterns were computed for both of these sets of data, and the result for the data in figure 35 is shown in figure 37. The first step in this computation is the evaluation of the integrals of eqs. (19) and (21) by the Fast Fourier Transform. This routine is extremely efficient, requiring about 30 seconds to transform an array of 128 x 128 complex near-field points to an equal number of far-field values. It is most efficient when the array size is a power of two, and so the data arrays are often padded with zeroes to increase their dimensions to powers of two.

After both sets of data have been transformed, the probe correction is applied to obtain the two rectangular or spherical components of $\underline{s}_{10}(\underline{K})$. This probe correction consists of using the previously measured receiving characteristic of the probe,

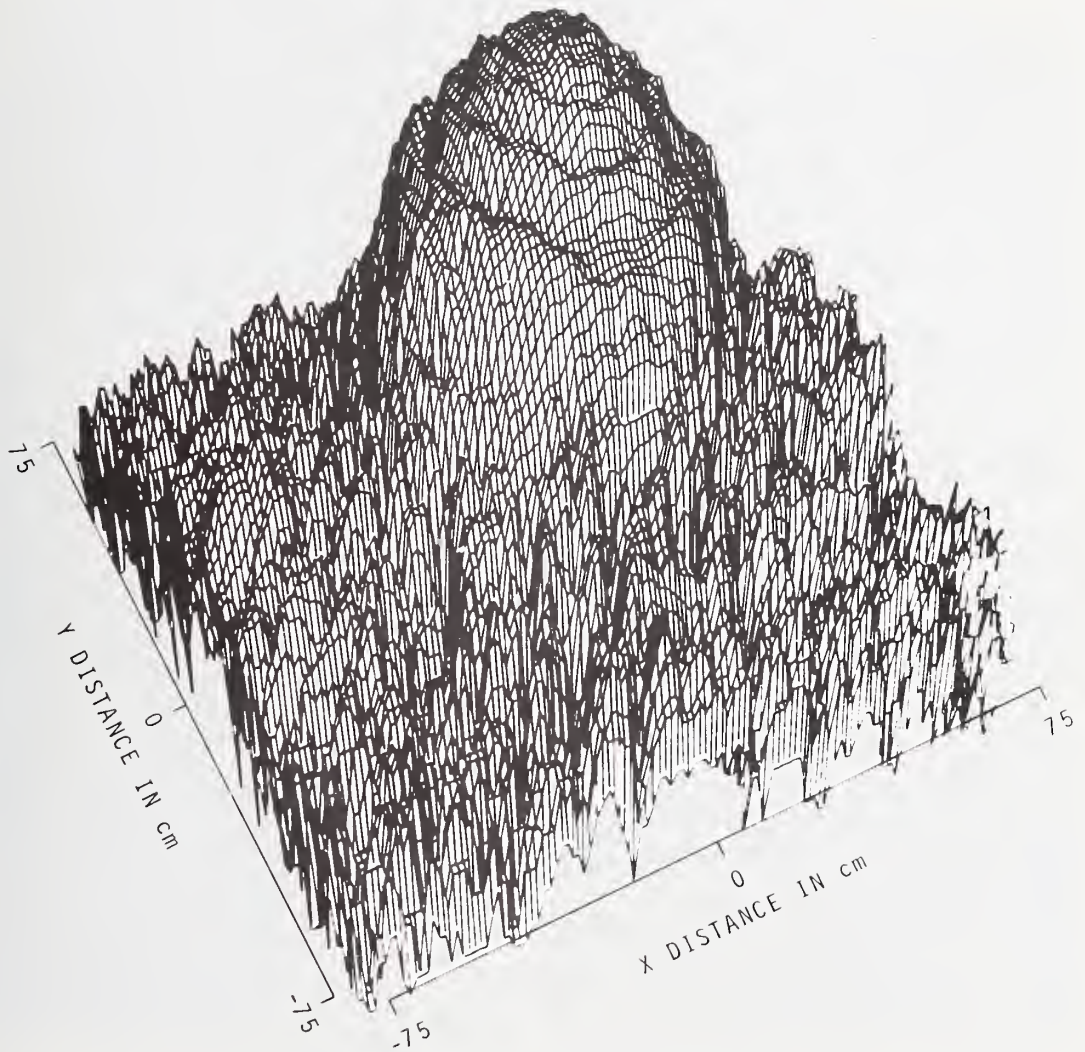

Figure 35a. Constrained Lens Sum Port Near-Field Log Amplitude, f = 9.2 GHz, z = 25.0 cm, No Radome.

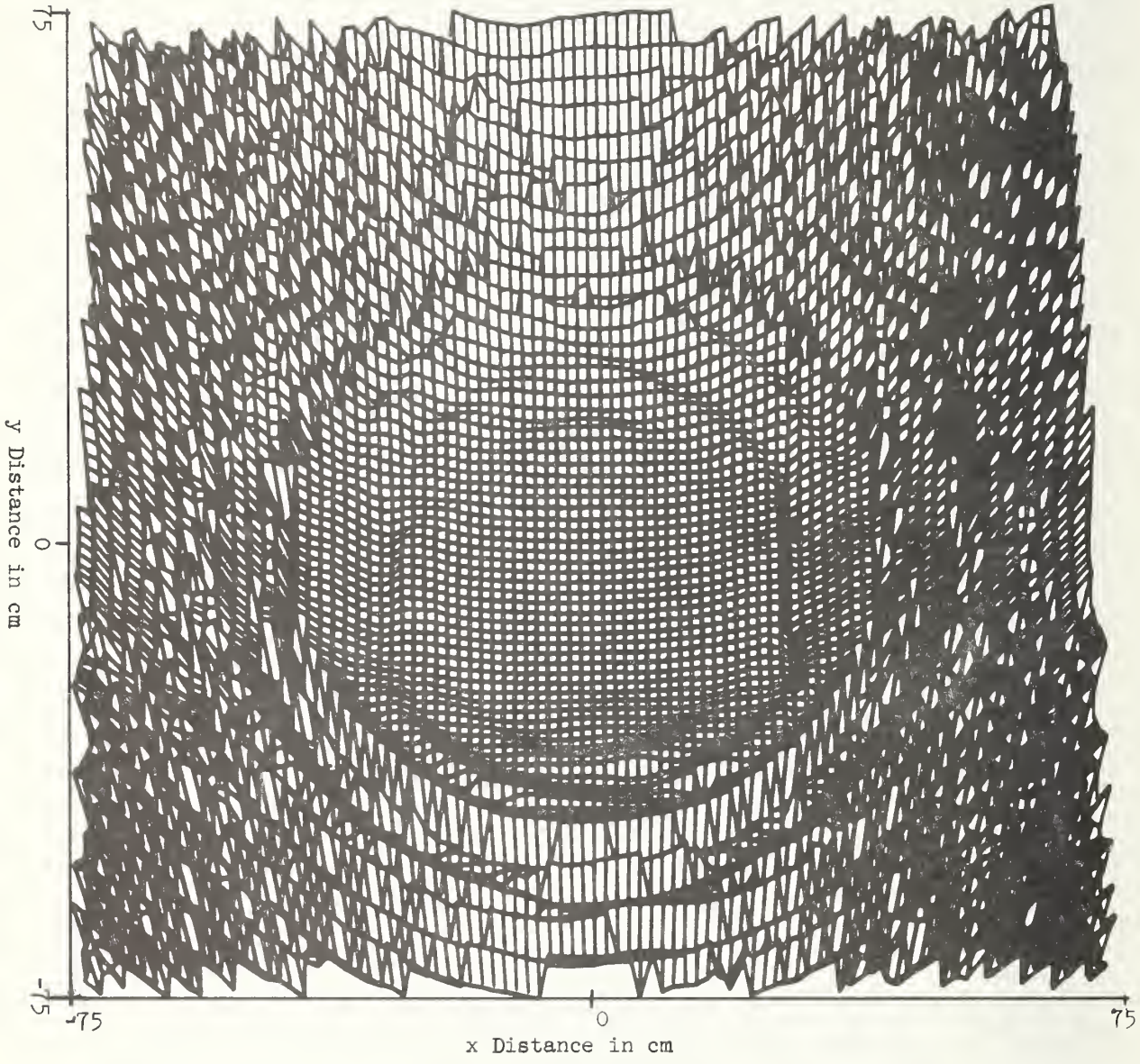

Figure 35b. Near-Field Phase, Constrained Lens Sum Port, f = 9.2 GHz, z = 25 cm.

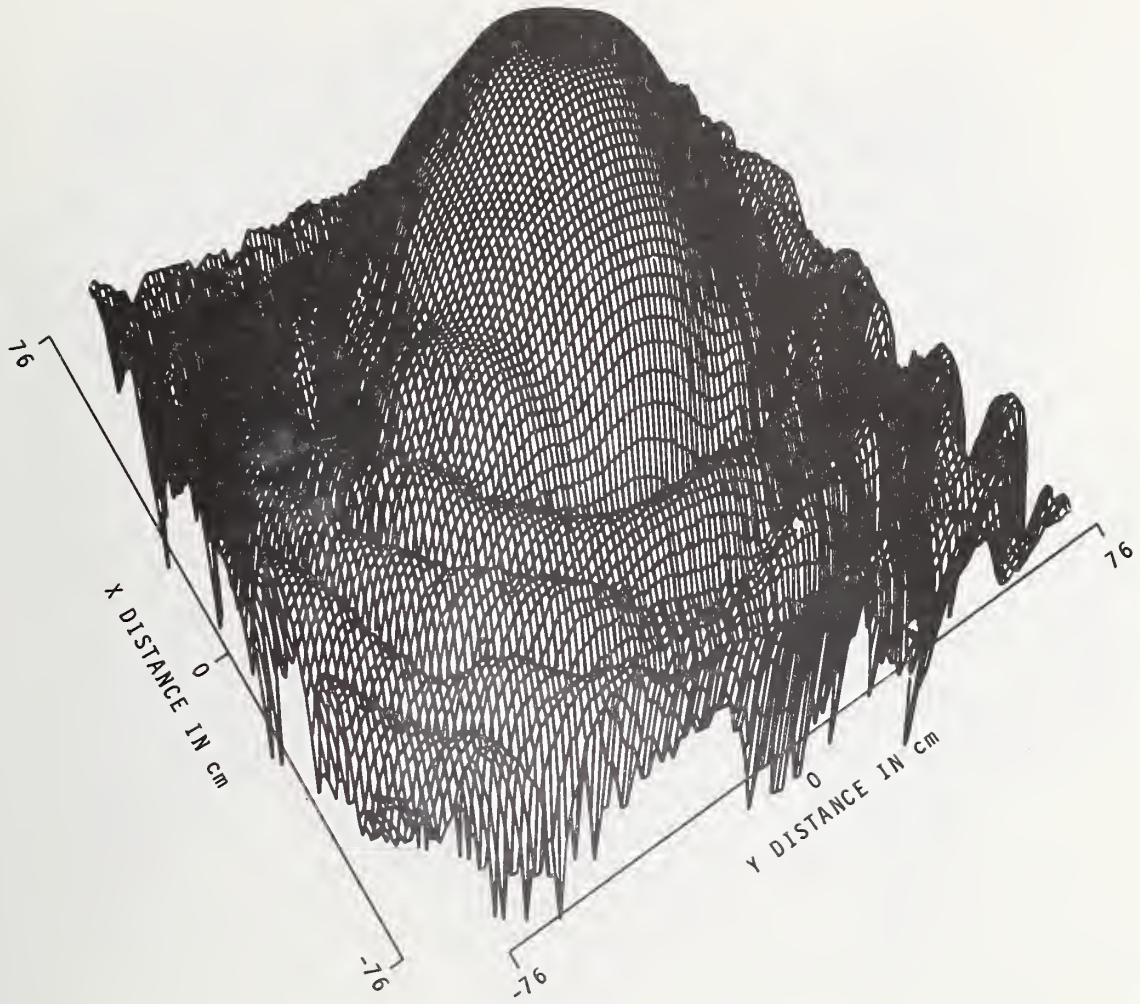

Figure 36a. Constrained Lens Sum Port Near-Field Log Amplitude, f = 9.2 GHz, z = 254 cm, No Radome.

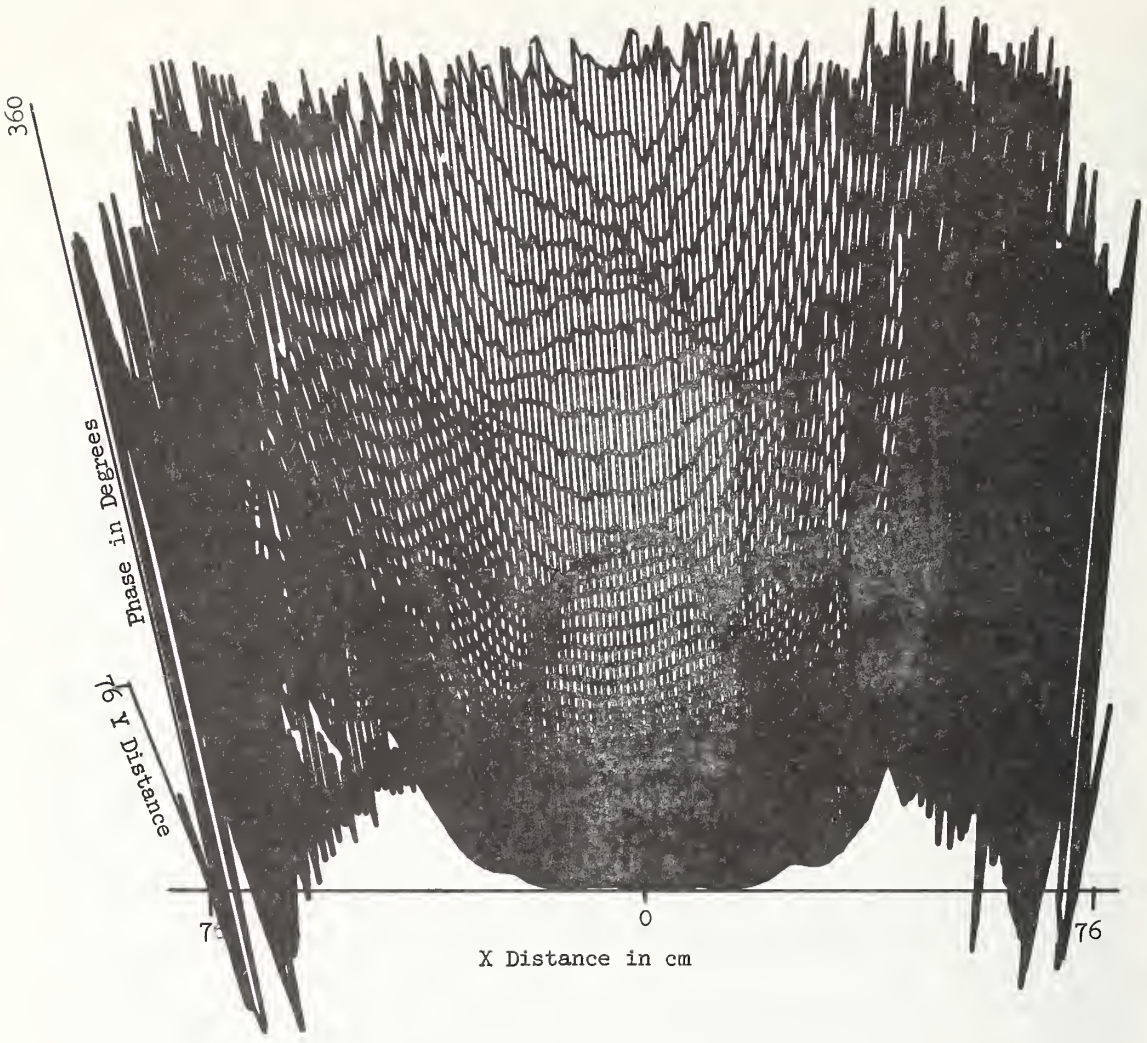

Figure 36b. Near-Field Phase, Constrained Lens Sum Port, f = 9.2 GHz, z = 254 cm.

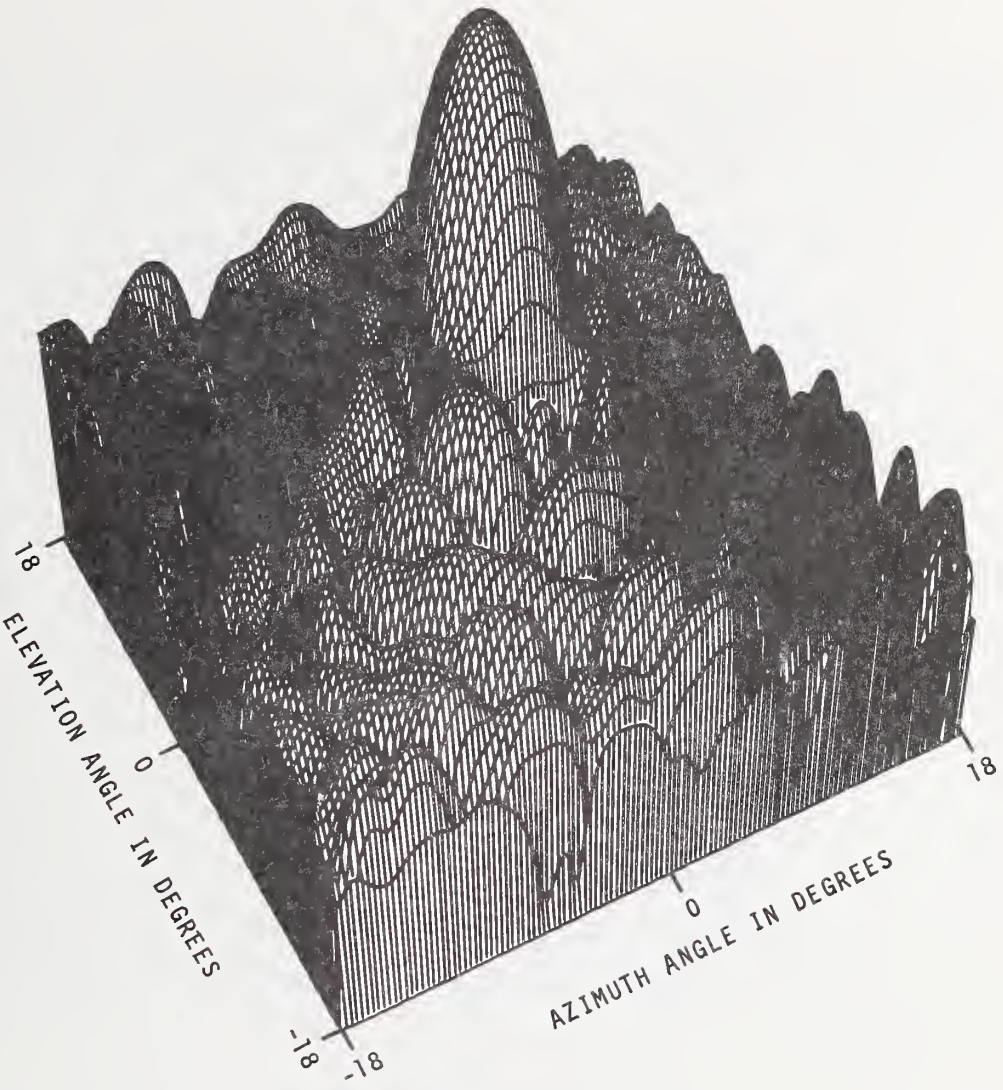

Figure 37. Constrained Lens Sum Port Far-Field Log Amplitude, f = 9.2 GHz, Computed from z = 25 cm Data, No Radome.

$\underline{R}'_{01}(\underline{K})$, and solving the simultaneous equations (18) and (20). The probe correction equations in terms of linear components are

$$S_{10x}(\underline{K}) = D'(\underline{K})R''_{01y}(\underline{K}) - D''(\underline{K})R'_{01y}(\underline{K})/\Delta_{xy} \tag{34a}$$

$$S_{10y}(\underline{K}) = D''(\underline{K})R'_{01x}(\underline{K}) - D'(\underline{K})R''_{01x}(\underline{K})/\Delta_{xy} \tag{34b}$$

where

$$\Delta_{xy} = R'_{01x}(\underline{K})R''_{01y}(\underline{K}) - R''_{01x}(\underline{K})R'_{01y}(\underline{K}). \tag{35}$$

The single primed quantities are the components for the probe in the first orientation and the results from the data measured in that orientation. The double primed quantities are similar quantities after rotating the probe by 90° about its axis, or using a second independent probe, as the case may be. The nature of the probe correction may be seen more clearly by looking at a special case. Let us assume that the probe responds to only one rectangular component of the incident spectrum, and therefore $R'_{01x}(\underline{K}) = R''_{01y}(\underline{K}) = 0$. Equations (34) then reduce to

$$S_{10x}(\underline{K}) = \frac{D''(K)}{R''_{01x}(\underline{K})}, \text{ and} \tag{36a}$$

$$S_{10y}(\underline{K}) = \frac{D'(K)}{R'_{01y}(\underline{K})}. \tag{36b}$$

It is apparent from eq. (36) why the probe may be viewed as a spatial filter, and the probe correction as the adjustment to the computed spectrum for this filtering. Equations (36) also illustrate another important feature of the probe correction, namely that the probe characteristic $\underline{R}_{01}(\underline{K})$ is required only for those directions ($\underline{K}$ values) for which $\underline{S}_{10}(\underline{K})$

is desired. This means that the probe correction is a simple algebraic calculation rather than an integration over an angular region. The probe receiving pattern is therefore required only within the same angular region over which $\underline{S}_{10}(\underline{K})$ is to be determined.

The probe correction equations in terms of spherical components of $\underline{s}(\underline{K})$ and $\underline{r}(\underline{K})$ are very similar, and they illustrate that the various components of $\underline{s}(\underline{K})$ are easily obtainable by using the corresponding components of $\underline{r}'(\underline{K})$ in the probe correction equations. They are

$$s_{10\theta} = D'(\underline{K})r''_{01\phi}(\underline{K}) - D''(\underline{K})r'_{01\phi}(\underline{K})/\Delta_{\theta\phi} \tag{37a}$$

$$s_{10\phi} = D''(\underline{K})r'_{01\theta}(\underline{K}) - D'(\underline{K})r''_{01\theta}(\underline{K})/\Delta_{\theta\phi} \tag{37b}$$

where

$$\Delta_{\theta\phi} = r'_{01\theta}(\underline{K})r''_{01\phi}(\underline{K}) - r''_{01\theta}(\underline{K})r'_{01\phi}(\underline{K}) \tag{38}$$

Similar equations in terms of $\underline{\kappa}_1$ and $\underline{\kappa}_2$ on left and right circular components are easily obtained by using these components in the expansions of eqs. (18), (20) or (22).

The perspective or "three-dimensional" plots such as those in figures 35-37 are very helpful in obtaining an overall view of the measured data and results. Prolems in the data which may not be apparent in the digital printouts are easily detected in this type of presentation. Figure 37 also illustrates the detail and resolution available from the near-field technique. This is one of the distinct advantages of this approach, because the antenna characteristics are obtained over a complete angular region and not just along the principal planes. When it is desirable to look at individual pattern cuts, these are easily obtained from the complete results. Figure 38

shows the patterns in the plane defined by $k_x = 0$ (E-plane for this antenna) for the two sets of data having different separation distances. Over this angular region they are very similar, which illustrates that within the region specified by eq. (27), accurate pattern information can be obtained at fairly large z distances.

Similar near-field data is shown in figures 39a and 39b for the antenna operating in the elevation difference mode, with complete and principal plane patterns in figures 40 and 41 respectively. The two patterns in figure 41 are again for data taken at z = 25 and z = 254 cm.

The data and results in all the previous figures have been for the usual case where the test antenna was transmitting and the probe receiving. For some tests, the mode of operation was changed, and the probe was used in the transmitting mode. The test antenna remained in the elevation difference mode since this more complex pattern should provide a more difficult test. Since both antennas in this case are reciprocal, the results of the test should be identical with those obtained with the probe receiving. The patterns are essentially identical as can be seen from figure 42. This confirms that measurements can be made with either a transmitting or receiving probe. This is required if the antenna is not reciprocal, and was in fact the case for the Volphase antenna.

Measurements with the Volphase antenna were not as fully automated using the small scanner system as were those with the constrained lens using the large scanner system. The small scanner consisted of a modified lathe bed driven by a constant-speed synchronous motor combined with a digital clock and optical position indicator and trigger mechanism. The scanner had to be manually reset in y after each scan for the desired step interval. The scan direction for this case was x. The measurement process is somewhat slower than the fully automated

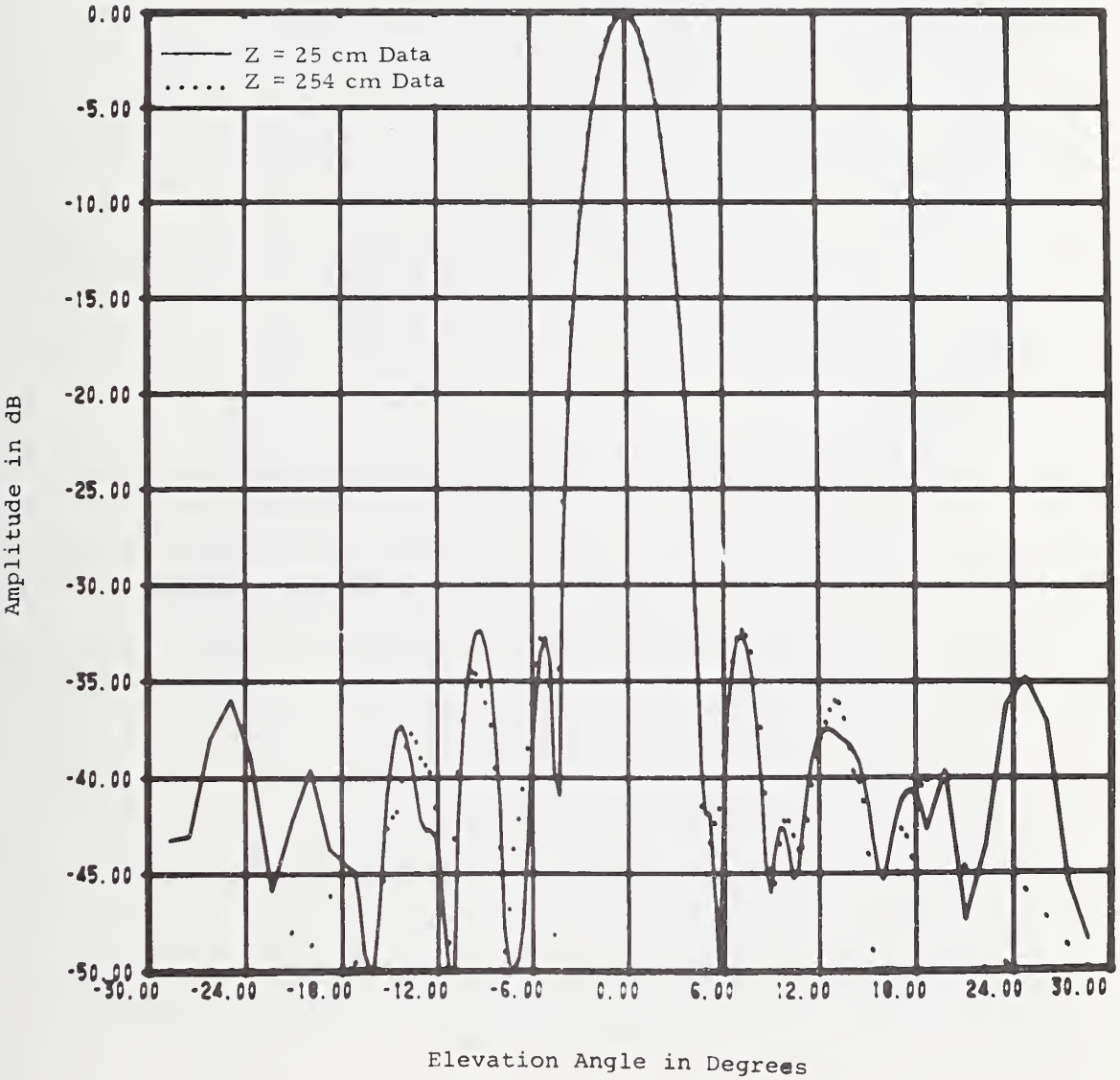

Figure 38. Comparison Between Far-Field Patterns Computed from Near-Field Data taken at Two Different z-Distances. Constrained Lens Antenna, E-Plane Sum Pattern.

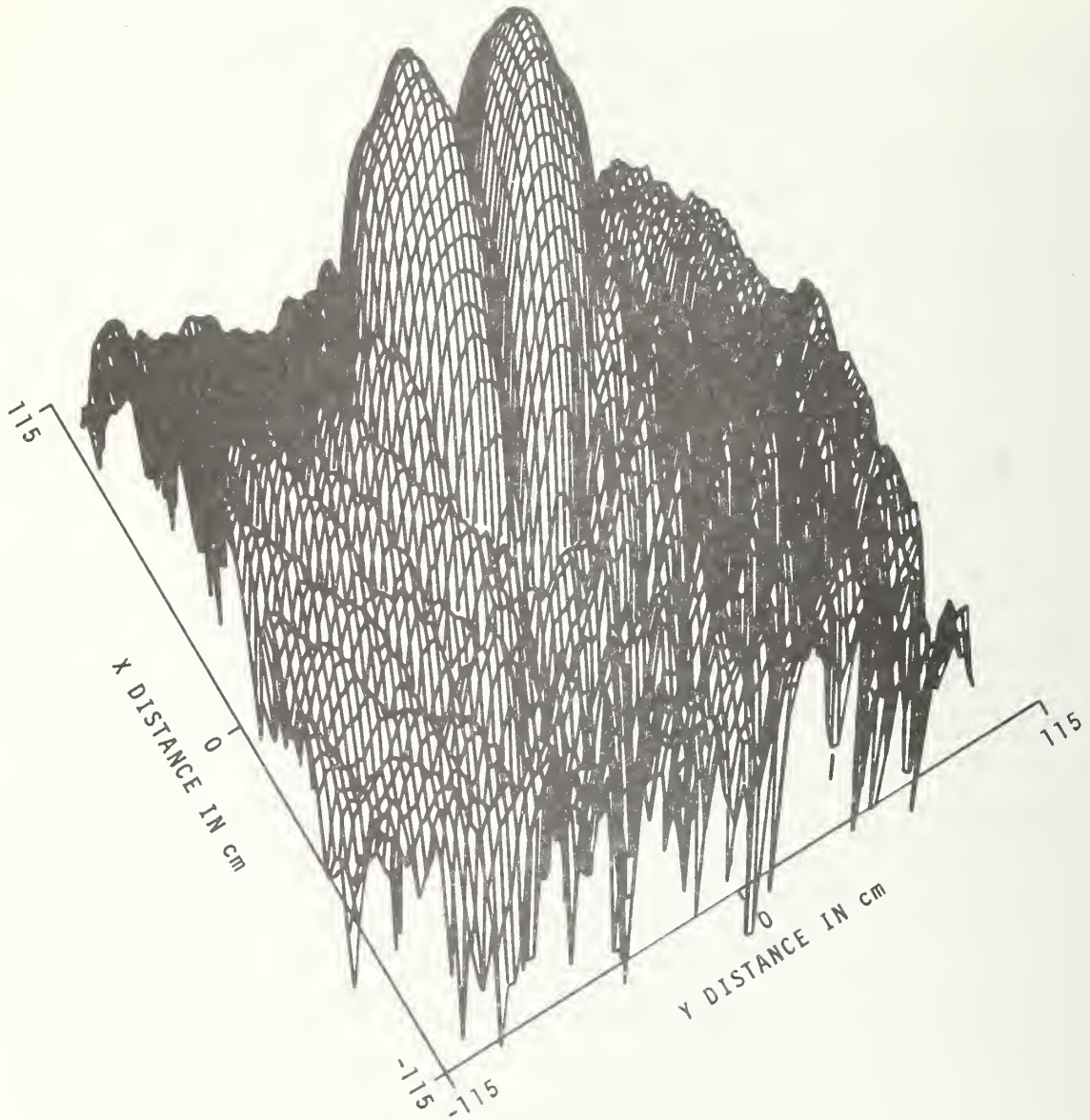

Figure 39a. Constrained Lens Elevation Difference Port Near-Field Log Amplitude, f = 9.2 GHz, z = 250 cm, No Radome.

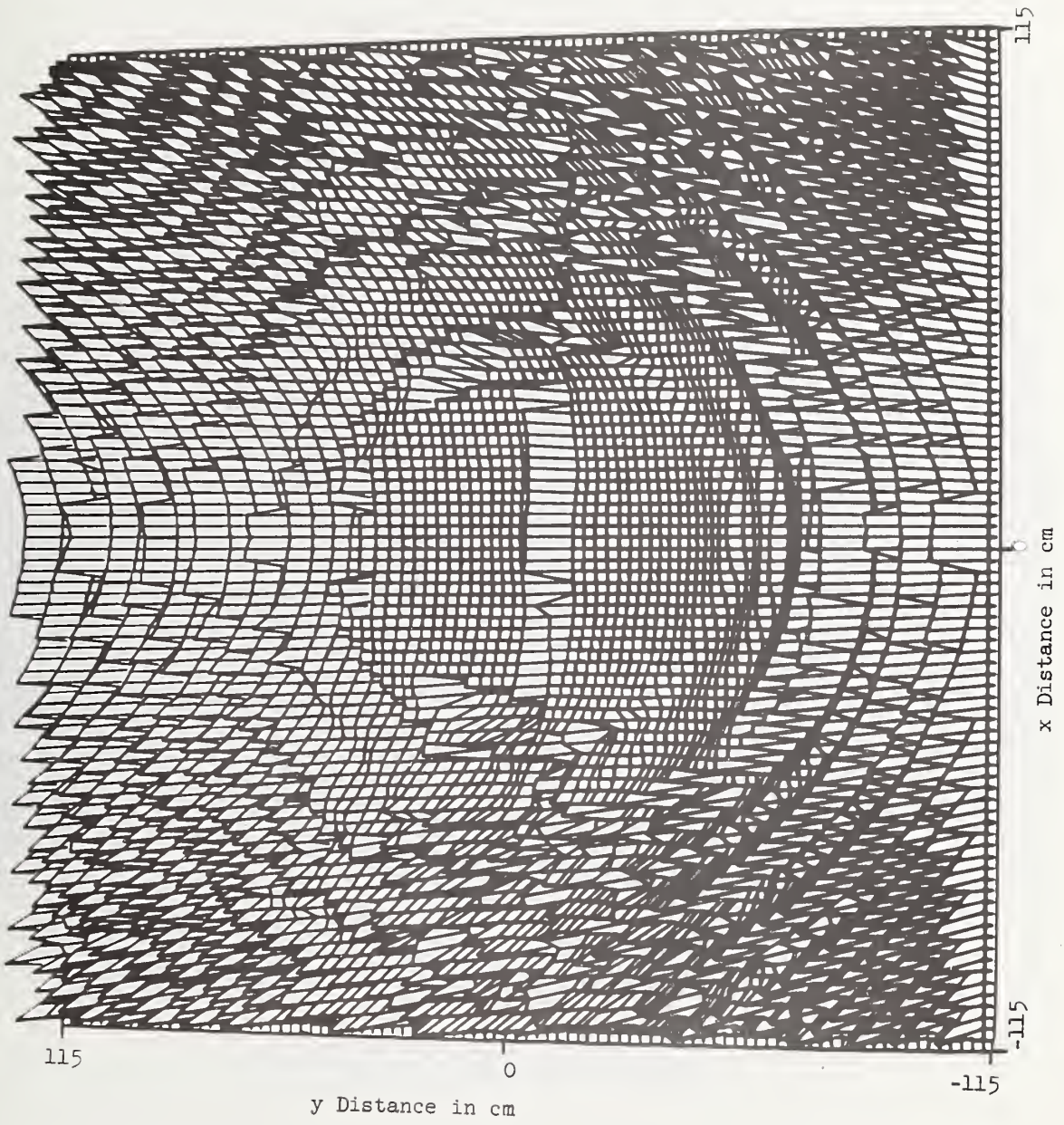

Figure 39b. Near-Field Phase, Constrained Lens Elevation Difference Port, f = 9.2 GHz, z = 250 cm.

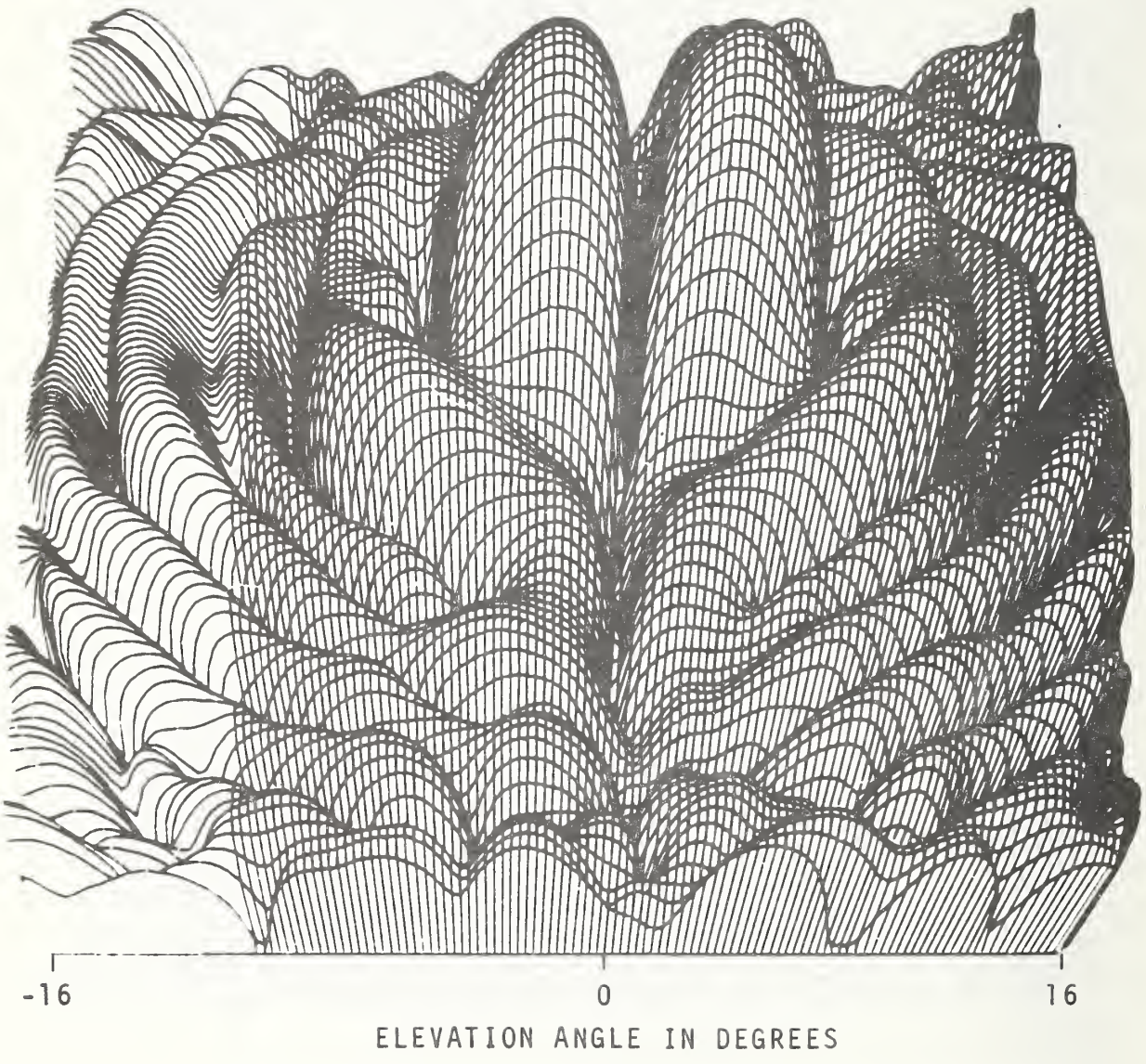

Figure 40. Constrained Lens Elevation Difference Port Log Amplitude, f = 9.2 GHz, Computed from z = 25 cm Data, No Radome.

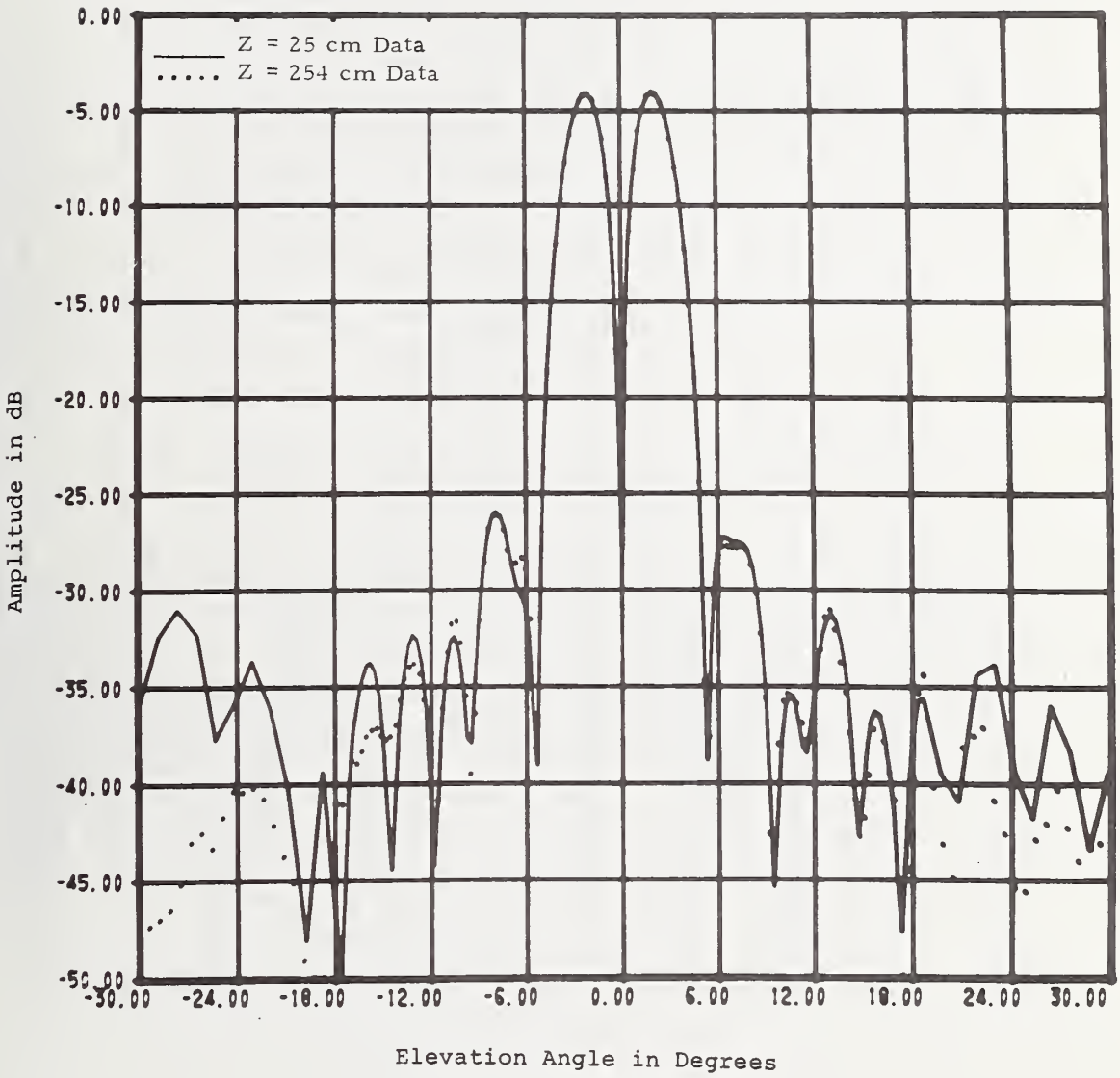

Figure 41. Comparison Between Far-Field Patterns Computed from Near-Field Data taken at Two Different z-Distances. Constrained Lens, E-Plane Elevation Difference Pattern.

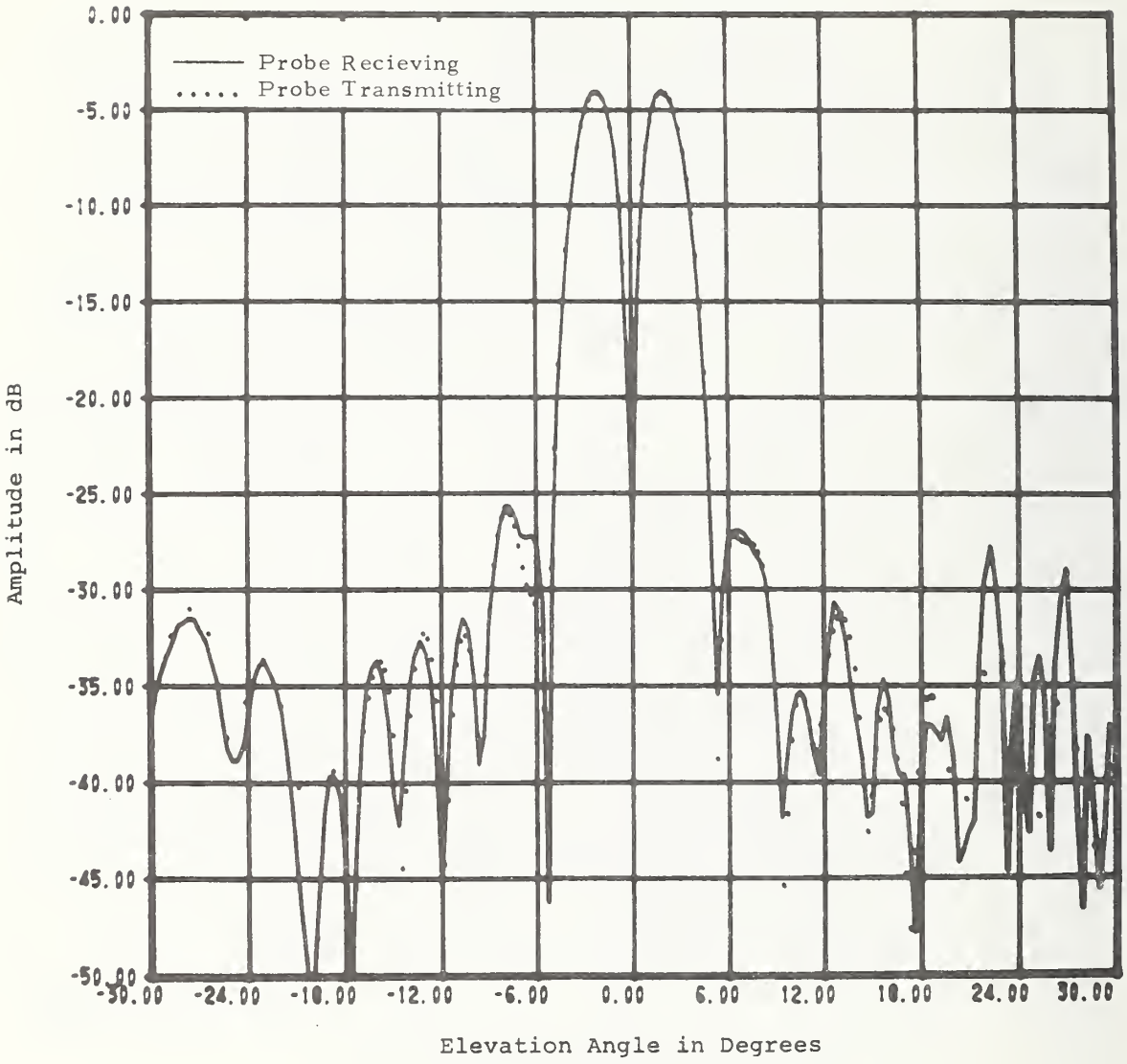

Figure 42. Comparison Between Far-Field Patterns Computed from Near-Field Data with Probe Transmitting and Receiving. Constrained Lens Antenna, E-Plane Elevation Difference Pattern.

system used with the constrained lens but did allow limited sized, two dimensional scans that took approximately four hours to complete. Because movement in the y direction was manual only, it was not practical to take normalization scans as was done with the large scanner with the constrained lens antenna. Therefore, the measurements with the Volphase antenna system were checked periodically and corrected for drift. The technique otherwise is the same for the two systems and utilizes the same equations for computing the far field patterns. A number of two-dimensional scans were made with the Volphase antenna (table 4). The same data processing was carried out on this data, and the results for some measurement cases will be described in the following section.

3.3.2 Pattern Comparisons for the Constrained Lens and Volphase Antenna

Pattern measurements were made on the antennas on conventional far-field ranges both before and after the near-field measurements. These patterns were compared with those computed from near-field data to demonstrate the agreement between these two methods. The results of some of these comparisons are shown in figures 43-48. The comparisons for the constrained lens are certainly within the limits of accuracy of the far-field measurements where ground reflections cause significant errors when the pattern is below about 30 dB.

On the Volphase comparisons, there is a definite degradation in accuracy in the near-field results for positive angles when the beam was steered to +30° off boresight. This is due to the limited scan area available with the small portable scanner. With the beam steered to +30°, the amplitude at the +x edge of the scan area was only 15-20 dB below the near-field

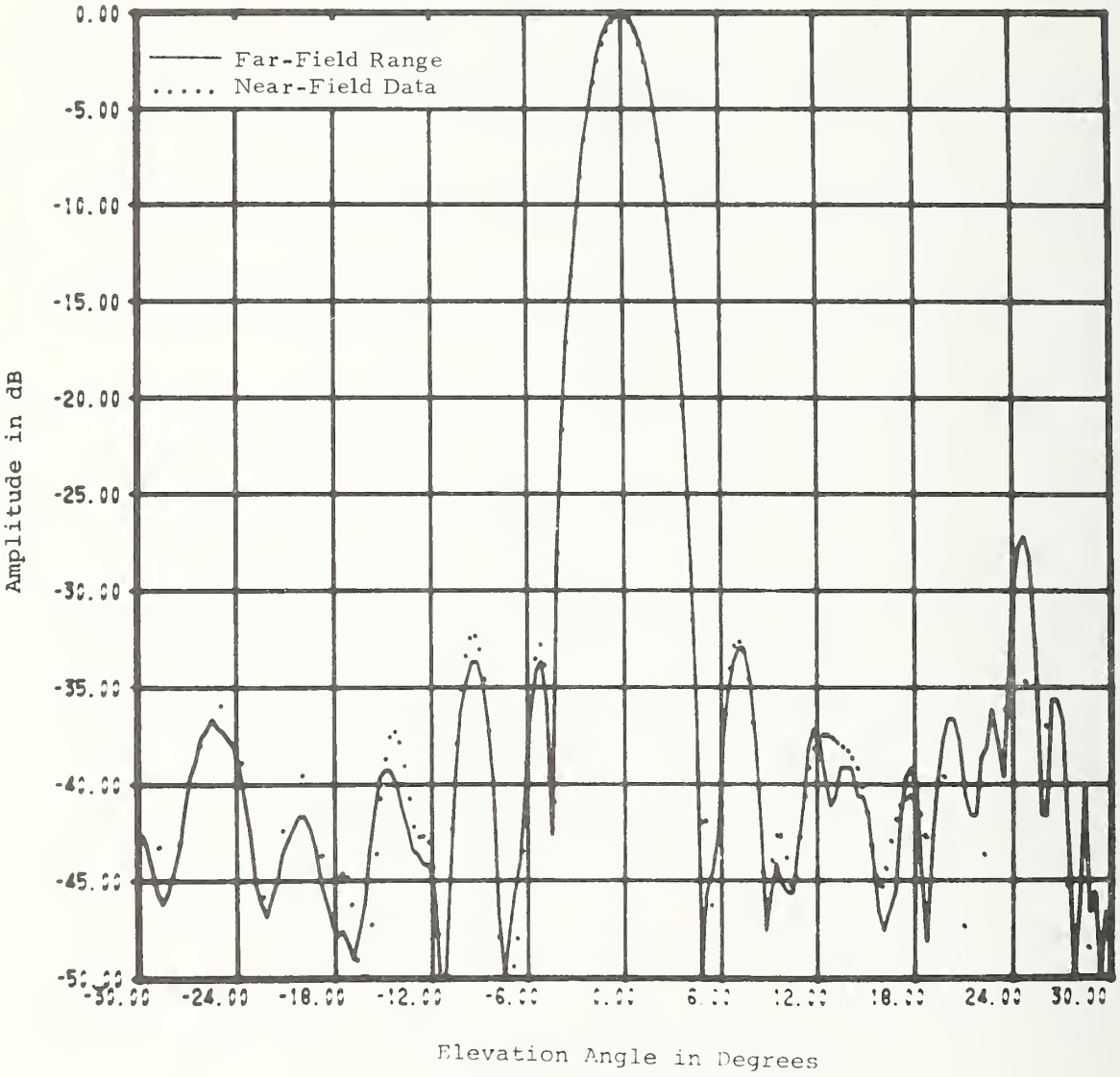

Figure 43. Comparison Between Far-Field Patterns Measured on Far-Field Range and Computed from Near-Field Data. Constrained Lens, E-Plane Sum Pattern.

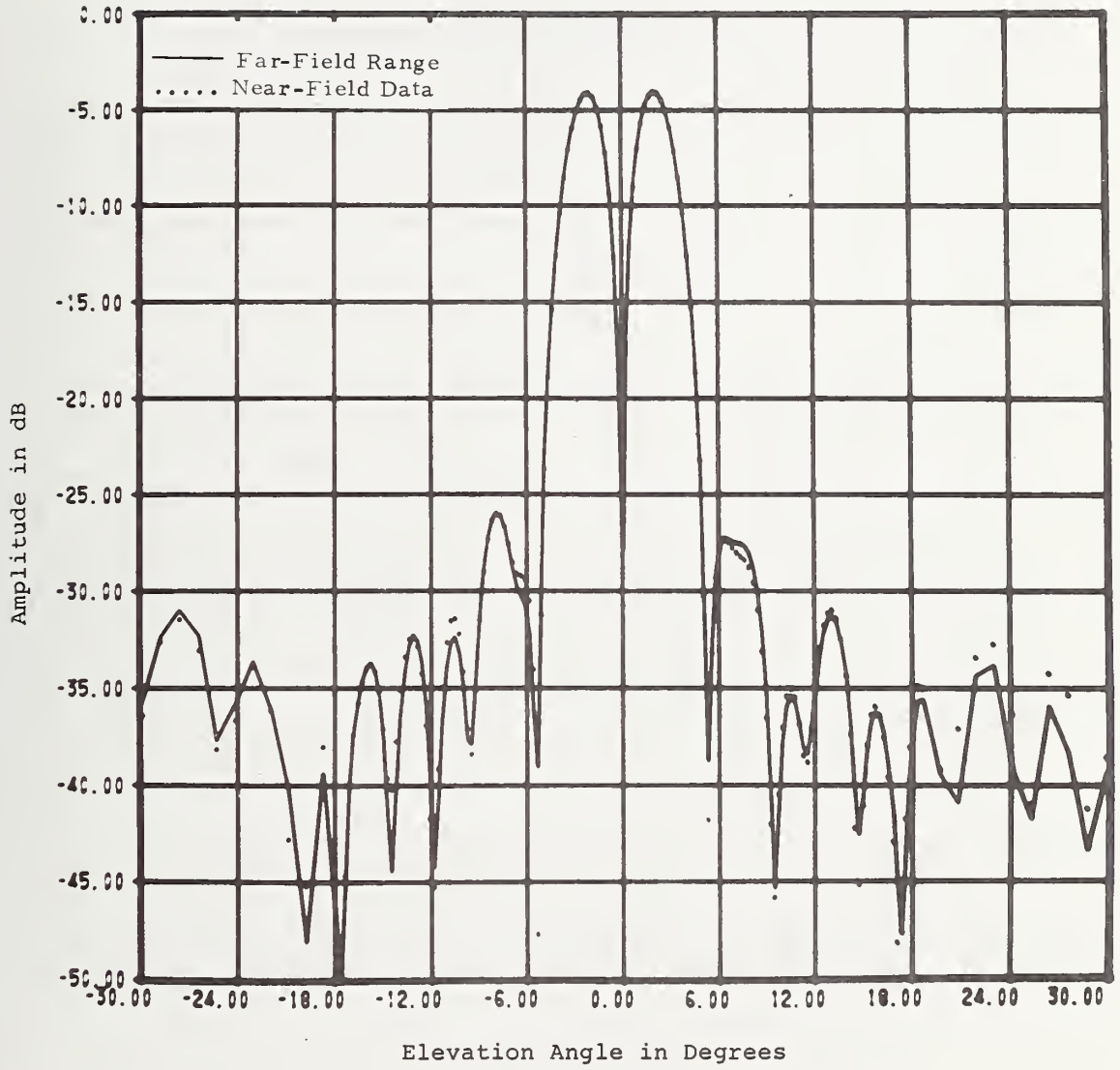

Figure 44. Comparison Between Far-Field Patterns Measured on Far-Field Range and Computed from Near-Field Data. Constrained Lens, E-Plane Elevation Difference.

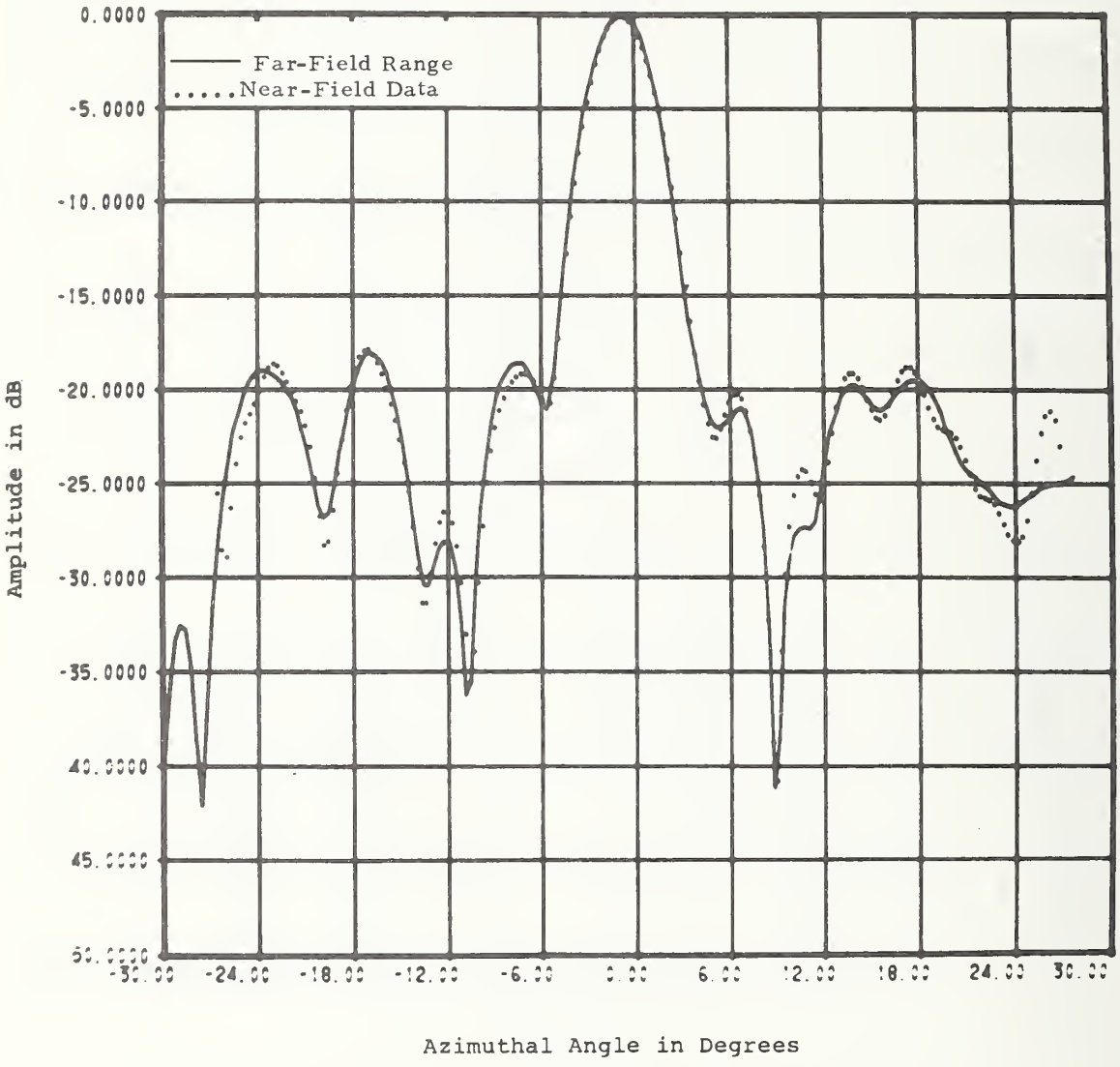

Figure 45. Comparison Between Far-Field Patterns Measured on Far-Field Range and Computed from Near-Field Data. Volphase Antenna, 0° Sum Pattern.

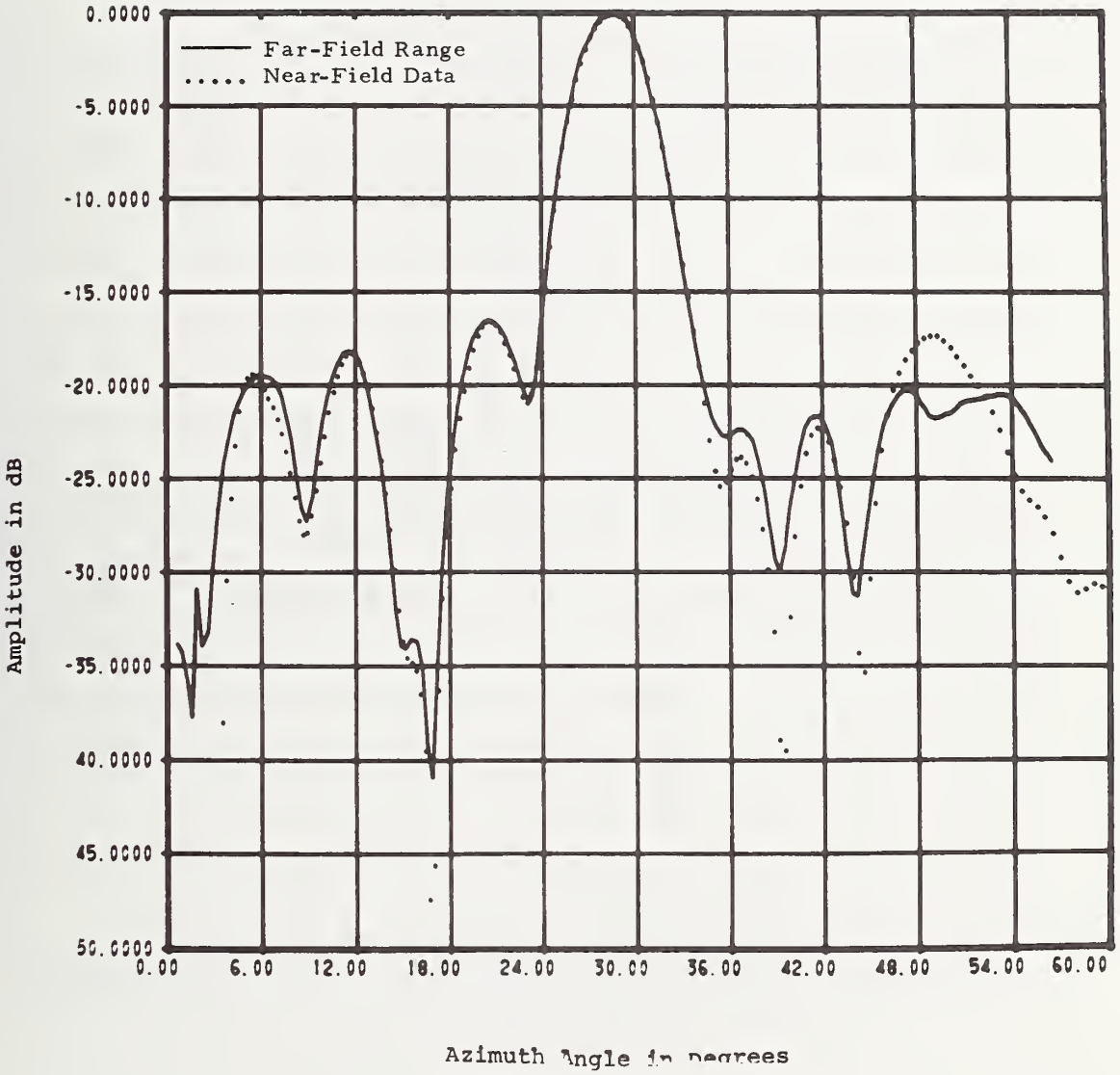

Figure 46. Comparison Between Far-Field Patterns Measured on Far-Field Range and Computed from Near-Field Data. Volphase, 30° Sum Pattern.

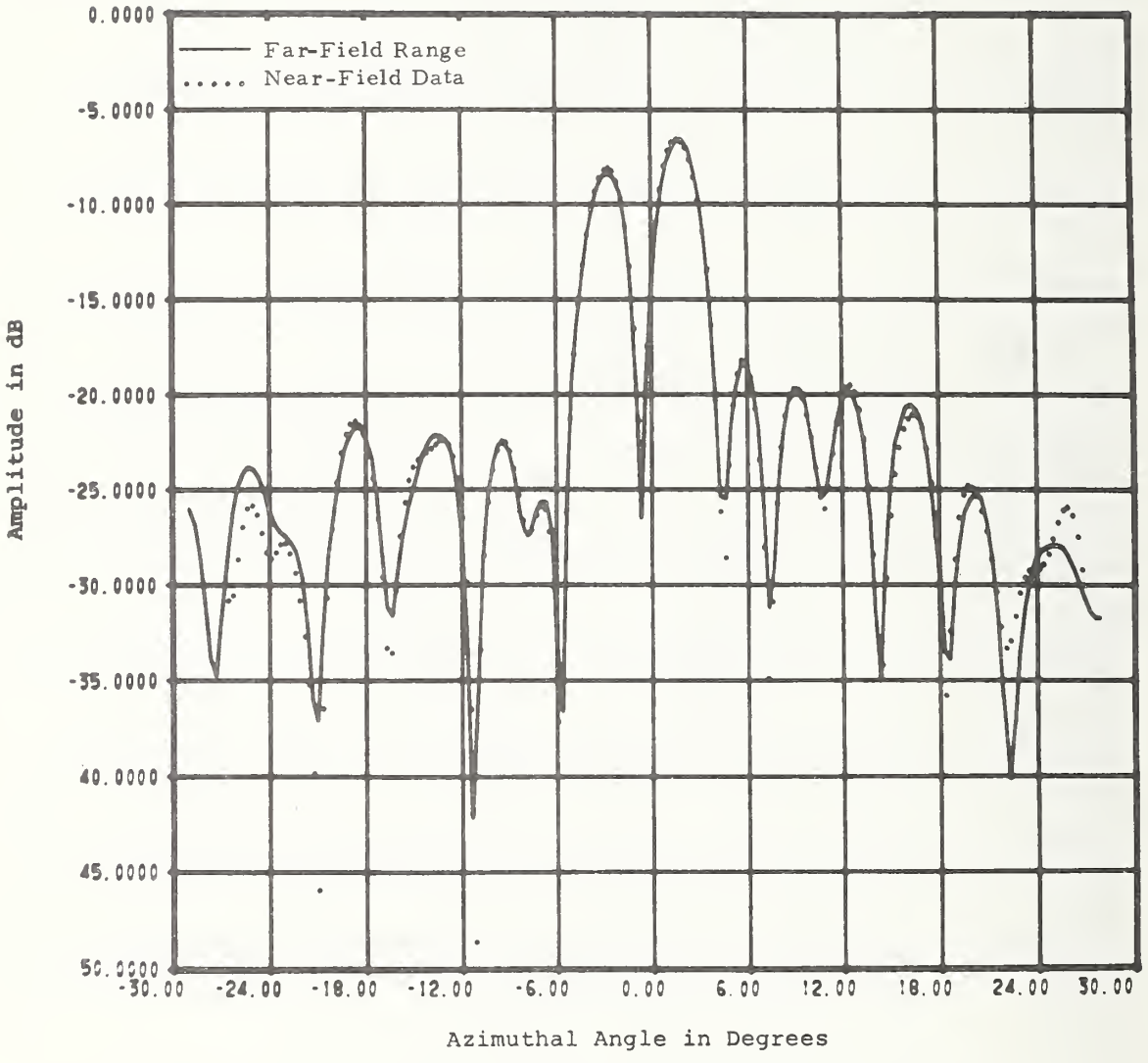

Figure 47. Comparison Between Far-Field Patterns Measured on Far-Field Range and Computed from Near-Field Data. Volphase Antenna, 0° Azimuth Difference Pattern.

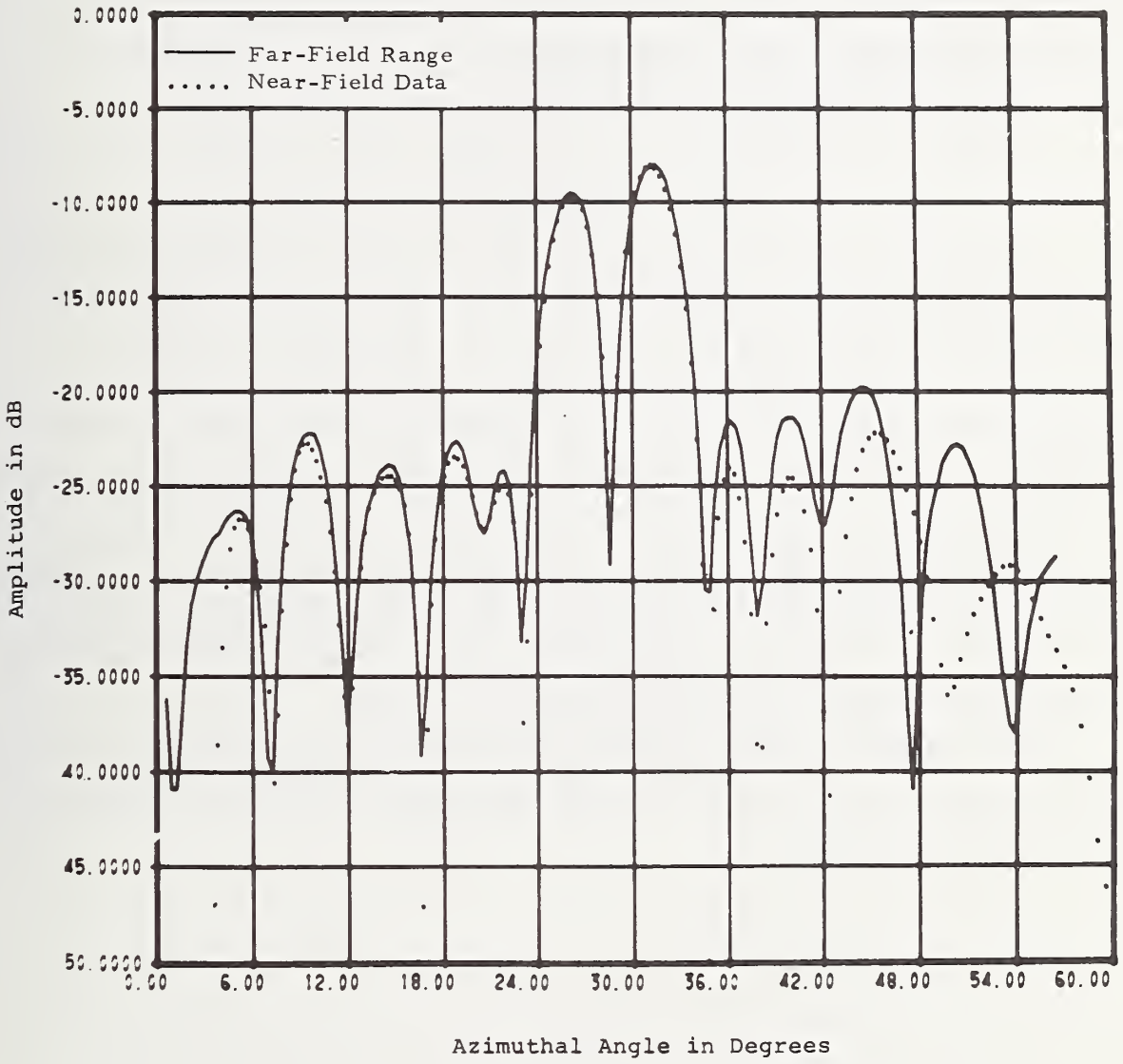

Figure 48. Comparison Between Far-Field Pattern Measured on Far-Field Range and Computed from Near-Field Data. Volphase Antenna, 30° Azimuth Difference Pattern.

maximum and the truncation of significant data caused the larger errors on this side of the pattern. Considering the small scan area, the small amount of absorbing material used, and the very unconventional "range," these comparisons are quite remarkable. They illustrate quite graphically that the planar near-field technique can be used very successfully in many antenna measurement situations.

4.0 Conclusions

The planar near-field measurement technique can be applied very successfully to high performance phased array antennas. In some cases, the amount of required data can be reduced by using data-point spacings of greater than $\lambda/2$, reducing the measurement area, or both. Even when the beam is steered to 45 degrees off axis, the required spacing is still only slightly less than $\lambda/2$.

Fast and efficient tests using centerline data can be performed to determine the required scan area, data point spacings, the effect of multiple reflections, and possibly the location of faults in the test antenna and/or radome.

The pattern comparisons indicate that the results computed from near-field data are in good agreement with those measured on far-field ranges.

References

[1] D.M. Kerns and E.S. Dayhoff, "Theory of diffraction in microwave interferometry," J. Res. Nat. Bur. Stand., Vol. 64B, pp. 1-13, Jan.-Mar. 1960.

[2] D.M. Kerns, "Correction of near-field antenna measurements made with an arbitrary but known measuring antenna," Electron. Lett., Vol. 6, pp. 346-347, May 1970.

[3] D.M. Kerns, "New method of gain measurement using two identical antennas," Electron. Lett., Vol. 6, pp. 347, 349, May 1970.

[4] R.C. Baird, A.C. Newell, P.F. Wacker, and D.M. Kerns, "Recent experimental results in near-field antenna measurements," Electron. Lett., Vol. 6, pp. 349-351, May 1970.

[5] E.B. Joy and D.T. Paris, "Spatial sampling and filtering in near-field measurements," IEEE Trans. Antennas Propagat., Vol. AP-20, pp. 253-261, May 1972.

[6] D.M. Kerns and R.W. Beatty, Basic Theory of Waveguide Junctions and Introductory Microwave Network Analysis (Pergamon Press, Oxford, 1967).

[7] D.M. Kerns, "Plane-wave scattering matrix and generalized reciprocity relations for antennas and scatters," NBS Report (unpublished), June 1972.

NBS-114A (REV. 7-73)

U.S. DEPT. OF COMM. BIBLIOGRAPHIC DATA SHEET	1. PUBLICATION OR REPORT NO. NBSIR 74-380	2. Gov't Accession No.	3. Recipient's Accession No.

4. TITLE AND SUBTITLE

Planar Near-Field Measurements on High Performance Array Antennas

5. Publication Date

6. Performing Organization Code

7. AUTHOR(S)
Allen C. Newell & Myron L. Crawford

8. Performing Organ. Report No.
NBSIR 74-380

9. PERFORMING ORGANIZATION NAME AND ADDRESS

NATIONAL BUREAU OF STANDARDS
DEPARTMENT OF COMMERCE
Boulder, Colorado 80302

10. Project/Task/Work Unit No.
2727454

11. Contract/Grant No.
F33615-73-M-6001

12. Sponsoring Organization Name and Complete Address *(Street, City, State, ZIP)*

Air Force Avionics Laboratory
Wright-Patterson Air Force Base
Ohio 45433

13. Type of Report & Period Covered
Final Report FY 73

14. Sponsoring Agency Code

15. SUPPLEMENTARY NOTES

U.S. Air Force Technical Report

16. ABSTRACT *(A 200-word or less factual summary of most significant information. If document includes a significant bibliography or literature survey, mention it here.)*

The results of measurements which apply the planar near-field measurement technique to phased array antennas are described. Fast and efficient tests are used to determine the required scan area and data point spacing. The use of these tests can reduce the amount of data required for some antennas without significantly increasing the errors in computed results.

Measurements were made at different distances from the antennas, with the probe transmitting and receiving, and for both sum and monopulse difference patterns. Comparisons between the far-field patterns computed from the near-field data and those measured on far-field ranges are presented.

17. KEY WORDS *(six to twelve entries; alphabetical order; capitalize only the first letter of the first key word unless a proper name; separated by semicolons)*

Antennas; near-field measurements; phased arrays.

18. AVAILABILITY

[x] Unlimited

[ ] For Official Distribution. Do Not Release to NTIS

[ ] Order From Sup. of Doc., U.S. Government Printing Office Washington, D.C. 20402, SD Cat. No. C13

[ ] Order From National Technical Information Service (NTIS) Springfield, Virginia 22151

19. SECURITY CLASS (THIS REPORT)
UNCLASSIFIED

21. NO. OF PAGES

20. SECURITY CLASS (THIS PAGE)
UNCLASSIFIED

22. Price

USCOMM - ERL USCOMM-DC 29042-P74